



TÉCNICO
LISBOA



Design, Control, and Testing of a Trimodal Unmanned Aerial Vehicle

Afonso Diniz Correia e Vale

Thesis to obtain the Master of Science Degree in

Aerospace Engineering

Supervisors: Dr. Meysam Basiri
Prof. Frederico José Prata Rente Reis Afonso

Examination Committee

Chairperson: Prof. Pedro Tiago Martins Batista
Supervisor: Dr. Meysam Basiri
Member of the Committee: Prof. André Calado Marta
Member of the Committee: Prof. Alexandra Bento Moutinho

July 2024



"That'll buff out" - Jeremy Clarkson

Declaration

I declare that this document is an original work of my own authorship and that it fulfills all the requirements of the Code of Conduct and Good Practices of the Universidade de Lisboa.

Acknowledgments

Aerospace Engineering is a multidisciplinary subject, and this work is no exception. As such, I would like to thank all who contributed to this work, with your opinion or with your help, namely:

To my supervisors, Prof. Frederico Afonso and Dr. Meysam Basiri, for your help and patience in guiding this work, and for always receiving me in your offices with questions or news.

To Tenente Vasco Coelho and to the Academia da Força Aérea, for your patience throughout the 7 different visits for wind tunnel tests, and for your help with these tests.

To Comandante Mourinha, Capitão-tenente Veloso, Segundo Tenente Gonçalves and CEOM, for allowing me to do tests in the CEOM facilities, for providing all the help possible in these tests and for employing a drone to record video footage, and to the CEOV, for facilitating these tests.

To Gaspar, for your "bitaites" about the structure of the wheels, and for printing the LW-PLA canopy.

To Francisco, for experiently flying the UAV, and providing key insights into its behaviour.

To Prof. Marco Leite and his students, for printing crucial parts, and for teaching me about 3D printing.

To AEIST, for allowing me to do tests on the football field.

To DSOR, for lending me a power module.

To Prof. Rodrigo Ventura and his students, for lending me the thrust stand used for propulsion tests.

To AeroTéc, and in particular the ATLAS project, for providing carbon fibre tubes and epoxy resin, for allowing me to use the lab and the hot wire CNC machine, and for lending me batteries for the operational tests. To all the ATLAS members who helped me use the hot wire CNC, for your time.

To Diogo, for the journey that was this thesis, and also to everyone else who like you, helped in any way in any of the tests, either by helping carry things, blocking the road, filming the tests, or providing moral support when the "gingarelho" would simply not move forward.

The journey to this point started much before this thesis did, and so I extend my greatest gratitude:

To everyone with whom I crossed paths in UAV(-ART) and ATLAS, including, Diogo, Afonso, Simão, Luís, Pinto, Francisco, Vitor, Ricardo, André, Peixoto, and everyone whom I had the chance to work with in OAT, and in the Systems team. Together, we achieved the unimaginable, and thanks to you I learned almost all that I know about UAVs, living some of the coolest, most stressful but still awesome moments in the process. Thank you for all the great memories and milestones.

To my dear colleagues in the Direção 21/22 and Direção 22/23, Thomas, Madeira, Valqueresma, Eva, Filipe, Vitor, Maria, Dores, João, Tiago, Gaspar, Machado, Tânia, Maria and Diogo, for sticking together throughout the toughest moments, and for the great friendships that ensued.

To everyone from Web.Dev, Pratas, Rafaela, João, Medeiro and André, for taking on a new challenge and for obviously all the in-person meetings.

To Eva, for the great company, advice and conversations. To João, for enduring a challenging year, and for all the 2 o'clock Teams meetings. To Mariana, for all the support and almoços. To Pratas and Rafaela, for all the cafés de Qanela.

To my parents and sister, for always trusting, supporting me, and cheering me on.

And last but not least, to all the great friends I made throughout the past 5 years.

Resumo

Os veículos não tripulados têm potencial de aumentar a eficiência, segurança e eficácia de tarefas tipicamente realizadas por humanos. A maioria das soluções disponíveis aplica veículos não tripulados dedicados a operações em ambiente aéreo, terrestre, ou submarino, no entanto, veículos híbridos, capazes de operar em diferentes modos, tornam o envelope de operações mais abrangente, e podem aumentar a eficiência energética. Nesta tese propõe-se um novo veículo aéreo não tripulado trimodal, capaz de rolar no chão, voo pairado e horizontal. O design é composto por uma estrutura de quadricóptero com componentes modulares, duas rodas passivas montadas num eixo para movimento no solo, e duas asas montadas na estrutura para voo de asa fixa. Para a implementação de controlo automático no solo, o firmware ArduPilot foi modificado com novos modos de controlo adicionados e da capacidade de executar missões automáticas com waypoints no chão e combinando os três modos de operação. O protótipo construído foi testado, tendo sido capaz de operar nos três modos, de onde foram retirados resultados de eficiência energética. Em voo horizontal, o alcance da aeronave aumentou, a custo de autonomia reduzida, enquanto que em operação no solo tanto o alcance como a autonomia aumentaram significativamente, comparando com o quadricóptero base. Em voo pairado, a adição de asas aumentou a autonomia, ainda que com alcance diminuto. Com as asas posicionadas com incidência, verificou-se um aumento superior de autonomia, e até mesmo de alcance, a custo de perda de estabilidade. Mostrou-se ainda a capacidade de subir inclinações, como paredes.

Palavras-chave: Locomoção Híbrida, Veículo Aéreo Não Tripulado, ArduPilot, Eficiência Energética, Controlo Automático, Design Modular

Abstract

Unmanned vehicles have shown potential in increasing the efficiency, safety and efficacy of tasks previously performed by humans. Most currently available solutions employ unmanned vehicles targeted at either aerial, ground or underwater environments, but multimodal vehicles, capable of operating in multiple modes, can make the operating envelope broader and increase energy efficiency. This work proposes a novel trimodal unmanned aerial vehicle, capable of ground locomotion, and aerial operations with hover and forward flight capacity. The design is based on a quadcopter base frame with modular components, two passive wheels attached to an axle for ground movements, and two wings attached to the quadcopter frame for forward flight. To implement automatic control on the ground, the ArduPilot firmware was modified with new control modes and the ability to execute automatic waypoint missions on the ground and combining multiple operating modes. The assembled prototype was tested and capable of operating in all three modes, from where energy efficiency results were drawn. In forward flight, the vehicle range increased, but at the cost of lower endurance, while in ground mode, both endurance and range increased significantly compared to the base quadcopter used. In hovering flight, the usage of wings was shown to increase the endurance of the vehicle, at the cost of reduced range. With the wings positioned at an angle, a further increase in endurance and now range was observed, at the cost of less controllability. The vehicle was also shown to be capable of climbing inclined surfaces, such as walls.

Keywords: Multimodal Locomotion, Unmanned Aerial Vehicle, ArduPilot, Energy Efficiency, Automatic Control, Modular Design

Contents

- Acknowledgments vii
- Resumo ix
- Abstract xi
- List of Tables xvii
- List of Figures xix
- Nomenclature xxiii
- Acronyms xxviii

- 1 Introduction 1**
- 1.1 Motivation 1
- 1.2 Topic overview 2
- 1.3 Objectives 2
- 1.4 Thesis outline 3

- 2 State of the Art 4**
- 2.1 Inspection tasks using aerial robots 4
- 2.2 Multimodal aerial-terrestrial UAVs 4
 - 2.2.1 Actively actuated designs 5
 - 2.2.2 Passively actuated designs 7
- 2.3 Air based multimodal UAVs 9
 - 2.3.1 Lift + Cruise VTOL 9
 - 2.3.2 Tiltrotor VTOL 10
 - 2.3.3 Tiltwing VTOL 11
 - 2.3.4 Tailsitter VTOL 11
- 2.4 Review Summary 12

- 3 System design 13**
- 3.1 Structural design 13
 - 3.1.1 Frame 13
 - 3.1.2 Wheels 14
 - 3.1.3 Wings 15
 - 3.1.4 Assembly 16

3.2	Aerodynamic design	17
3.2.1	Operating conditions	18
3.2.2	2D aerofoil design	19
3.2.3	3D wing design	20
3.3	Propulsive system	23
3.3.1	Battery	23
3.3.2	Electronic Speed Controller	25
3.3.3	Electric motor	25
3.3.4	Propeller	27
3.3.5	Performance simulation	31
3.4	Avionic systems	34
3.4.1	System components	34
3.4.2	Autopilot firmware	35
4	Controller implementation	37
4.1	Vehicle dynamics	37
4.1.1	Hover dynamics	38
4.1.2	Forward flight dynamics	40
4.1.3	Ground dynamics	42
4.2	Control laws	43
4.2.1	Motor mixer	44
4.2.2	Attitude rate controller	45
4.2.3	Attitude controller	46
4.2.4	Position controller	49
4.2.5	Waypoint controller	52
4.3	Control modes	53
4.3.1	Hover modes	53
4.3.2	Forward-flight modes	54
4.3.3	Ground modes	55
4.4	Transition controller	56
4.4.1	Hover \longleftrightarrow Fixed-wing transition	56
4.4.2	Hover \longleftrightarrow Ground transition	56
5	Experiments & Results	57
5.1	Propulsive system	57
5.1.1	Test bench	57
5.1.2	Propulsive performance	58
5.2	Wind tunnel	61
5.2.1	Wind tunnel setup	61
5.2.2	Aerodynamic performance	62

5.3	Operational tests	67
5.3.1	Hovering flight	68
5.3.2	Forward flight & transition	70
5.3.3	Ground locomotion	72
5.3.4	Energy efficiency	74
5.3.5	Multimodality	77
6	Conclusions	79
6.1	Achievements	79
6.2	Future work	80
	Bibliography	81
A	ArduPilot 4.5.0 controllers	89
B	ArduPilot controllers	90
B.1	Forward flight	90
B.1.1	Position control	90
B.2	Mission commands	95
C	ArduPilot control modes	98
C.1	Hover modes	98
C.1.1	QSTABILIZE	98
C.1.2	AUTO and QRTL	98
C.2	Forward flight modes	99
C.2.1	FBWB	99
C.2.2	AUTO, GUIDED and RTL	99
C.3	Ground modes	100
C.3.1	RDBWA	100

List of Tables

3.1	Summary of vehicle weights.	17
3.2	Considered aerofoils [54].	19
3.3	Battery characteristics [59, 60].	24
3.4	ESC characteristics [66, 67].	26
3.5	Motor characteristics [66, 67, 70].	27
3.6	Propeller characteristics [66, 67, 73].	30
3.7	eCalc xCopterCalc analysis results for hovering condition.	32
5.1	Power and efficiency (at maximum throttle) experimental results.	59
5.2	Experimental hover forward drag coefficient contributions and totals.	63
5.3	Estimated energy consumption at the maximum speed in hovering flight.	64
5.4	Experimental lateral drag coefficient.	65
5.5	Hover attitude controller metrics.	69
5.6	Forward flight attitude controller metrics.	71
5.7	Ground θ_{max} comparison.	73
5.8	Ground attitude controller metrics ($\theta_{max} = 50^\circ$).	73
5.9	Measured energy consumption.	75
5.10	Estimated maximum range and endurance.	76
5.11	Wing incidence angle comparison in hover ($\theta_{max} = 30^\circ$).	76
5.12	Maximum measured speed (m/s).	77

List of Figures

2.1	Actively actuated multimodal vehicles.	5
2.2	Passively actuated multimodal vehicles.	7
2.3	Lift + Cruise VTOL aircraft.	10
2.4	Tiltrotor VTOL aircraft.	11
2.5	Tiltwing VTOL aircraft.	11
2.6	Tailsitter VTOL aircraft.	12
3.1	DJI F450 frame [50].	14
3.2	Wheel assembly.	15
3.3	3D renderings of the different vehicle configurations.	16
3.4	Different vehicle configurations.	16
3.5	Aerodynamic parts.	18
3.6	Comparison of the considered aerofoils, for $Re = 150000$	20
3.7	3D Plane analysis.	21
3.8	Wing manufacturing process.	22
3.9	Cross-section view of a propeller blade element (adapted from [74]).	29
3.10	Comparison of different propeller pitch values with advance ratio [71].	30
3.11	Vibrations during static tests.	31
3.12	eCalc propCalc analysis results for forward flight condition.	33
3.13	Avionic system components.	35
3.14	Avionics schematic.	35
4.1	UAV model in hover mode.	38
4.2	Roll manoeuvre in hover mode.	38
4.3	UAV model in forward flight mode.	40
4.4	Pitch manoeuvre in cruise condition in forward flight mode (tailsitter configuration).	40
4.5	UAV model for ground locomotion.	42
4.6	UAV model for yaw control in ground mode.	42
4.7	Attitude rate controller diagram.	45
4.8	PID controller diagram.	45
4.9	Attitude angle controller.	47

4.10 Roll/Pitch square root controller output.	48
4.11 Pitch angle controller.	49
4.12 Roll angle controller.	49
4.13 Horizontal position controller.	50
4.14 Vertical position controller.	51
4.15 S-Curve Navigation Profile example.	53
4.16 QHOVER mode.	54
4.17 QLOITER mode.	54
4.18 FBWA mode.	54
4.19 RMANUAL mode.	55
4.20 Ground AUTO mode.	55
4.21 Tailsitter transition.	56
5.1 Wind tunnel propulsion tests setup.	58
5.2 PWM-Thrust map.	58
5.3 Dynamic thrust experimental results.	60
5.4 Wind tunnel mounting.	62
5.5 Wing performance in hover at 20.80 m/s.	64
5.6 Hover 20.80 m/s test.	65
5.7 E169 forward flight performance estimate.	66
5.8 Lift in forward-flight conditions.	66
5.9 Different flight configurations in hove flight.	68
5.10 Attitude controller performance.	69
5.11 UAV in forward flight.	70
5.12 Transition analysis.	70
5.13 Pitch rate controller during both transitions.	71
5.14 Robot in ground locomotion tests.	72
5.15 Ground attitude controller performance.	73
5.16 Ground AUTO mode waypoint test.	74
5.17 Aerial view of the ground waypoint test.	75
5.18 Energy-velocity mapping.	77
5.19 Aerial-ground locomotion.	78
5.20 Wall climb test.	78
A.1 Attitude rate PID controller (v4.5.0).	89
A.2 Vertical position controller (v4.5.0).	89
B.1 L1 loiter controller.	91
B.2 L1 waypoint tracking loop.	92
B.3 L1 waypoint controller.	93

B.4	Pitch TECS control loop.	94
B.5	Throttle TECS control loop.	95
B.6	TECS energy calculation (simplified).	95
C.1	QSTABILIZE mode.	98
C.2	Hover AUTO mode.	99
C.3	FBWB mode.	99
C.4	Fixed-wing AUTO mode.	99
C.5	RDBWA mode.	100

Nomenclature

Greek symbols

α	Angle of attack
α_0	Zero-lift angle of attack
α_{eff}	Effective angle of attack
β	Side-slip angle
γ	Surface inclination angle
η_m	Motor efficiency
η_{prop}	Propeller efficiency
θ	Pitch angle
μ	Fluid dynamic viscosity
μ_{static}	Static friction coefficient
ρ	Density
τ	Torque
Φ	Body frame rotation w.r.t. Inertial frame
ϕ	Roll angle
ϕ_R	Resultant incident airflow angle
ψ	Yaw angle
ω	Rotational speed

Roman symbols

\mathbf{V}_B	Body frame velocity
\mathbf{V}_I	Inertial frame velocity
$\{B\}$	Body frame

$\{I\}$	Inertial frame
$\{V\}$	Vehicle frame
a	Acceleration
B	Number of propeller blades
b	Wing span
c	Wing chord
C_τ	Torque coefficient
C_D	3D Drag coefficient
C_d	2D Drag coefficient
C_L	3D Lift coefficient
C_l	2D Lift coefficient
C_m	Pitching moment coefficient
C_P	Power coefficient
C_T	Thrust coefficient
$C_{m\alpha}$	Pitching moment coefficient angle of attack derivative
D	Drag force
d	Down position
d_{ca}	Aerodynamic centre distance from centre of gravity
D_{prop}	Propeller diameter
d_{rotors}	Diagonal distance between rotors (Frame size)
e	East position
F	Total force
g	Gravitational acceleration
GS	Ground speed
I	Inertia tensor
i	Electric current
i^*	Filtered battery current
I_0	Motor idle current

J	Advance ratio
K_V	Motor speed constant
L	Lift force
M	Propeller figure of merit
m	Mass
N	Reaction force
n	North position
n_{rps}	Rotational speed (rps)
P	Power
p	Roll angular velocity
P_τ	Pitch actuation
p_{prop}	Propeller pitch
Q	Battery capacity
q	Pitch angular velocity
R	Rotation matrix
r	Yaw angular velocity
R_τ	Roll actuation
R_h	Propeller hub radius
R_i	Internal resistance
R_p	Propeller blade radius
Re	Reynolds number
S	Wing area
T	Throttle, Thrust
U	Voltage
v	Velocity
V_∞	Free-stream velocity
V_a	Airspeed
V_R	Resultant incident airflow velocity

V_{ia} Propeller induced velocity

W Weight force

Y_τ Yaw actuation

Subscripts

d Desired

in Input

m Measured

n, e, d North, East, Down components

out Output

p Pilot input

x, y, z Body frame components

Superscripts

' Constrained

Acronyms

- BEC** Battery Eliminator Circuit. 25, 26
- BEMT** Blade Element Momentum Theory. 27–29, 32
- CCW** counter-clockwise. 30, 90
- CEOM** Centro de Experimentação Operacional da Marinha. 67, 73
- CG** Centre of Gravity. 8, 20, 22, 37–39, 42, 61, 68, 72
- CNC** Computer Numerical Control. 22
- CW** clockwise. 30, 90
- EKF** Extended Kalman Filter. 44–46, 94
- ESC** Electronic Speed Controller. xiv, xvii, 17, 23, 25, 26, 31, 32, 34, 59
- FDM** Fused Deposition Modeling. 16
- GCS** Ground Control Station. 36, 70, 99, 100
- IMU** Inertial Measurement Unit. 34, 45
- Li-Ion** Lithium-Ion. 23
- LiPo** Lithium-Polymer. 23, 31
- LW-PLA** Lightweight PLA. 17, 18
- MAE** Mean Absolute Error. 68, 69, 71, 73
- MOSFET** Metal-Oxide-Semiconductor Field-Effect Transistor. 25
- MTOW** Maximum Take-Off Weight. 18, 20
- PETG** Polyethylene Terephthalate Glycol. 16, 17
- PID** Proportional Integrative Derivative. xix, 45, 46, 48, 50, 51

PLA Polylactic acid. 16–18

PWM Pulse Width Modulation. 25, 26, 34, 43, 45, 59

RC Radio Control. 34

RMSE Root Means Square Error. 68, 69, 71, 73

SISO Single-Input Single-Output. 45

TECS Total Energy Control System. xxi, 52, 90, 93–95

UAS Unmanned Aerial System. 34

UAV Unmanned Aerial Vehicle. xiii, xix, xx, 1–5, 9, 10, 12, 13, 16, 21, 23, 25, 28, 33, 34, 37, 38, 40, 42, 43, 46, 47, 49, 50, 61, 62, 64, 66–68, 70, 71, 76, 79, 90, 92, 94–96, 98

VTOL Vertical Take-Off and Landing. xiii, xix, 2, 3, 7, 9–12, 36, 46, 56, 70, 96, 97

Chapter 1

Introduction

This introduction presents an overview of all the work developed within the scope of this work. To lay its foundation, the motivation for developing such a vehicle is presented as well as a very brief overview of the existing technology.

1.1 Motivation

Robots, and in particular aerial robots or Unmanned Aerial Vehicles (UAVs), have continuously shown great potential in executing tasks more efficiently, safely and precisely than humans. Their applications range greatly, and as their applications expand, so do their operating environments. As such, vehicles capable of operating beyond aerial scenarios can provide more applications for UAVs, which have their operation restricted by the distance they need to maintain from the ground, and the energy required to maintain flight. Hybrid vehicles, capable of operating in different environments such as on the ground, in the air, or even underwater not only have their capabilities expanded due to the fact that they can operate in different mediums, but also because of their ability to combine the different mediums in a single operation. This combination enables missions on each of these mediums with stricter requirements. For example, a mission requiring contact with the ground surface on terrain with occasional obstacles is possible due to the vehicle's capability to move on the ground, and to fly over obstacles. For inspection-orientated missions, being able to move on surfaces enables the possibility of performing close inspection with drones. Moreover, and considering the particular case of some ground-aerial multimodal robots (to be later explored in Section 2.2), the combination of the aerial and terrestrial modes enables operations in surfaces with any inclination, with potential applications in the inspection of surfaces of infrastructure such as dams, or other tall buildings.

In addition to the added functionality provided by multimodal vehicles, advantages can also be seen in matters related to energy efficiency. While hovering, all of the weight of conventional multicopters must be sustained by propeller thrust, while conventional fixed-wing aircraft achieve flight by sustaining their weight with lift produced by wings, thus flying more efficiently. The combination of both rotary-wings and fixed-wings may allow for improved flight times, both in hovering flight and in forward flight. By operating

on the ground, at least on flat horizontal surfaces, the need to use energy to sustain the weight of the vehicle is removed, which results in an efficiency improvement. As the great majority of unmanned vehicles use a battery as a power source, which is limited in the amount of energy it can provide, any efficiency improvement results either in an improvement in endurance or range, which enhances the capability of unmanned systems.

1.2 Topic overview

To tackle the challenge of developing multimodal vehicles, several solutions have already been proposed (these will be studied in Chapter 2). For ground-aerial motion, both active and passive solutions are possible, with passive solutions presenting advantages in reduced complexity and weight, due to the necessary additional actuators for active solutions. Vertical Take-Off and Landing (VTOL) aircraft, capable of both efficient forward flight and hovering flight can achieve this multimodality in different ways, potentially requiring either additional actuators or motors, with different impacts on efficiency, and increasing complexity. Of all VTOL aircraft, the tailsitter type can achieve both modes with no additional actuators. To the best of our knowledge, no vehicle fully capable of ground locomotion, hovering flight and forward flight has been documented in the literature. The literature review confirmed that multimodal vehicles can indeed operate more efficiently and in broader operating environments.

1.3 Objectives

The primary goal of this work is to develop a fully capable trimodal aerial-ground vehicle, capable of hovering flight, forward flight and ground locomotion. With this goal in mind, secondary goals were laid out:

- To design and assemble a functional prototype trimodal UAV;
- To improve the operating efficiency with ground operations and forward flight, compared to a base quadcopter;
- To improve the efficiency of the hovering flight mode, considering the base quadcopter as a reference;
- To evaluate the energy consumption of the trimodal UAV in all operating modes;
- To characterise the vehicle's aerodynamic behaviour;
- To implement and demonstrate automatic control in all operating modes.

To meet these objectives, a capable prototype was assembled and manufactured, and the firmware running on the autopilot was made capable of all desired functionalities, including those related to ground movement.

1.4 Thesis outline

The contents of this thesis are divided as follows:

Chapter 2 (State of the Art): In this initial chapter, a review of existing prototypes capable of multimodal operation (focusing on those that operate on land and in the air) is made, as a learning step towards the design of the vehicle this work is focused on. This review is divided by ground-aerial bimodal capability, and within these, those that are passively and actively actuated, and by aerial multimodal operation, where different types of VTOL aircraft are analysed. Lastly, an analysis of where the work developed in this thesis fits in is made.

Chapter 3 (System design): The third chapter details the design process of the developed prototype. First, the structural components are detailed, and a summary of the vehicle's masses is made. Then, the design and manufacturing process of the wings used is detailed. Following that, the choice of components used for the propulsive system is justified, taking into account the theory behind the working principle of each component, with special emphasis on the effect on the efficiency, as it may impact later results. Lastly, the avionic components used are described, and a brief analysis of the firmware used as a base for the autopilot is made.

Chapter 4 (Controller implementation): In this chapter, a description of the control algorithms used on the vehicle is made. First, a brief description of the dynamic model of the vehicle is made, highlighting the differences between the different operating modes. Then, both the existing ArduPilot (which is the selected autopilot software) controllers, as well as those implemented in this work to add ground locomotion functionality are described, using block diagrams. Lastly, the behaviour of the control modes used on the autopilot is briefly described.

Chapter 5 (Experiments & Results): This chapter details all experiments that were made during the development of the vehicle, as well as with the finished prototype. First, the setup used for propulsion tests is detailed, then the obtained results are presented, which were used as support for the design phase. Next, the aerodynamic wind tunnel tests are described, from where results are extrapolated regarding the drag characteristics of the UAV and the forward flight performance, with some performance predictions being made from the wind tunnel data. Lastly, all tests done with the finished prototype are described, with tests done in all three operating modes. The results obtained are presented, namely with regards to the control of the vehicle and its stability, and with a special focus on the vehicle's efficiency and operational characteristics, namely its endurance and range. In the end, the robot's multimodal capabilities are displayed.

Chapter 6 (Conclusions): Lastly, the major conclusions drawn from the results and observations made throughout this work are presented, and some of the major achievements are highlighted. An overview of potential future research and improvements that could be made on this vehicle is also made.

Chapter 2

State of the Art

Most hybrid vehicles are only able to operate in two different modes, such as underwater and in the air [1], underwater and on the ground [2], or on the ground and in the air. Of those that include aerial locomotion, to the best of our knowledge, most of the built prototypes are multicopters, meaning that their ability to fly comes exclusively from moving rotors, which is characterised by a less efficient operation when compared to fixed-wing aircraft.

2.1 Inspection tasks using aerial robots

One of the most common applications of aerial robots is inspection, where a given vehicle is equipped with a given set of sensors, with the objective of collecting data from a specified location. The ability for UAVs to access otherwise inaccessible locations, while keeping risk to human life at a minimum makes them great tools for such tasks. Compared to satellite imagery, they can provide higher resolution data [3]. Moreover, their ability to fly autonomously, or automatically, provides a clear advantage over surveillance using manned aircraft [4]. Current applications of unmanned aerial vehicles are widespread across different industry fields, with applications in agriculture [5], power lines [6], photovoltaic plants [7], forest fire monitoring [8], among others. When working in unknown environments, operational versatility is a big advantage that can be achieved with long endurance, enabling long uninterrupted missions. Moreover, the ability to inspect from a distance, or if needed in close proximity, when more detailed data is required, and the ability to move on different surfaces, contribute to the operational versatility, allowing for general-purpose vehicles.

2.2 Multimodal aerial-terrestrial UAVs

Within land-based inspections, ground-based multimodal vehicles can present numerous advantages. Their ability to move on the ground means that, when required, given areas can be inspected in close proximity and greater distances can be covered in this case. Simultaneously, being able to fly means that large areas can be quickly inspected and obstacles present on the ground can be promptly

overcome. Additionally, the simultaneous usage of both operating modes allows these robots to operate in environments inaccessible to most ground robots and UAVs, such as steeply inclined surfaces.

Hybrid vehicles capable of these two modes can be classified according to the mechanism used for ground locomotion, with actively actuated designs using dedicated actuators for this purpose, and passively actuated designs relying on existing UAV actuators.

2.2.1 Actively actuated designs

In this category, in addition to the actuators required for flight, other actuators are employed to enable the vehicle to move on the ground. Within this category, different mechanisms are implemented to enable ground locomotion, such as tilt-rotor designs, tracked vehicles and active wheel drives, among others. One such tilt-rotor design is the Multi-Modal Mobility Morphobot (M4) [9]. This design consists of a vehicle with four independent legs, each equipped with wheels that incorporate propellers in their interior. The objective of this vehicle is to achieve different mobility modes, which it does successfully, at the cost of an increased actuation complexity. To implement the 8 different modes it is capable of operating in, this system requires four propellers, and their respective motors, four wheel motors to drive the wheels, and eight hip servos, required to control the rotation of each of the legs, with two servos on each leg. This additional complexity is in turn translated into extra weight which is not useful for all modes, resulting in sub-optimal efficiency. Still, despite its great versatility, this vehicle only claims the ability to climb surfaces with a slope as high as 45° . In Figure 2.1(a) the M4's operating modes are described. A simpler tilt-rotor design is presented in [10], where only the two front motors of a quadcopter tilt to provide forward thrust. The frame then uses four passive wheels to move on the ground.

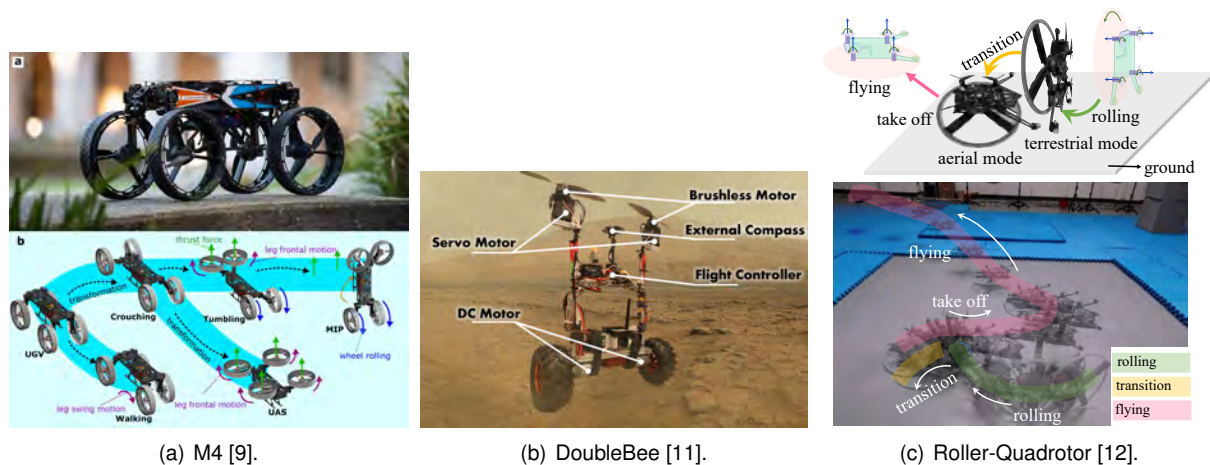


Figure 2.1: Actively actuated multimodal vehicles.

It is also worth mentioning the solution provided in [13], a highly complex solution with ten actuators, which in turn is able to perform highly complex manoeuvres. A simpler solution in [14] reduces the number of actuators by using the same motors for both driving the wheels and powering the propellers. Using a servo, the arms upon which the motors are assembled can tilt, enabling the proper contact of the wheel with the ground. A gearbox, fitted to the two rear wheels, connects the existing motors to the wheels, thus

driving them with adequate torque and rotational speed. No power consumption results were provided, however, the addition of the gearboxes on the rear wheels, which are driven simultaneously, represents a 2.5% increase in overall power consumption. Likely, on the ground, driving the propellers at the same time has a worse effect and, as such, the vehicle could benefit from a mechanism to disengage the propellers.

A simpler approach to actively actuated ground modes was taken in [15], in which a simple quadcopter frame was combined with a rover frame, providing complete separation between modes. Four conventional propellers and motors power the flight mode, and four motors and wheels are responsible for the ground modes. The full separation between modes facilitates the development of control strategies, as existing strategies for each mode can be used with little to no modification. However, the extra number of actuators and supporting structures make the robot heavier, and less aerodynamic. It is nonetheless a simple to implement solution.

In contrast to this simple solution, [11] proposes a design using only two propellers (and corresponding motors) and two motors for wheel propulsion. Additionally, the two flying motors have their pitch angle controlled by a servo motor each, allowing for thrust vectoring of these motors. In aerial mode, the rectangular structure upon which the motors are assembled flies upright, using the tilt of the motors to control pitch and yaw, and the differential thrust to control roll. On the ground, the structure can fly at any given angle, given the possibility of tilting the flight motors, which balance the vehicle when driving at an angle. When driving completely upright, the propellers are not required to move the vehicle. A decrease in power consumption on the ground was observed in this vehicle, although not significant, as all actuators are required on the ground to maintain stability. In Figure 2.1(b), the DoubleBee's actuators are described.

In [12], a simple actively actuated solution is proposed with a single extra actuator for ground locomotion. In this solution, the additional weight required for ground locomotion is minimised compared to even some passively actuated solutions, as it only involves adding a wheel onto an existing quadrotor frame, and a motor to drive it. This design is described in Figure 2.1(c). This simplicity, however, comes at a cost, given the fact that ground locomotion is driven by a unicycle, the controller for ground movement requires the simultaneous actuation of all motors. Additionally, transitioning from aerial to ground mode is not seamless and requires precise actuation to prevent the vehicle from tilting over. During ground locomotion, precise control is also required, which may result in reduced stability on uneven terrain or in windy conditions. It does however provide an advantage for travelling down narrow paths, where this vehicle excels. Lastly, although the robot boosts an exceptional increase in run time while on the ground (41.2 times more than in the air), the increase in range on the ground is much smaller, only 2.8 times greater than in aerial mode.

Lastly, in [16], a multimodal package delivery tailsitter, with terrestrial motion capability is proposed. For ground movement, three landing gear wheels are actuated using electric motors, which enable yaw control on the ground. For flight, an electric ducted fan concept is used to generate thrust. For hovering flight, a simple upward force is produced, lifting the vehicle for take-off and landing manoeuvres. Then, for forward flight, a folding wing unfolds, using servos, and the aircraft rotates, such that the wing generates lift. The addition of forward flight capability contributes to the efficiency of the vehicle in-flight. To the

best of our knowledge, this is the only vehicle combining dedicated ground locomotion, Vertical Take-Off and Landing (VTOL) and forward-flight capability, and still, only a conceptual design is proposed, with no simulations or prototypes having been developed.

2.2.2 Passively actuated designs

Unlike the actively actuated designs, passively actuated designs rely solely on the existing flight rotors to move the robot in all modes. Such can be achieved with the implementation of mechanisms that typically introduce an additional degree of freedom to the frame upon which the rotors are assembled onto. In Figure 2.2 some of the vehicles that will be described are presented, highlighting the main types within this category.

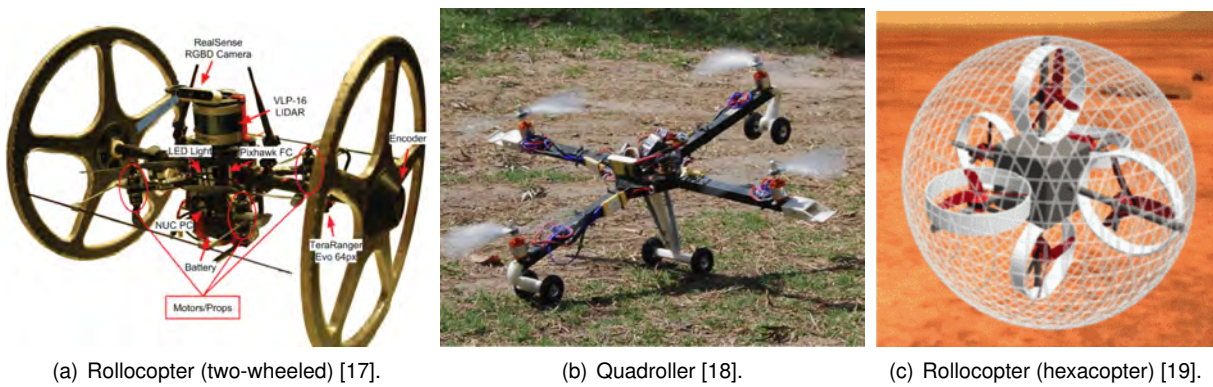


Figure 2.2: Passively actuated multimodal vehicles.

One such mechanism involves the implementation of a cage around a conventional quadcopter. This design was detailed in [20]. With this setup, a cage surrounds the entire quadcopter, being joined to it by two arms connecting it to the centre of the frame. In between the two arms and the cage, bearings can be found, which allow the cage to rotate independently around the drone. This means that when on the ground, the quadcopter can rotate freely around the pitch axis. It is this ability that allows the vehicle to move on the ground. By pitching forward (or backwards), the thrust produced by the propellers is directed both upward and in the desired forward or backward direction, allowing the vehicle to move accordingly. In order to change its orientation, differential thrust is used, as it would be used to control the yaw angle of a common quadcopter in the air. In this particular case, since the cage completely surrounds the vehicle, that can become an obstacle to any sensors that may be integrated onboard, such as cameras for inspection. Additionally, the cage has a higher aerodynamic footprint, resulting in increased drag. However, the large surface area in contact with the ground means that this vehicle exhibits higher stability on the ground, compared to other alternatives. Lastly, it is worth mentioning the fact that the vehicle is unable to maintain a full 90° pitch angle on the ground, meaning that part of the thrust generated is useless to the ground movement, especially on flat surfaces. With this, an increase of 6 times in operating time, and 4 times in distance covered was observed when comparing the ground mode to aerial movement.

Similarly, in [17] a design is presented following the same principle, but without the usage of a cage,

as seen in Figure 2.2(a). Instead, only two wheels are used, connected to the centre frame in a similar manner, using a main shaft. By not employing a cage, the aerodynamic footprint of the vehicle is improved, as well as the visibility of any sensors that could be implemented onboard. Still, such solutions applied to larger platforms, which typically require larger propellers, require a significantly larger wheel size. When increasing the wheel size, its stability can become compromised, which can make ground locomotion more difficult, due to the loss in rigidity of the wheel. In this work, a wheel made of a light carbon fibre honeycomb structure is presented, which can yield a wheel that is light, while maintaining sufficient structural integrity. An improvement of over 5 times was reported in power consumption. Both caged and 2-wheeled solutions present easy to implement control strategies, given the shared controllers for both hovering and ground modes.

Unlike the previously analysed vehicles, in [18] a passive solution using more than two wheels is proposed. The Quadroller uses two pairs of two wheels, as shown in Figure 2.2(b), mounted at the end of two opposing arms of the quadcopter, and two additional wheels, mounted further away from the frame, in its centre. The result is a conventional quadrotor, which when landed on the ground sits at an angle. With this inclination, part of the thrust produced is directed forward, and as such, forward ground locomotion is possible. To control the heading of the robot, a mechanism using springs gives partial freedom of motion to the vehicle on its roll axis, which combined with a skateboard steering truck on its front wheels, enables the vehicle to change its yaw angle, by rolling. Such a vehicle, however, is not able to roll on steeper surfaces, being limited to flat terrains. Additionally, its low angle means that while moving on the ground, a significant part of the thrust produced is not directed towards moving on the ground, making this vehicle not as efficient as other alternatives, only achieving an over 3 times increase in operating time.

Lastly, in [19], an innovative passive solution is proposed which does not resemble conventional multicopters, as seen in Figure 2.2(c). In this work, a vehicle with three pairs of rotors, each aligned with one of the main axes of the vehicle, surrounded by a spherical cage is proposed, giving it freedom of movement on all axes. While on the ground, the spherical cage rolls like a ball, enabled by its rotors. Given its complex rotor configuration, control strategies for such a vehicle are different from the existing ones used in other multicopters. Still, an improvement in power consumption while rolling compared to flying was observed, although this improvement drastically diminishes when compared at higher speeds. It is also worth mentioning that a prototype was not built and that results are from simulations exclusively.

In [21], a quadcopter built into a wheel is proposed, similar to [12], but with a larger wheel area and with its Centre of Gravity (CG) inside it, providing higher stability. Rather than introducing a motor to drive the wheel, no extra actuators are present, meaning the only actuators are the flight rotors. A passive elastic mechanism for two of the motors was designed where, while on the ground, less thrust is required, two of the motors generate thrust radially, with respect to the wheel. Thus, two of the motors generate a torque, which makes the wheel roll. The system is, however, unable to control the direction towards which the vehicle is rolling, once it is in rolling mode. Once again, transition is far from trivial and requires a change in pose on the ground. No power consumption results are presented, however, given that the thrust generated is almost all directed towards generating movement, efficiency results could be promising.

2.3 Air based multimodal UAVs

Unmanned aerial vehicles (UAVs), more specifically heavier than air aircraft, can be classified according to their means of generating lift. Rotary-wing aircraft, generate lift using rotating wings, also called rotors. Such vehicles can exhibit a varying number of rotors, with both helicopters and multicopters included in this category. The main advantage resulting from these aircraft is their ability to hover, which can be of great interest for some inspection tasks. In addition, their ability to hover also means that take-off and landing are performed vertically, thus meaning operations can take place in areas where a runway (or similar) is not available. Nonetheless, the need to rotate the wing to generate lift implies a constant energy consumption during flight. Currently, most commercially available consumer UAVs fall into this category. Fixed-wing aircraft, on the other hand, rely on airflow over a fixed wing to generate lift. This means that unlike rotary-wing aircraft, they cannot hover and require a given length to take-off, as flight is only possible above a given airspeed. As lift is generated exclusively by aerodynamic means, these aircraft are more efficient, boasting higher range and operating time, and are typically able to achieve higher speeds.

Some operational scenarios, however, require characteristics from both of the categories. For example, a fire monitoring vehicle requires the greater range and operating time from a fixed-wing aircraft, in order to be able to cover a large area, but at the same time, given the fact that areas where such a vehicle might be deployed lack the proper conditions for a fixed-wing to take-off, it might require the ability to vertically take-off and land. As such, although helicopters and multicopters are capable of vertical take-off and landing, aircraft able to fly in both modes are commonly called VTOL aircraft.

VTOL aircraft can then be classified according to the mechanisms or manoeuvres required for transitioning from hovering flight to cruise flight (and vice-versa), with each type having its particular advantages and disadvantages with regards to energy efficiency, complexity, and control difficulty.

2.3.1 Lift + Cruise VTOL

A Lift + Cruise VTOL consists of a fixed-wing aircraft with separate propulsion for each of the modes. One of the most common configurations consists of fixed-wing aircraft, with either a tractor or pusher motor generating thrust in the forward direction and four motors mounted on booms, generating upward thrust. The need for separate motors usually means that these configurations have heavier propulsive systems. However, the separation between modes means that propellers can be chosen for each mode which maximises the efficiency, as the thrust requirements and incident airflow velocity are different. For the vertical propulsion system, the incident airflow velocity can be considered null, whereas for forward flight, the propulsive system should be optimised for the cruise speed of the aircraft. Additionally, the possibility of producing thrust in both directions during the transition between modes, usually means that control of the vehicle during transition is easier to maintain. One design aspect worth mentioning in aircraft of this type is the positioning of the cruise motor, which can be placed either in a tractor configuration, at the front of the nose, or in a pusher configuration, at the rear of the fuselage. Choosing the appropriate configuration will depend on the specific aircraft design at hand, as both can have their

advantages and disadvantages. In conventional fixed-wing aircraft where the rotors are mounted on the wings, mounting the propellers in a tractor configuration can help increase lift generated by the wing, although accompanied by an increase in drag [22, 23]. Examples of such aircraft are the UAVision Ogassa OGS42V [24], the Tekever AR3 [25], the Beyond Vision VTOne [26], the Elka1Q [27] and the Evolonic NF3 [28], using pusher motor configurations, and the Emergency Response UAV developed in [29], which employs a tractor motor configuration, less common in this type of VTOL. Some of these aircraft can be seen in Figure 2.3.

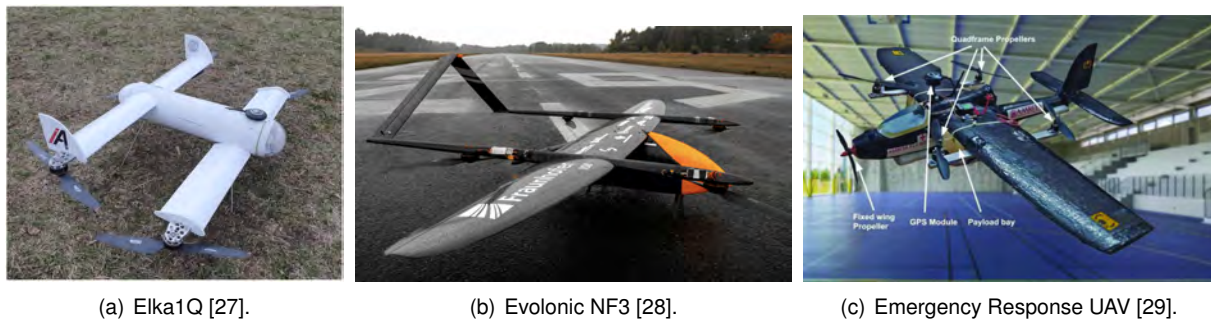


Figure 2.3: Lift + Cruise VTOL aircraft.

2.3.2 Tiltrotor VTOL

A tiltrotor VTOL consists of a fixed-wing aircraft where the same rotors are used to provide lift in vertical flight and forward thrust in cruise flight. This can be achieved by implementing a tilt mechanism in some or all of the rotors used to generate lift. Different configurations exist for such vehicles, ranging from tricopters to vehicles with a higher number of rotors and with varying numbers of tilting rotors as well. Two very common configurations are that of a simple quadrotor, with the two forward rotors tilting forward [30], or less frequently with all four rotors tilting [31], and the tricopter configuration, with the forward motors tilting [32], or all rotors tilting [33]. One of the major disadvantages of tiltrotor UAVs is the inability to simultaneously maximise efficiency in forward flight and hovering flight when designing with a fixed-pitch propeller. This is due to the fact that propeller pitch is largely associated with the incident airflow speed. A variable pitch mechanism can be introduced, however, for most small-scale applications, the increase in complexity and weight significantly outweighs the increase in propeller efficiency [34]. Another aspect worth mentioning is the need for extra actuators required for the tilting mechanism, which represents an increase in system complexity, and introduces an additional point of failure. Nonetheless, a vehicle can be designed bearing in mind the potential failure of actuators, in order to ensure the aircraft remains controllable [35]. On the other hand, the implementation of additional actuators enables the usage of more complex and interesting control strategies, leveraging the use of thrust-vectoring for attitude control of the vehicle [36]. Many different control strategies are available for the transition phase [31, 37, 38], however, there is a general consensus about the goals, which are to maintain altitude during the transition, and to keep a stable, level attitude. In Figure 2.4, some examples of tiltrotor aircraft are presented.

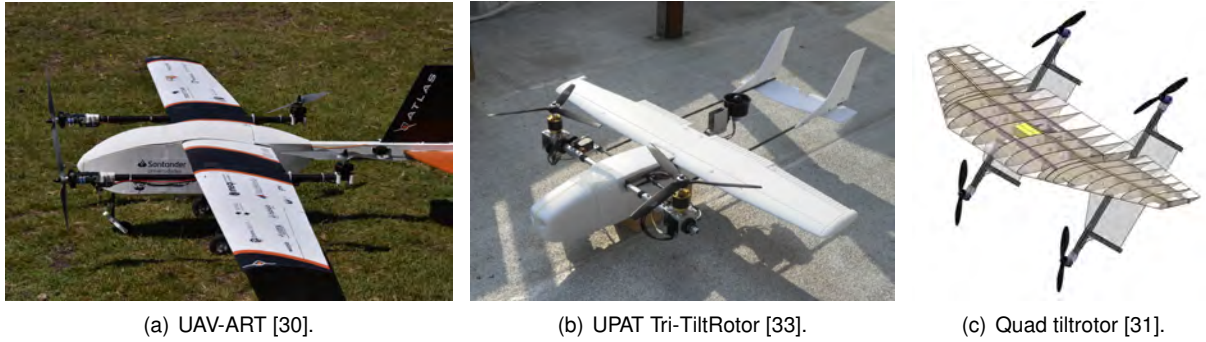


Figure 2.4: Tiltrotor VTOL aircraft.

2.3.3 Tiltwing VTOL

A tiltwing VTOL employs a similar technique to a tiltrotor aircraft, but instead of only tilting the motors, the entire wing is rotated. As such, these aircraft typically make use of the wing for mounting the motors, which serve both hover and forward flight modes. Given the preference for quadcopters in hover flight, a common configuration for a tiltwing VTOL is a quad tiltwing, consisting of two wings, each equipped with two motors, as demonstrated in [39, 40]. Alternatively, configurations with non-tilting rotors are also feasible [41]. Since the rotors are mounted on the wings, airflow passes over the wing during hover mode, allowing the use of control surfaces on the wing and providing an advantage over tiltrotors. Still, compared to a tiltrotor, the actuator required to rotate the wing is significantly more complex, and the failure of this mechanism can lead to a more catastrophic outcome, compared to the failure of the tiltrotor actuator [42]. Still, the usage of rotors that impact the airflow over the wing in cruise flight means that a wing can be designed to take advantage of this fact, leading to more efficient cruise flight. Examples of the most common configurations of this type are presented in Figure 2.5

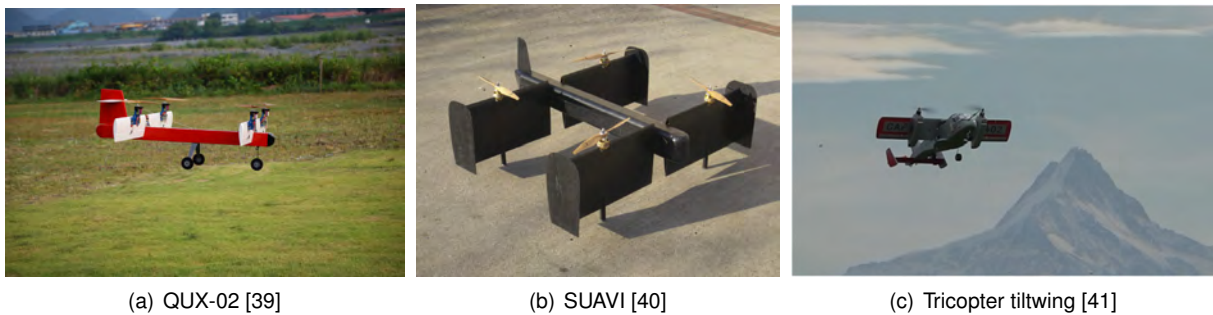


Figure 2.5: Tiltwing VTOL aircraft.

2.3.4 Tailsitter VTOL

A tailsitter VTOL, similarly to the tilt-rotor, uses the same motors for both generating lift in vertical flight modes and producing horizontal thrust in cruise, however, instead of using actuators to control the tilt angle of some of these motors, the whole vehicle tilts during the transition, thus not requiring any additional actuators. Within this category, many different designs are presented, ranging from vehicles with no control surfaces, vehicles using thrust vectoring techniques, and tailsitters using conventional

aerodynamic control surfaces [42]. Among those employing control surfaces, a bi-motor flying wing with two elevons is one of the most common designs, even found commercially available [43]. All actuators are used for attitude control in both flight modes [44]. On the other hand, designs with no aerodynamic control surfaces present simpler solutions, such as a simple conventional quadcopter, with an added wing for lift generation in forward flight. Most commonly, a bi-plane configuration is implemented, as in [45, 46], where a three times power requirement decrease from hover to forward flight could be observed. Control of such a vehicle relies solely on differential thrust and torque. On top of this base platform, different features can be implemented, such as a variable propeller pitch mechanism [47], which can decrease the power requirement for different values of vehicle operating airspeed in forward flight. Another option is the incorporation of swivelling wings [48]. More unconventional configurations are also available like the NederDrone [49], a hydrogen-powered tailsitter with 12 motors. Lastly, the vehicle previously discussed in [16] is also a VTOL tailsitter. Although they boast a key advantage in simplicity, tailsitter aircraft can be more susceptible to wind disturbances in hover flight, leading to this mode being more challenging to control and less efficient, when compared to other VTOL configurations [42]. Some common tailsitter configurations are presented in Figure 2.6.

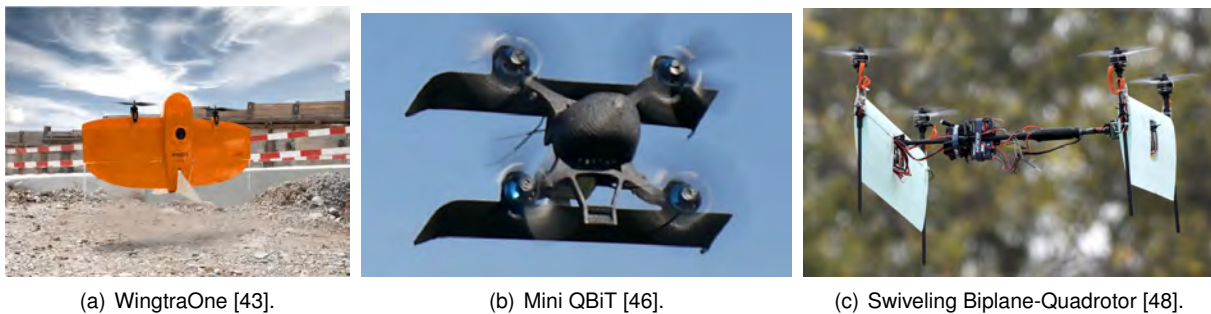


Figure 2.6: Tailsitter VTOL aircraft.

2.4 Review Summary

Taking into account all the previously analysed hybrid UAVs, there is a clear lack of a simple and efficient solution, capable of both ground and aerial locomotion, while maintaining the same set of actuators and control laws for all modes, and flying in a more efficient manner, with a fixed wing. The closest vehicle, proposed in [16], can both hover, fly horizontally, and move on the ground, but requires additional and complex actuators to achieve so. Additionally, that work only proposes a design, with no prototype having been built or tested.

Given the fact that this work aims to implement a trimodal UAV platform, in order to minimise weight and complexity, the number of actuators should be minimised. As such, to implement ground locomotion a passive wheel mechanism can be used, that enables the vehicle to freely rotate around the pitch axis. Moreover, for fixed-wing flight tailsitter aircraft showed the most potential for a passive solution, allowing for control exclusively with existing quadcopter motors. Among those, a biplane tailsitter allows the vehicle to maintain its symmetry and maximises the wing area within the available space in between the wheels.

Chapter 3

System design

Given the previously identified research gap, the objective of implementing a vehicle both capable of ground and aerial locomotion, while also presenting a more efficient flight mode option was set. The main goal of this work is to implement a multimodal vehicle, capable of ground locomotion, in both flat and inclined surfaces, and aerial locomotion, in both hovering and in cruise flight. In this chapter, the process of designing the structural components of the UAV and its aerodynamic surfaces (wings) and choosing the components of the propulsive and avionic systems will be detailed.

3.1 Structural design

One of the main reasons such a vehicle can be beneficial, besides its versatility, is its potential for energy efficiency. As such, one important objective to accomplish this is minimising weight. To achieve this, the design prioritises the use of a single set of actuators for all operating modes. This eliminates the unnecessary weight of additional actuators and allows for a passive ground actuation mechanism. For forward flight capability, a tailsitter design with no aerodynamic control surfaces was chosen. This approach requires less weight to be implemented and reduces the complexity of the system. Since wings will be used, a non-caged design would have to be used, as a cage around the vehicle would disrupt the airflow over the wings, thus decreasing their performance. In addition, a cage could block potential sensors to be installed onboard, and would therefore make this UAV unusable for inspection missions for example.

3.1.1 Frame

A multicopter X frame forms the base of the vehicle, for its common availability, control simplicity, and increased efficiency, compared to configurations with a higher number of motors. In addition, this design can produce rotational torque in all 3 axes of the vehicle, as well as generate thrust, crucial for controlling the vehicle on the ground and in both aerial modes, thus fulfilling the objective of using the same set of actuators for all operating modes. An increase in motor count would represent an increase in cost, weight,

and power consumption. Finally, given the two-wheeled design, which will be explained next, a fully symmetric frame facilitates the assembly of wheels onto the frame, without reducing ground clearance.



Figure 3.1: DJI F450 frame [50].

The DJI F450 frame [50] was chosen as the quadcopter frame. It is comprised of two central plates, used to mount the avionics, and four arms connected onto the central plates, at the end of which a motor is mounted. Although the prototype is not designed for a specific payload, the 450 mm motor-to-motor diagonal distance of the F450 is sufficient for most commonly used sensors. In Figure 3.1, the DJI F450 frame is presented, where

the red arms indicate the forward direction and the white arms indicate the backward direction. The bottom plate also serves as a power distribution board, used to distribute power to the four motors.

3.1.2 Wheels

Two passive wheels are attached to the main quadcopter frame, serving as landing gear, ground contact points, and propeller protectors. When sizing the wheel, there are two important parameters to consider, its diameter and its distance to the centre of the frame (or track width). The diameter of the wheel should be such that the whole internal frame can rotate freely without any propellers touching the ground. As such, the wheels should be able to accommodate the chord of the wings. Lastly, the track width should accommodate the wingspan and allow free propeller rotation. It is worth bearing in mind however that a larger diameter wheel requires additional reinforcement to maintain rigidity, and represents an increase in weight. Similarly, a greater track width allows for a larger wing, at the cost of increased inertia, a negative aspect for control.

Regarding the structure of the wheel, a thinner profile reduces the aerodynamic drag in forward flight, however, it also decreases the contact area with the ground in ground locomotion, leading to a less stable support, which makes the wheel more susceptible to bending in turns. When designing the spokes, which give the wheel rigidity, ideally the surface area should be minimised, as it will increase lateral aerodynamic drag, and make controlling the vehicle in the air harder.

With the resources available, a wheel could not be manufactured from scratch. As such, a wheel made out of an aluminium grill was used, comprised of an outer rim made of sheet metal and an interior made of a mesh. To reinforce it, and provide an assembly point to the axle, four carbon fibre spokes are attached to the outer rim and the central hub. These are made from unidirectional (all of the fibres are oriented along the length of the tube) carbon fibre tubes with 4 mm external diameter and 3 mm internal diameter. In Figure 3.2, one of the wheels is presented. A wheel diameter of 600 mm and a track width of 600 mm were used. The wheel has a thickness of 4 mm and a mass of 326 g.

To connect the wheels to the main frame, a carbon fibre tube with 12 mm external diameter and 10 mm internal diameter is used. On the side of the main frame, a 3D printed plastic part is used, to which

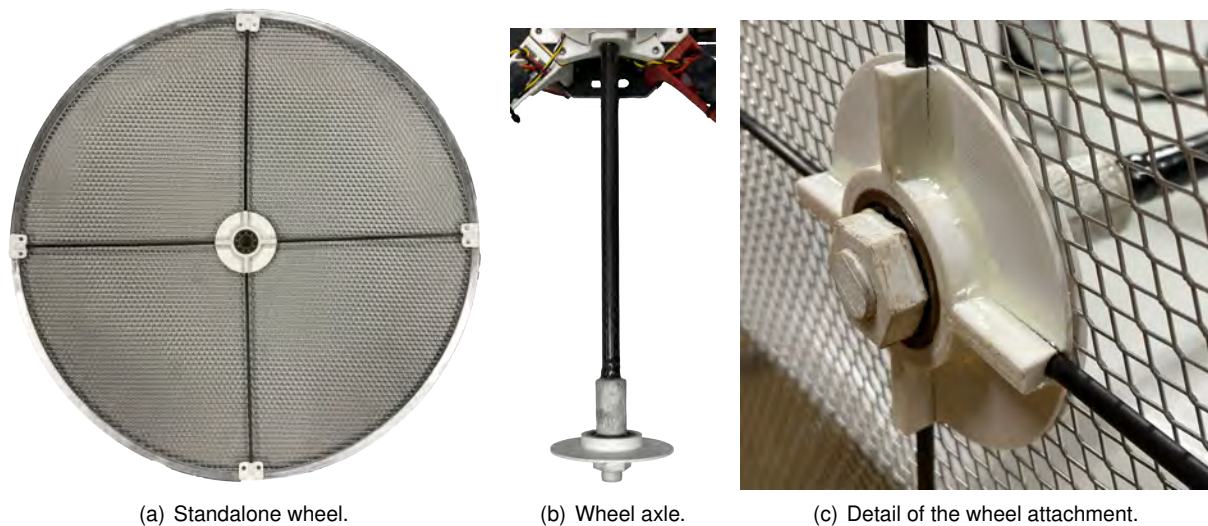


Figure 3.2: Wheel assembly.

the carbon fibre tube is glued. This plastic piece follows the shape of the main frame and is bolted into it. On the other end of the tube, another plastic part is glued onto the tube, to enable the assembly of the wheel. Around this part, a bearing is fit, around which a plastic plate is fit, that will serve as the stop point of the wheel on the axle. This plate can freely rotate, as it will be in contact with the wheel. In Figure 3.2(b) the fully assembled axle is presented. A similar hub can be found in the wheel (see Figure 3.2(c), where the spokes connect, with a bearing as well.

To lock the wheel in position, a nut screws into the axle, pressing both plates together and allowing for the wheel to freely rotate while remaining stable. The plastic part at the end of the carbon tube was threaded using an M14x1.25 threading die. Similarly, an M14x1.25 nut would be needed, however, conventional steel nuts would be too heavy and unnecessarily strong, and nylon nuts were difficult to acquire, so a hexagonal nut was 3D printed in the same material as the axle, and using a taper tap, a thread was applied onto it.

One aspect worth mentioning is that a larger internal diameter bearing is preferred to minimise play in the bearing and ensure stable ground locomotion. A 16002 ball bearing was used, with 32 mm external diameter and 15 mm internal diameter. Previously, a smaller bearing (and axle) diameter was tested, which proved to be more unstable on the ground. The attachment mechanism is displayed in Figure 3.2(c).

This design allows both wheels to be removed by simply unscrewing two nuts, meaning that for missions where ground locomotion will not be required, the wheels can be removed for improved aerodynamic efficiency and reduced weight. Given the wheel's shape and position, symmetry is maintained.

3.1.3 Wings

To attach the wings, a simple mechanism needed to be devised, allowing for a simple assembly, that permits quick removal for missions when forward flight capability is not required (thus once again improving the hovering stability), but still ensuring that the wings are firmly held in place during flight. As will be discussed in Section 3.2, the wings should be placed in line with the rotors. As such, the legs of

the F450 frame below each motor can be used as a mounting point. With that in mind, a plastic part was designed that follows the shape of the aerofoil along a portion of its chord, with this serving as a surface to glue the attachment onto the wing, which then features a negative version of the pattern found on the F450's legs. With this, assembly is as simple as fitting the wing onto the F450 frame. Still, given the 90° angle the legs make with each other, the fitting is secure, as each wing is held on by two legs, and the forces required to remove each fitting are perpendicular. Lastly, this mechanism permits easy swapping of the wings, thus enabling the testing of different aerofoils on this platform. In Figure 3.5(a) the wing attachment part is presented, for the two aerofoils selected in Section 3.2.

3.1.4 Assembly

All previously mentioned plastic parts were manufactured using Fused Deposition Modeling (FDM), an additive manufacturing technique commonly referred to as 3D printing, of Polylactic acid (PLA) and Polyethylene Terephthalate Glycol (PETG), unless otherwise stated. Both materials were used according to availability. All glued junctions, unless otherwise stated, were glued using 5 minute epoxy resin.

In Table 3.1, the weights of all the previously chosen and designed components are listed, as well as of the components to be defined in Sections 3.2 and 3.4. The total weight of the vehicle in different configurations is also presented, in a Quadcopter mode, corresponding to the simple quadcopter, in a Tailsitter configuration, where the wings are attached to the frame, in a Ground configuration, where only the wheels are assembled, and lastly in the Full vehicle configuration. To facilitate the design of the 3D printed parts, a 3D model of the vehicle was also developed, from which the renderings in Figure 3.3 were obtained. In addition, the different flight configurations of the UAV are presented in Figure 3.4.

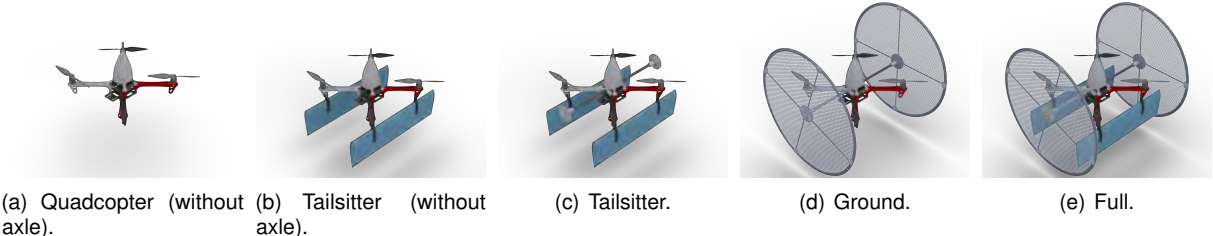


Figure 3.3: 3D renderings of the different vehicle configurations.

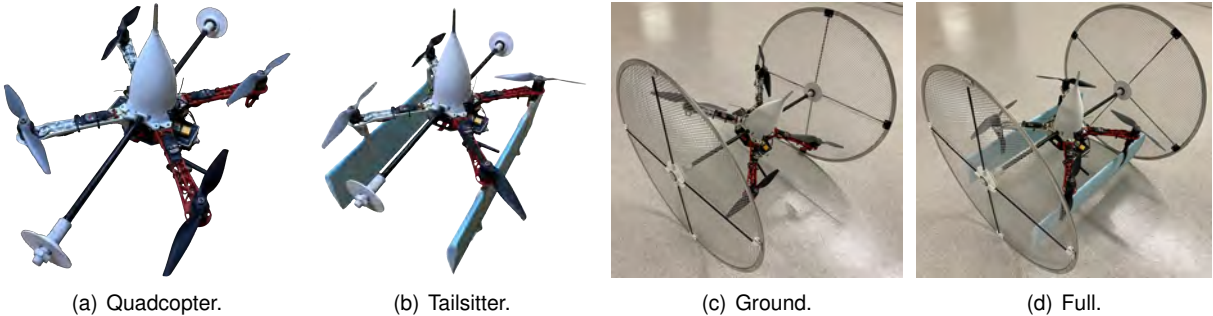


Figure 3.4: Different vehicle configurations.

Table 3.1: Summary of vehicle weights.

Subsystem	Component	Material/Model	Mass (g)
Structure			297
	F450 frame	PA66+30GF	282
	Nose canopy	LW-PLA	15
Propulsion			830
	Motors	DJI 2312E	60 (x4)
	ESC's	T-Motor AIR 20A	14 (x4)
	Propellers	APC 9x6E	17 (x4)
	Propeller nuts	Steel	8 (x4)
	Battery	Gensace Bashing	434
Avionics			166
	Flight controller	CubePilot CubeOrange	75
	GNSS module	Here+V2 GPS	49
	Power module	-	14
	Airspeed sensor + Pitot	-	15
	RC Receiver	FrSky RX6R	3
	Telemetry	Holybro Sik Telemetry	10
Wheels			964
	Bearings	PFI 16002	27 (x4)
	Wheel hub (axle side)	PETG	17 (x2)
	Wheel axles	Carbon fibre + PETG	82 (x2)
	M14 nut	PETG	3 (x2)
	Wheels	Aluminium + PETG/PLA + Carbon fibre	326 (x2)
Wings			126
	Attachment	PLA/PETG	12 (x4)
	Aerofoil	XPS	39 (x2)
Vehicle Configuration			Total Mass (g)
	Quadcopter (without axle)		1293
	Quadcopter		1551
	Tailsitter (without axle)		1419
	Tailsitter		1677
	Ground		2257
	Full		2383

3.2 Aerodynamic design

In this section, the design process of the forward flight mode will be described in detail. Firstly, given the adopted quadcopter frame, which provides control over all axes of the vehicle, and the objective of using a common set of actuators for all modes of locomotion, a design with fixed aerodynamic surfaces and no movable control surfaces was chosen. Taking advantage of the square frame and motor positioning, a biplane design is the optimal choice that can maintain a symmetrical vehicle. Positioning the propellers in a tractor configuration relative to the wings has been shown to increase the lift-to-drag ratio [51]. A biplane can also fit a higher wing area with the same wheel track width.

Although vertical stabilisers could be added forming a square box wing, they might reduce hovering stability in windy conditions due to the added wetted area. As such, no vertical stabilisers were implemented, leaving the stabilisation up to the differential thrust of the motors, and respective attitude controller. This approach has the disadvantage of using additional energy for stabilisation, reducing the

margin left for acceleration in forward flight. The design process of the biplane wings is described next.

In addition to the wings, a nose canopy was designed to reduce the drag of the main frame in forward flight, protecting the avionic components, and providing a mounting point for the pitot tube. No particular aerodynamic analysis was performed, nonetheless, a shape was designed resembling a streamlined body. Since the only force acting on the nose during flight is aerodynamic drag, a thin shell profile was used without internal structure to house the avionics components and minimise weight. An initial version was designed and tested, however, in wind tunnel testing that will be detailed later on in Section 5.2, flow deceleration was observed at its top (likely due to the impact of the frame and canopy), where the pitot tube is assembled, thus meaning the airspeed sensor would provide unreliable readings. To fix that, a more elongated nose was designed, such that the pitot tube would be further away from the frame. To attach the nose to the frame, the legs are screwed into the existing screw holes in the frame. The final design, shown in Figure 3.5, was printed in Lightweight PLA (LW-PLA), a lighter version of PLA, which allowed for a reduction in weight of up to 67% [52], as this is not a structural component.

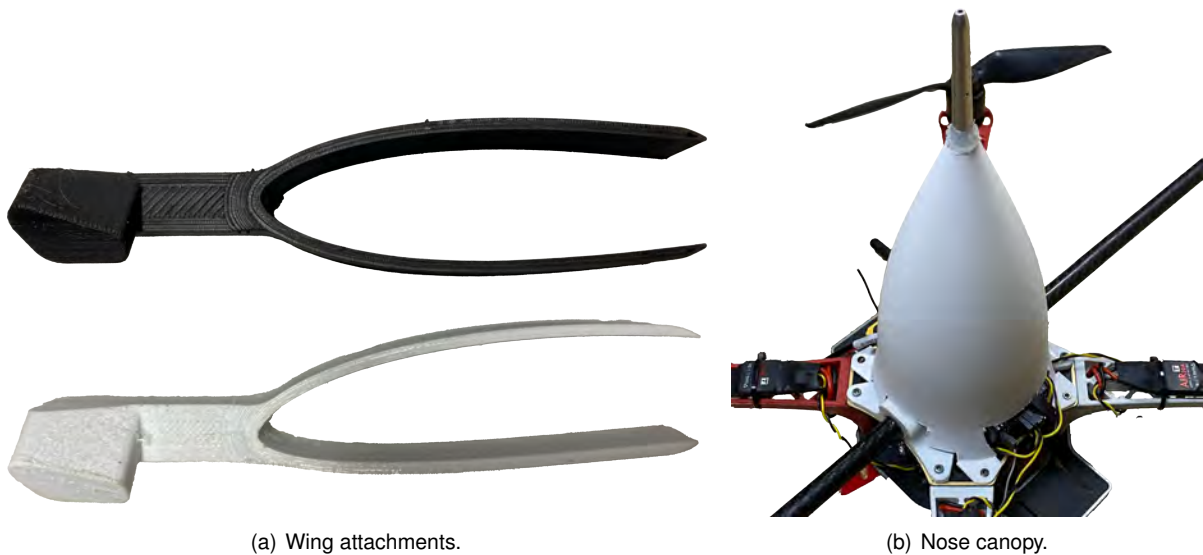


Figure 3.5: Aerodynamic parts.

3.2.1 Operating conditions

In the design process, the following conditions and limitations were taken into consideration as an initial estimate:

1. A Maximum Take-Off Weight (MTOW) of 2200g;
2. A cruise airspeed of 15 m/s;
3. A maximum wingspan of 56 cm, limited by the track width of the wheels;
4. A chord of 15 cm, limited by the diameter of the wheels;

With these conditions in mind, the first approach was to only consider symmetrical aerofoils, as a cambered aerofoil could produce lift during hover, due to the flow over the wings generated by the propellers [53]. Estimating the lift generated by an aerofoil due to this flow is a complex task, beyond the scope of this work.

Two important dimensionless variables are defined, the Reynolds number, Re , and the lift coefficient, C_L ,

$$Re = \frac{\rho V_{\infty} c}{\mu} \quad (3.1a)$$

$$C_L = \frac{2L}{\rho V^2 S} \quad (3.1b)$$

where ρ is the air density, V_{∞} is the free stream flow velocity, c is the wing chord, μ is the dynamic viscosity of the air, L is the lift force and S is the total wing area. The Reynolds number helps characterise a given flow's behaviour, while the lift coefficient is a dimensionless quantity that relates the lift generated to some fluid and wing properties.

Using the design operating conditions, a Reynolds number (at sea-level, 20° C) of $Re = 148898$, and a lift coefficient of $C_L = 0.9488$ were obtained, corresponding to the cruise flight condition, meaning level flight. The reference area considered was the total rectangular area of both wings. Next, for the purpose of aerofoil selection, disregarding the 3D flow characteristics, the 3D lift coefficient was considered to be equal to the 2D lift coefficient, i.e. $C_l = C_L$, when in fact $C_L < C_l$, and this is therefore an overestimation of the aerofoil performance, specially considering the low aspect ratio of each wing of 3.7.

3.2.2 2D aerofoil design

A search was conducted on the popular website Airfoil Tools [54], considering only symmetrical aerofoils, with the goal of maximising the peak $\frac{C_l}{C_d}$ ratio, at a Reynolds number of 200000. From there, the following aerofoils were considered, from the Eppler series aerofoils, the E168 and E169, and from the NACA series, the NACA0012 and NACA63-012A. In addition, a non-symmetrical aerofoil was considered, the Eppler E396, with the goal of evaluating its true impact in hovering flight. In Table 3.2, the characteristics of the considered aerofoils are presented.

Table 3.2: Considered aerofoils [54].

Aerofoil	E169	NACA0012	E168	NACA63-012A	E396
Max. thickness (%)	14.4	12	12.4	12	13.1
Max. thickness location (% of chord)	26.5	40	26.7	35	29.5
Max. camber (%)	0	0	0	0	5.4
Max. camber location (% of chord)	-	-	-	-	52.1
Peak $\frac{C_l}{C_d}$ @ $Re = 150000$	48.31	42.96	47.52	45.29	72.66
α of peak $\frac{C_l}{C_d}$ @ $Re = 150000$ (°)	8.5	5.0	7.5	4.5	9
Cruise α @ $Re = 150000$ (°)	9	9	9	9	3

To select an aerofoil, the considered aerofoils were analysed using the XFOIL tool, included in XFLR5 [55]. Analyses in the range of $Re = 50000$ - 1000000 were conducted, with a step size of 25000, to be

later on used in the Plane analysis, and the $Re = 150000$ analysis in particular was considered here, as it approximates the design cruise operating conditions. In Figure 3.6, the C_l and C_l/C_d results for the different aerofoils are presented.

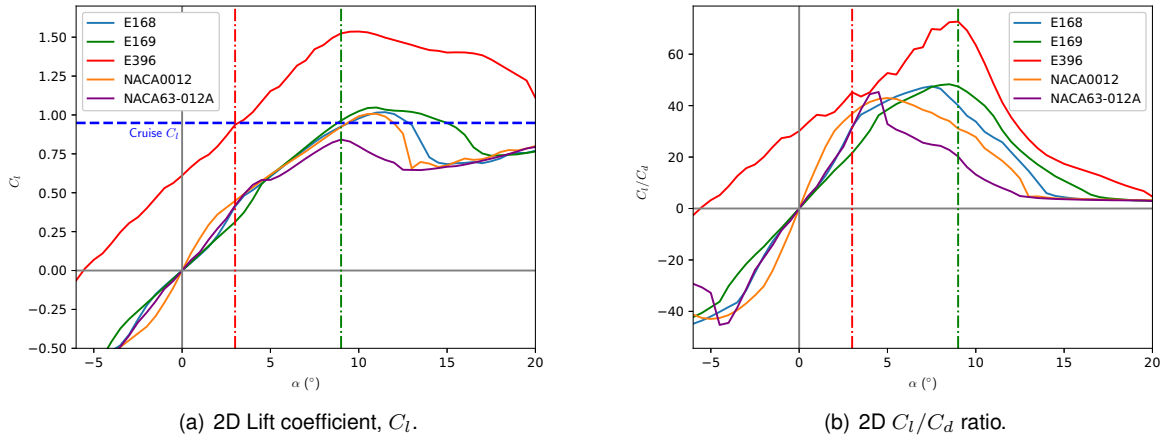


Figure 3.6: Comparison of the considered aerofoils, for $Re = 150000$.

The line in blue indicates the cruise condition C_l previously defined. The green line corresponds to the angle of attack, α , required with the E396 profile to achieve the cruise C_l , while the red line indicates the approximate angle of attack required to achieve the cruise C_l with the E168, E169 and NACA0012. The NACA63-012A cannot achieve the required cruise C_l .

From Figure 3.6, among the symmetrical aerofoils, the E169 presents the highest peak C_l/C_d and has this peak closest to the cruise angle of attack. As such, the E169 was selected from the symmetrical aerofoils. Justifying the reason why a non-symmetrical aerofoil was also considered, the E396 profile boasts a significantly higher peak C_l and C_l/C_d ratio, while the E169 profile operates in cruise condition near its peak C_l , meaning close to its stall angle.

3.2.3 3D wing design

With these two aerofoils selected, a Plane analysis (where the 3D wing is taken into consideration) was conducted using the flow5 software (a more current version of the XFLR5 software) [56]. Both wings are rectangular, such as to maximise the wing area, within the area available with the chosen wheel diameter. The inertia of the vehicle was also defined, such that the CG could be properly calculated. Two types of analyses were run, a constant $V_\infty = 15$ m/s analysis, where the angle of attack α was varied from -20° to 20° , and a constant lift (equal to the weight, in cruise condition) analysis, where the angle of attack was varied in the same range. Only results within α regions where the C_l of the 2D aerofoil could be interpolated were obtained. Figure 3.7 presents the results of these analyses.

During manufacturing, the actual weight of the aircraft exceeded the design MTOW. As such, as more realistic masses were obtained, the Plane analyses were continuously updated. The final configurations analysed were the Full configuration (fully assembled vehicle with a mass of 2383g) and the Tailsitter configuration (vehicle without wheels, mass of 1677g). The mass of the Tailsitter configuration could

be further reduced if the two axes that hold the wheels were removed, but given its slight additional complexity, they were considered here.

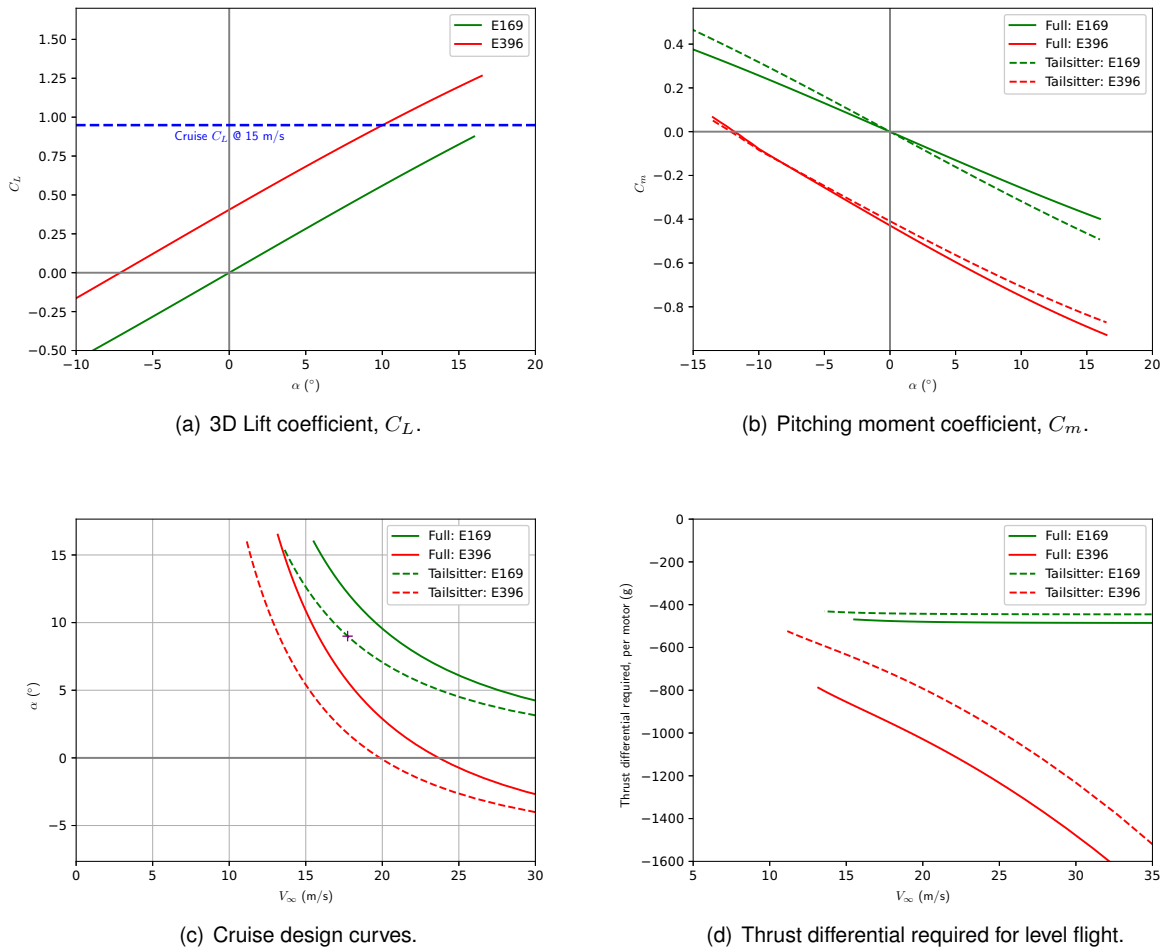


Figure 3.7: 3D Plane analysis.

A clear decrease in the lift coefficient is visible when compared to the 2D lift coefficient, as expected. This is due to the three-dimensional effects that take part, in particular the wing-tip losses caused by the generation of vortices at wing-tips, a known phenomenon of finite wings. In this biplane configuration, this is more relevant as there are four wing-tips, versus the two that would be found in a conventional wing aircraft. Due to this decrease, at the design speed of 15 m/s, the E169 cannot achieve the originally intended cruise C_L .

Compared to the originally intended operating point of $V_\infty = 15$ m/s at 9° angle of attack in the Full configuration, the performance is significantly degraded due to the 3D effects. With the symmetric E169 aerofoil, level cruise flight cannot even be achieved at 15 m/s, at any angle of attack. The non-symmetric E396 aerofoil on the other hand boasts an improvement, by lowering the cruise speed and operating angle of attack, as seen previously in the 2D simulations. As such, when not required, flying without wheels in the tailsitter configuration should bring a great performance improvement, by lowering the weight of the vehicle (and thus the required lift), and the drag the vehicle will face.

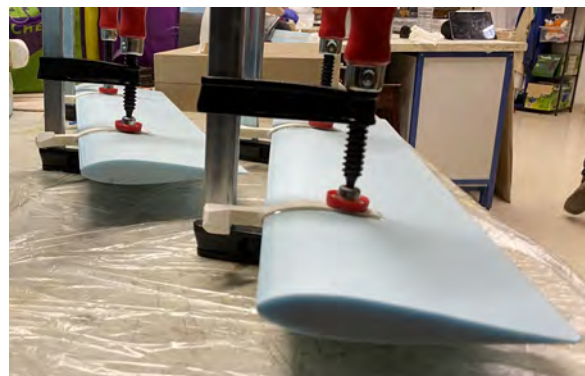
Regarding the longitudinal stability of the UAV, both aerofoils lead to a negative $C_{m\alpha}$ coefficient (the

pitching moment coefficient angle of attack derivative), i.e., a negative slope on the C_m (pitching moment coefficient) curve, meaning the equilibrium point on it will be stable. However, the equilibrium point for the symmetric aerofoil is, intuitively, 0° angle of attack, a point at which the wings will not produce any lift, meaning level flight will not be possible. The E396 profile achieves equilibrium at a negative angle of attack, for which the lift produced is negative, meaning it points downward, thus being a point at which level flight is not possible. As such, given that for both wings at an angle of attack where the aircraft can cruise the pitching moment is not null, the motors should produce a counter-acting differential thrust to maintain the attitude of the aircraft. For example, at the purple operating point in Figure 3.7(c), the differential thrust should produce a 1.39 Nm torque, which given the distance of the motors to the CG, translates into 8.74 N of differential thrust, meaning 4.37 N more on each of the lower motors versus the top motors. The thrust differential required per motor, obtained from C_m , as a function of the airspeed, is also presented for level flight conditions. Note that the CG is located approximately 6 cm in front of the leading edge of the wings, although this value changes slightly depending on the configuration. The pitching moment generated by the cambered aerofoil is considerably higher than that of the symmetrical wing at the same angle of attack.

The selected wings to manufacture use the E169 and E396 aerofoils with a 15 cm chord, and a 56 cm wingspan, amounting to a total 0.168 m^2 wing area. To manufacture the wings, first, the aerofoil is loaded onto the Jedicut software, where the cut layout is drawn and a .gcode file is generated. Then, the .gcode file is loaded onto the GRBL HotWire Mega 5X software, which sends the commands to the hot wire Computer Numerical Control (CNC) machine, where the wings were cut out of extruded polystyrene insulation foam (XPS). The cut profile is then cut to match the desired wingspan, and finally, the previously mentioned attachments are glued, using 10 minute epoxy resin, unlike the 5 minute epoxy resin used in other junctions, as this connection is where the most significant loads are expected. No additional wing structures or structural reinforcements were deemed necessary. The mentioned steps are shown in Figure 3.8.



(a) Hot wire CNC cutting.



(b) Attachment gluing.

Figure 3.8: Wing manufacturing process.

3.3 Propulsive system

The goal of the propulsive system is to generate thrust that lifts the vehicle from the ground in hover mode and propels it forward in forward-flight and ground modes. In addition to that, the differential thrust and torque produced by the four motors are used to generate moments about the three axes of the vehicle, in order to control its attitude in all modes.

For the vehicle in design, an electric propulsion system powered by a battery was chosen for its simplicity, reduced size and weight, given the scale of the UAV in question. An electric propulsive system is composed of 4 main components, a battery, an Electronic Speed Controller (ESC), a motor, and a propeller. Other alternatives could include internal combustion engines or other sources of electric energy, such as hydrogen fuel cells.

When designing the propulsive system, the following requirements and objectives were laid out:

1. A quadcopter layout should be used, meaning four independent rotors should be used;
2. In hovering mode, the vehicle should have a thrust-to-weight ratio of at least 1.5, ideally 2.0;
3. In forward flight mode, the vehicle should produce enough thrust to overcome the drag at its cruising speed, with a minimum 30% margin, such that it is controllable;
4. As much as possible, available hardware should be used;
5. The chosen motors and propellers should fit the F450 frame.

With this in mind, components should be chosen that produce results in accordance with the requirements and objectives. For the design of this system, performance estimates were obtained using the eCalc tool [57], which were continuously updated.

3.3.1 Battery

In an electric propulsion UAV, batteries are used to store energy, by converting chemical energy into electrical energy. Lithium-based batteries currently dominate the market for unmanned aerial vehicles, and in particular Lithium-Ion (Li-Ion) and Lithium-Polymer (LiPo) batteries, due to their increased specific energy and power. LiPos, when compared to Li-Ions present slightly higher specific energies, but much higher discharge rates, and therefore higher specific power [58]. As such, and given their predominance in the small UAV market, LiPo batteries were selected.

A LiPo battery pack can be characterised by the following specifications: Number of cells in series, number of cells in parallel, cell capacity, cell discharge rate, and pack weight [59]. First, given the estimated mass of the UAV of roughly 2300 g, a 4S (4 cells connected in series) battery was determined to be used, considering the expected power required and adequate current draw. Given the characteristics of LiPo cells, such a battery would then have a maximum voltage of 4.2 V per cell, thus 16.8 V total, and a nominal voltage of 3.7 V per cell, thus 14.8 V total. With this characteristic determined, the design of the motor and propeller can go forward, upon which the remainder of the battery characteristics depend, with

a hovering current estimated at 7.15 A per motor, meaning a total current draw of 28.6 A in hover. Thus, in order to achieve a hovering flight time of around 10 minutes, a 4767 mAh capacity battery would be required. Considering the available equipment, two battery packs remain as potential candidates, whose characteristics are presented in Table 3.3.

Table 3.3: Battery characteristics [59, 60].

Manufacturer and Model	Gensace Bashing	Gensace Soaring
		
Configuration	4S1P	4S1P
Nominal Voltage (V)	14.8	14.8
Capacity (mAh)	5000	4000
Energy (Wh)	74	59.2
Discharge Rate (C-rating)	60C	30C
Maximum Discharge Current (A) [C-rating * Capacity]	300	120
Weight (g)	436	376
Specific Energy (Wh/kg) [Energy / Weight]	169.72	157.45
Measured Internal Resistance (mΩ)	13	20 and 15
Estimated Voltage Drop (V) @ 70 A	0.91	1.4 and 1.05

A key aspect to consider, is the voltage drop the battery experiences. A full 4S battery, with no load, will present a voltage of 16.8 V. However when a load is applied, or the battery is not fully charged, a voltage drop is observed, leading to the measured voltage at the terminals of the battery being lower. The voltage at the terminals of a battery can be given by Equation (3.2a), according to the model proposed by [61], where E_0 , K , A and B are model parameters that need to be estimated for a given battery pack, and i^* is the filtered current.

$$U_{\text{batt}} = E_0 - U_{\text{drop}}^{\text{load}} - U_{\text{drop}}^{\text{charge}} \quad (3.2a)$$

$$U_{\text{drop}}^{\text{load}} = R_i i + K \frac{Q}{Q - \int i dt} i^* \quad (3.2b)$$

$$U_{\text{drop}}^{\text{charge}} = K \frac{Q}{Q - \int i dt} \int i dt - A e^{-B \int i dt} \quad (3.2c)$$

The voltage drop due to a load being applied to the battery can then be approximated by $U = R_i * i$, where R_i denotes internal resistance and i stands for current. The ArduPilot [62] firmware estimates the resting voltage of the battery (voltage if no load was applied) using the same approximation, where the internal resistance is estimated by the firmware. Given the fact that the rotational speed of the motor (and consequently the thrust produced by the propeller) is directly dependent on the supplied voltage, a voltage drop translates into a drop in performance, by producing less thrust. Due to this drop in performance, the ArduPilot firmware can scale the controller gains to compensate for the battery voltage decrease [63].

Taking all of this into consideration, the Gensace Bashing battery was chosen, as it presents the

closest capacity to the estimated value required for a 10 minute hovering flight. In addition, it presents higher specific energy, higher maximum discharge, and decreased voltage drop under the maximum expected load, therefore leading to an expected higher autonomy and performance from the UAV. Still, it represents an additional 60 g of mass, and as such, if required, the Gensace Soaring battery can be used as an alternative when flying with maximum payload. As will be seen in Section 3.4, this battery not only powers the propulsive system, but also all avionic systems onboard.

3.3.2 Electronic Speed Controller

Connected to the battery power, there are the four ESCs, one for each of the motors. The ESC receives a Pulse Width Modulation (PWM) signal commanding the throttle for each motor and produces a three-phase AC signal, which rotates the motor. With the use of Metal-Oxide-Semiconductor Field-Effect Transistors (MOSFETs), the DC signal from the battery is converted into a PWM, three-phase signal. This signal presents high-frequency pulses, whose pulse width depends on the commanded throttle. The higher the commanded throttle, the higher the pulse width, and thus the higher the average power [64].

As with any electrical component, ESCs are subject to power losses. These power losses can originate mainly from the rapid switching that occurs in the ESC and from the conduction of electricity. Both [64] and [65] show that, unlike most manufacturers claim, the efficiency of this device is not constant, rather it increases with the commanded throttle value. As such, maximum efficiency of the ESC is observed at full throttle, with this maximum value varying depending on the ESC, in the range of 80% - 95%. This means that in hovering flight, where the thrust produced equals the weight of the UAV and the commanded throttle is below its maximum value, a lower efficiency can potentially be experienced.

When choosing the appropriate ESC for a propulsive system, there are three important characteristics to bear in mind. First, the ESC should support the voltage of the chosen battery, and both of the available ESCs support a 4S battery. Then, the ESC should be able to withstand the maximum expected current to be drawn from the motor. As will be seen in Section 3.3.5, the maximum current expected to be drawn is 18.97 A. Lastly, depending on the architecture of the avionic systems, namely if there are any additional control surfaces powered by servos, an ESC with a Battery Eliminator Circuit (BEC) may be required to supply power to these components. In this system, a BEC is not required on the ESCs. The specifications of the available ESCs are presented in Table 3.4.

As such, the DJI 430 Lite would have been the ideal choice, as it continuously supports the maximum expected current and it is lighter than the alternative. However, as the T-Motor AIR 20A was already installed on the F450 frame, and given that it supports the current expected to be drawn, it was chosen.

3.3.3 Electric motor

To transform the stored electrical energy into mechanical energy by rotating a propeller, a motor is used. Several types of electric motors are available, however, brushless DC motors widely dominate the market for electric UAVs due to their increased efficiency, better torque performance and reduced noise in operation [68]. While a model of a brushless motor is presented in [68], it relies on parameters

Table 3.4: ESC characteristics [66, 67].

Manufacturer and Model	T-Motor AIR 20A	DJI 430 Lite
		
Rated Battery	3S-4S	3S-4S
Maximum Continuous Current (A)	20	30
Maximum Peak Current (A)	30	45
BEC	No	No
Maximum PWM Frequency (Hz)	621	500
Weight (g)	14	11.6

not typically provided by motor manufacturers. Therefore, a model based on specifications provided by manufacturers was developed in [69], where motor losses are assumed to come from two sources: the motor winding resistance and the idle current, which incorporates mechanical losses in the motor.

A motor can be characterised by its speed constant, K_V , the motor internal resistance, R_i , and the idle current, I_0 . Using these parameters, the efficiency of the motor, η_m , its rotational speed, ω , and the power output to the shaft (and hence the power output to the propeller), P_{out} , can be given by Equation 3.3, at a given operating point.

$$\eta_m = \left(1 - \frac{i_{in} R_i}{U_{in}}\right) \left(1 - \frac{I_0}{i_{in}}\right) \quad (3.3a)$$

$$\omega = K_V (U_{in} - i_{in} R_i) \quad (3.3b)$$

$$P_{out} = (i_{in} - I_0)(U_{in} - i_{in} R_i) \quad (3.3c)$$

This yields an efficiency curve where the most efficient point is not trivial, but some general conclusions can be drawn. Motor efficiency typically increases significantly in lower rotational speed ranges, up until its peak efficiency. After that point, efficiency slowly decreases until the full throttle point is reached.

When choosing an appropriate motor, the motor-propeller combination must be taken into consideration as a whole. Regarding the motor, the following should be taken into account:

- The speed constant, K_V , is a rough indication of how fast the motor will rotate, along with the system's input voltage. With the same propeller, a higher K_V motor produces higher static thrust;
- Given a propeller (i.e. the motor's load), the power limit of the motor should be sufficient for the propeller to rotate at full throttle;
- The motor shaft should be compatible with the chosen propeller and the motor mount should be compatible with the frame it is being mounted on.

Table 3.5: Motor characteristics [66, 67, 70].

Manufacturer and Model	DJI 2312E 960KV	T-Motor Air 2213/KV920	T-Motor AT2814 KV1050
			
K_V (rpm/V)	960	920	1050
Rated Battery	3S-4S	3S-4S	3S-4S
Maximum Power (W)	280	230	700
Idle Current @ 10 V (A)	0.45	0.5	1.5
Magnetic Poles	14	12	14
Internal Resistance (m Ω)	117	132	35
Shaft Diameter (mm)	8.0	6.0	6.0
Weight (g)	60	54	107

In Table 3.5, the specifications of the available motors are presented. The choice of the motor-propeller combination will be detailed in Section 3.3.5. Still, the chosen motor was the DJI 2312E 960KV. Given the previously mentioned model on motor efficiency, presenting a lower idle current and internal resistance than the T-Motor Air 2213/KV920, it should operate more efficiently. In addition, it is compatible with the F450 motor mounts. Lastly, the T-Motor AT2814 KV1050 presents too significant of a power upgrade, which comes at the cost of increased weight and thus energy consumption.

3.3.4 Propeller

In order to generate thrust, a propeller is rotated, such that it experiences a velocity, and thus produces a lift force. A typical propeller will have a given number of blades, with each blade being an aerofoil, that will experience a forward velocity and thus generate lift. In general, the thrust, torque and mechanical power produced by a propeller can be given as a function of the coefficients of thrust C_T , torque C_τ and power C_P , according to Equation (3.4), where n_{rps} is the rotational speed of the propeller in rotations per second, D_{prop} is the diameter of the propeller, and ρ is the density of the air [71].

$$T = \rho n_{rps}^2 D^4 C_T \quad (3.4a)$$

$$\tau = \rho n_{rps}^2 D^5 C_\tau \quad (3.4b)$$

$$P = \rho n_{rps}^3 D^5 C_P \quad (3.4c)$$

Using a model, such as the one provided by the Blade Element Momentum Theory (BEMT), these coefficients can be obtained for a given propeller, as a function of the advance ratio, J . With experimental tests, these coefficients can also be obtained. The advance ratio provides a ratio between the velocities

of the flow impacting the propeller and the velocity of the propeller's rotation and is defined as

$$J = \frac{V_\infty}{n_{rps} D_{prop}}. \quad (3.5a)$$

The efficiency of the propeller in forward flight follows as

$$\eta_{prop} = J \frac{C_T}{C_P}. \quad (3.5b)$$

For hovering flight, where the advance ratio is not applicable, the figure of merit follows as [72]

$$M = \frac{C_T^{3/2} / \sqrt{2}}{C_P}. \quad (3.5c)$$

Using BEMT requires a complete definition of the propeller geometry, including the aerofoil geometry at each section of a blade, and its pitch angle and chord. The propeller manufacturer APC publishes such data on their website [73].

From BEMT, assuming axial free stream flow, the thrust and power can be obtained from Equation 3.6 [74],

$$T = \frac{B}{4\pi} \rho \int_{R_h}^{R_p} c V_R^2 (C_l \cos \phi_R - C_d \sin \phi_R) dr \quad (3.6a)$$

$$P = 2\pi n \tau \quad (3.6b)$$

$$P = -\frac{B}{2} n \rho \int_{R_h}^{R_p} c V_R^2 (C_l \sin \phi_R + C_d \cos \phi_R) dr \quad (3.6c)$$

$$V_R = \sqrt{(V_\infty + V_{ia})^2 + (2\pi n r)^2} \quad (3.6d)$$

$$\phi_R = \arctan \frac{V_\infty + V_{ia}}{2\pi n r} \quad (3.6e)$$

$$C_l = C_{l\alpha} \alpha_{\text{eff}} \text{ (unstalled)}, \quad \alpha_{\text{eff}} = \theta - \alpha_0 - \phi_R \quad (3.6f)$$

where B is the number of blades of the propeller, R_h and R_p are the radius of the hub and of the propeller blade, respectively, c is the chord length of a given blade element, C_l and C_d are the 2D lift and drag coefficients of the aerofoil of a given blade element, V_{ia} is the induced velocity caused by the rotation of the propeller, ϕ_R is the angle of the incident resultant airflow, V_R , α_{eff} is the effective angle of attack on the blade element, θ and α_0 are the blade element pitch angle and zero-lift angle of attack, respectively. In Figure 3.9, the previously mentioned angles are depicted. It is worth mentioning that α_0 is negative for a positive camber aerofoil.

Usually, manufacturers present propeller dimensions as $D_{prop} \times p_{prop}$, in inches. Most common UAV propellers use a variable pitch angle and chord along the blade radius. Therefore, the pitch of such propellers is defined in inches, as the forward distance covered in one full rotation of the propeller, if it was rotating through a solid medium [75]. According to [71], for a given rotational speed n_{rps} and the free stream velocity at which the propeller will stop producing thrust (also called pitch speed), V_∞^{pitch} the pitch

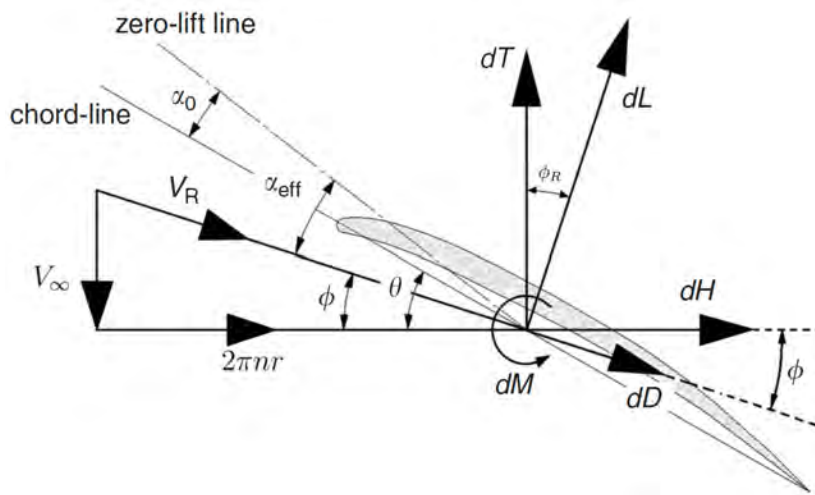


Figure 3.9: Cross-section view of a propeller blade element (adapted from [74]).

reported by the manufacturer follows as $p_{prop} = V_{\infty}^{pitch} / n_{rps}$. Although not directly linked, a propeller with a higher pitch described by the manufacturer will present a higher pitch angle, θ , throughout its length.

From Equation (3.6a), it is clear that an increase in the diameter of the propeller will result in an increase in thrust, both in static conditions (where $V_{\infty} = 0$) and dynamic conditions. Increasing the pitch of the propeller will increase the angle of attack, α_{eff} of the propeller, and thus, will increase the local C_l of each blade element, and consequently the thrust, so long as the increase does not push the propeller into a stalled region.

As the free stream velocity increases, maintaining the same rotating velocity, the angle of the resultant airflow will increase, thus α_{eff} will decrease. As such, with an increase in free stream velocity, a decrease in C_l is experienced, thus a decrease in thrust produced, despite the slight increase in the resultant velocity. At a given velocity, α_{eff} will become zero and no thrust will be produced. By increasing pitch, the effective angle of attack is increased, so, the velocity at which the propeller stops producing thrust also increases, in agreement with the previous definition of pitch (in inches). Moreover, increasing the pitch increases the free stream velocity at which maximum propeller efficiency occurs. These effects can be seen in Figure 3.10, where propellers with different pitch values were evaluated using BEMT and experimental tests, at a fixed rotational speed.

In hover, according to [72], the use of negative twist (i.e. a higher pitch near the root of the blade than at the tip of the blade) can improve the figure of merit M . In [76], it was shown that the figure of merit increases with the pitch angle, up to a given maximum point, after which the figure of merit decreases, hence, for a given hover condition, there is an optimum blade pitch angle. As such, variable pitch mechanisms can enable more efficient operation throughout different operating conditions, although at the cost of increased complexity.

From Equation (3.6a), one might assume that increasing the blade number will allow an increase in thrust, with no down-sides, however, when taking into account correction factors to BEMT, increasing the blade number increases tip-losses [71].

Table 3.6 presents the different characteristics of the considered propellers. Although 9x6E is the only

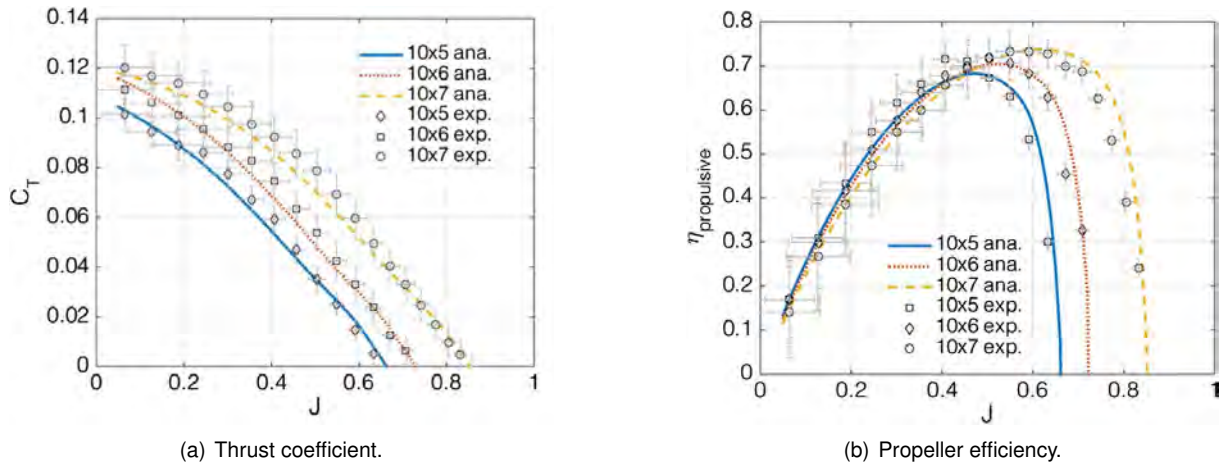


Figure 3.10: Comparison of different propeller pitch values with advance ratio [71].

APC propeller presented, the full range of APC Electric propellers was considered during the design [73].

Table 3.6: Propeller characteristics [66, 67, 73].

Manufacturer and Model	DJI Z-Blade 9450	T-Motor T9545	APC Thin Electric 9x6E
			
Diameter (in)	9.4	9.5	9
Pitch (in)	5.0	4.5	6.0
Hub Diameter (mm)	15.8	16.0	20.32
Shaft Diameter (mm)	-	-	6.35
CW and CCW	Yes	Yes	Yes
Weight (g)	13	13.5	17.86

As detailed in Section 3.3.5, the APC 9x6E propeller was chosen. Compared to the other two alternatives, which screw directly onto the motor shaft, the APC 9x6E propeller has a geometry optimised for forward flight rather than hovering, with a noticeably higher twist.

Given that this propeller does not directly screw onto the motor shaft, it would need to be adapted to be mounted onto the chosen motor. First, the shaft hole was enlarged to 8 mm in diameter. Secondly, due to the short shaft the motor presented and the thick hub of the propeller, a larger 12 mm hole had to be drilled through the top of the hub, such that enough thread on the shaft was available to screw a nut onto. A washer with 8 mm internal diameter and 12 mm outer diameter was then placed on each propeller.

Lastly, given that two of the motors spin in a clockwise (CW) orientation and the two others in a counter-clockwise (CCW) orientation, two sets of different propellers were used, the 9x6E and 9x6EP (pusher version). For CCW spinning motors, right-locking nyloc nuts were used to tighten the propeller, and for the CW spinning motors, left-locking nyloc nuts were used. As such, the motors spin in the direction that tightens the nuts, rather than undoing them. Nyloc nuts and washers were used such that the fitting is more secure and the vibrations are reduced.

As the propeller was modified from its original configuration, imperfections in drilling the holes could

lead to an unbalancing of the propeller and consequent generation of vibrations. Therefore to validate the changes, the propellers were tested on a thrust stand (to be described further in Section 5.1.1), in order to confirm vibration levels were acceptable.

In Figure 3.11, the vibrations measured at each motor speed are presented, across different test methods, performed in static conditions. At some rotational speeds, peaks in vibration are observed (corresponding to harmonics of the natural frequency), but, even at the motor's maximum operating speed, these values are smaller than the ones observed on the same motor with its original self-tightening propeller.

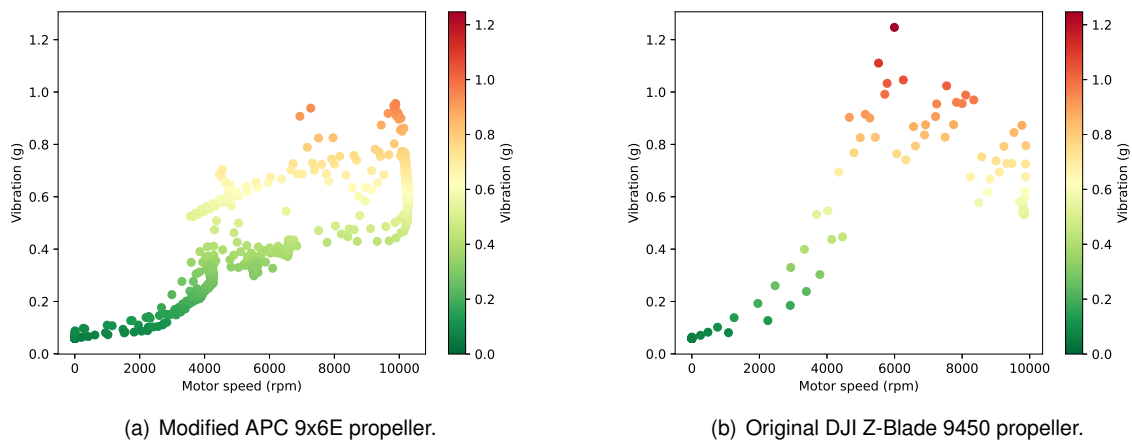


Figure 3.11: Vibrations during static tests.

3.3.5 Performance simulation

To choose the appropriate motor and propeller combination, previously mentioned in Sections 3.3.3 and 3.3.4, simulations were performed with the objective of estimating the performance of such combinations in real flight conditions, both in hover and forward flight. The popular web-based tool eCalc [57] was used, in particular its calculators xCopterCalc and propCalc.

In both calculators, some settings were assumed that are unrelated to the design choice in assessment. These include a 100 m airfield altitude, 25°C temperature, and a QNH (or sea-level pressure) of 1013 hPa. The Gensace Bashing battery was considered, and entered as a 5000 mAh LiPo battery, with 45C continuous discharge rating and 60C maximum discharge, in a normal charge state, and with 85 % of its capacity used during flight. For all configurations except with the T-Motor AT2814 motor, the AIR 20A ESC was considered, as a max 20A ESC in eCalc. With the AT2814 motor, the DJI ESC was considered, as a max 30A ESC in eCalc, with a 45 A maximum current rating. Motor cooling was always considered as good, given their appropriate exposure to airflow. During the design phase, given that different propellers and motors present different weights, only the Full vehicle configuration was considered, with an estimated mass of 2400 g. The actual masses of the configurations were used after the design was finalised. In all configurations, the wheel axle mass was considered. In the case of the configuration with the AT2814 an additional 188 g mass was considered. Only possible combinations

were evaluated, meaning, only combinations where the propeller can be mounted on a given motor.

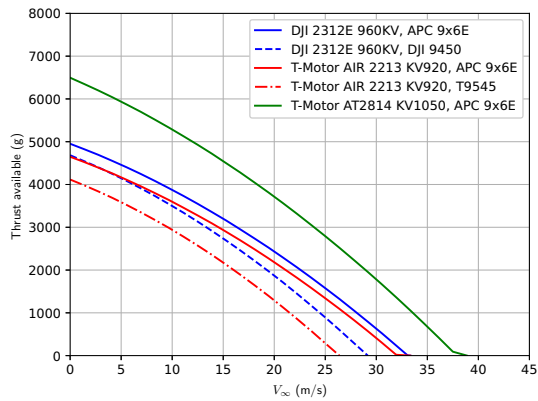
It is worth mentioning that the methods used by the eCalc tool, to the best of our knowledge, are unknown. Still, it is likely that ESC efficiency is disregarded, and that models similar to those presented in Sections 3.3.1 and 3.3.3 are used for the battery and motor. The propeller however is likely not simulated using a model like BEMT, given the parameters provided to the tool.

Table 3.7: eCalc xCopterCalc analysis results for hovering condition.

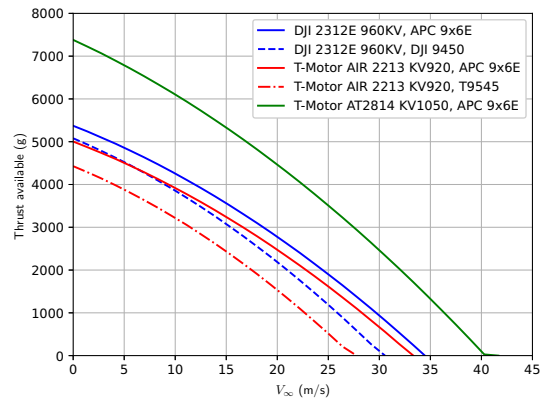
Motor Propeller	DJI 2312E		T-Motor AIR 2213		T-Motor AT2814
	APC 9x6E	DJI 9450	APC 9x6E	T9545	APC 9x6E
T/W ratio [Full]	1.7	1.8	1.6	1.6	2.1
T/W ratio [Ground]	1.8	1.9	1.7	1.7	2.2
T/W ratio [Tailsitter]	2.5	2.6	2.3	2.3	2.9
T/W ratio [Quadcopter]	2.7	2.8	2.5	2.5	3.1
Hover electrical power (W) [Full]	111.3	108.6	112.9	113.9	120.7
Hover electrical power (W) [Quadcopter]	56.8	55.4	57.7	58.2	67.7
Hover motor efficiency (%) [Full]	80.5	80.5	79.3	79.4	85.1
Hover motor efficiency (%) [Quadcopter]	82.0	82.0	80.6	80.6	83.5
Hover flight time (min) [Full]	8.2	8.4	8.1	8.0	7.6
Hover flight time (min) [Ground]	9.1	9.3	8.9	8.9	8.2
Hover flight time (min) [Tailsitter]	14.5	14.9	14.3	14.1	12.3
Hover flight time (min) [Quadcopter]	16.4	16.8	16.1	16.0	13.7
Maximum electrical power (W)	259.9	261.4	235.3	234.2	385.0
Maximum current (A)	18.97	19.09	17.04	16.95	29.25
Estimated motor temperature (°C)	51	51	46	45	46

The results obtained for hovering flight are presented in Table 3.7. Configurations using the T-Motor AIR 2213 motor clearly underperform when compared to the two other motors, both producing a lower maximum thrust (and hence a lower thrust-weight ratio) and being less efficient in hover by consuming more power, thus presenting a lower flight time. This is likely due to the DJI motor's higher KV's and lower idle current. Compared to the AT2814 motor, however, the DJI motor underperforms, with the AT2814 motor achieving a much higher thrust-weight ratio, despite being 188 g heavier. However, in hover, this increase in weight means the hover operating point with the AT2814 motor requires more power, despite its increased efficiency. Together with the reasons mentioned next in the forward-flight analysis, the DJI 2312E motor was chosen. From the two available configurations, the DJI propeller achieves a slightly lower hover power consumption and a slightly higher thrust-to-weight ratio. As such, it would be the most appropriate choice for hovering flight, however, as will be seen next, the APC 9x6E propeller is better suited for forward flight, and hence it was the chosen propeller.

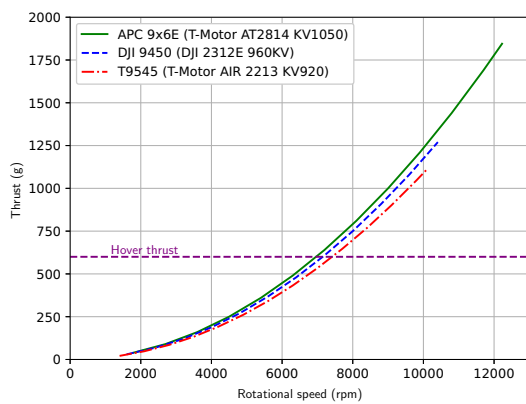
The results from the forward flight eCalc analysis are presented in Figure 3.12. First, as a validation of the battery chosen in Section 3.3.1, the total available thrust as a function of the free stream velocity is presented for configurations using both batteries. It is clear that with the Gensace Bashing battery, the total thrust produced is higher, due to this battery's higher discharge capacity, and therefore lower voltage drop while in load. The DJI and T-Motor propellers underperform compared to the APC propeller,



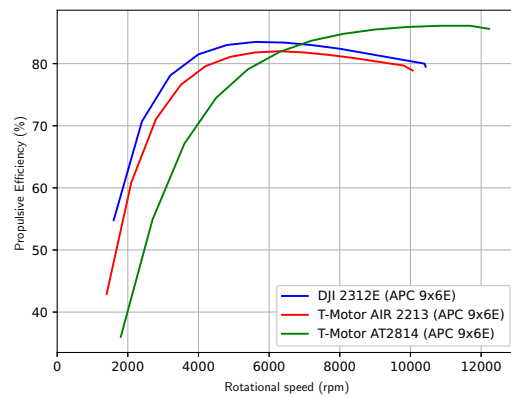
(a) Available thrust with the Gensace Soaring battery.



(b) Available thrust with the Gensace Bashing battery.



(c) Static thrust produced by each propeller.



(d) Static efficiency comparison of each motor.

Figure 3.12: eCalc propCalc analysis results for forward flight condition.

due to the APC's higher pitch. In addition, the APC propeller features a geometry designed for forward-flight, unlike the DJI and T-Motor propellers, which were designed for hover conditions, so they might perform worse than predicted by this tool, which was made for forward-flight conditions. Given the conclusion reached in Section 3.2.3 that the aircraft would have to fly faster than its intended design speed, performance at higher speeds is critical for the success of the forward-flight mode. The AT2814 motor could have been a better choice for forward-flight conditions, producing more thrust, however, given the constraints mentioned in Section 3.2.1, increasing the weight would increase the wing loading, forcing the vehicle to fly at an even higher speed, which would increase the drag of the UAV, thus not being chosen.

Lastly, the thrust and motor efficiency as a function of the motor rotational speed are presented. The thrust results are only presented once for each propeller (as they are always the same), for the highest KV motor supported by that propeller. Similarly, the efficiency results are only presented once for each motor, only considering the APC propeller. From these results, it is clear that below the hovering conditions the DJI motor is the most efficient, however, above the hovering condition, the AT2814 proves to be more efficient, on its own. These results also corroborate the evolution described in Section 3.3.3. As such, the final combination that was implemented in the UAV was the DJI 2312E motor, with the APC 9x6E

propeller.

3.4 Avionic systems

3.4.1 System components

To accomplish the multimodality objectives, avionic systems are required to control the vehicle. The vehicle requires at least one pilot to be flown, even in automatic modes, where the pilot acts as a safety layer, monitoring the execution of the flight and taking over control if required. A Radio Control (RC) system serves as the primary link between the pilot and the Unmanned Aerial System (UAS). For this system, the FrSky Taranis X9D Plus 2019 was used as the remote controller [77] and a FrSky RX6R receiver [78] was fitted in the UAV. The remote and receiver communicate using a frequency of 2.4 GHz.

To control the outputs sent to the motors and log information about the flight, a CubePilot CubeOrange flight controller was used, with an ADSB-IN carrier board. It features two different processors, the FMU, using an STM32H753 processor, with 2 MB of flash memory, 1 MB of RAM memory and running at up to 480 MHz, and the IO, using an STM32F103. The FMU features 6 PWM outputs and runs the flight code. The IO processor features 8 PWM outputs and can be used as a failsafe processor, in the event of an FMU failure. The RC inputs are connected to the IO processor and the interfaces the CubeOrange presents connect to the FMU, which can be used to connect additional hardware, through the base board. In terms of sensors, three different Inertial Measurement Units (IMUs) are present, an ICM20649, an ICM20602, and an ICM20948, with the latter two being vibration-dampened. In addition, two MS5611 barometers are used. Additional details can be found in [79]. The ADS-B carrier board features a uAvionix ADS-B IN receiver and a built-in antenna, which can be used to detect other aircraft in the surrounding airspace of the vehicle [80].

To provide power to the autopilot and monitor the battery and power consumption, the Power Brick Mini Power module by CubePilot had originally been chosen, as it was supplied with the CubeOrange. However, comparing its readings with those of a UNI-T UT203R clamp current meter [81] at the battery output, a dead zone and offset were verified in the range of 0-5A, where the ground mode is expected to operate. Given this fact, such that viable power draw readings could be obtained, a different analogue Power Module was used instead. It can be used with up to an 8S battery and can sense a maximum current of 90 A. The battery connects to it on one end, and the other end connects to the distribution board that connects to the ESCs. It connects to the POWER1 port on the autopilot.

For navigation, the Here+V2 GNSS module is used, which features a u-blox NEO-M8P-0, capable of using GPS, GLONASS and BeiDou constellation satellites. Additionally, the Here+ base station mounted on a tripod enables RTK functionality for centimetre-level accuracy measurements [82].

To measure the airspeed in forward flight, an airspeed sensor and pitot tube are used with a 4525DO digital sensor, which connects via I²C to the autopilot.

To provide a live telemetry feed to a ground station, a telemetry radio is used, in particular, a Holybro Sik Telemetry Radio, functioning at 433 MHz. It supports the MAVLink protocol, which will be used to

both send and receive data from the ground station, running the Mission Planner software [83].

The avionic system components described are illustrated in Figure 3.13. In Figure 3.14, a diagram presenting the previously mentioned components and their respective connections is shown. Green lines indicate bus connections and red and white connections indicate power delivery. Bus connections indicate next to the connection the protocol used and, inside square brackets, the port to which they connect.

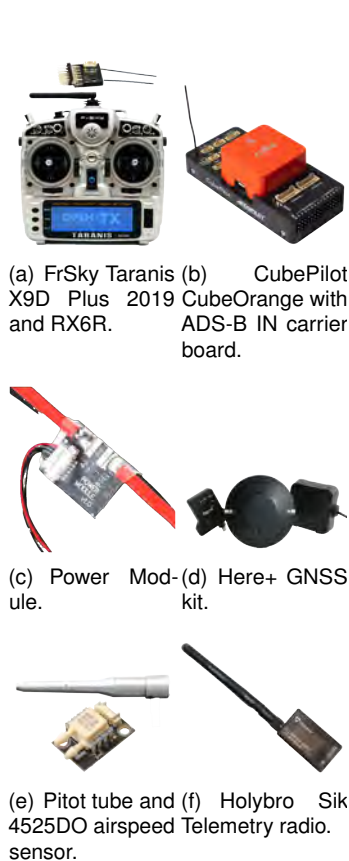


Figure 3.13: Avionic system components.

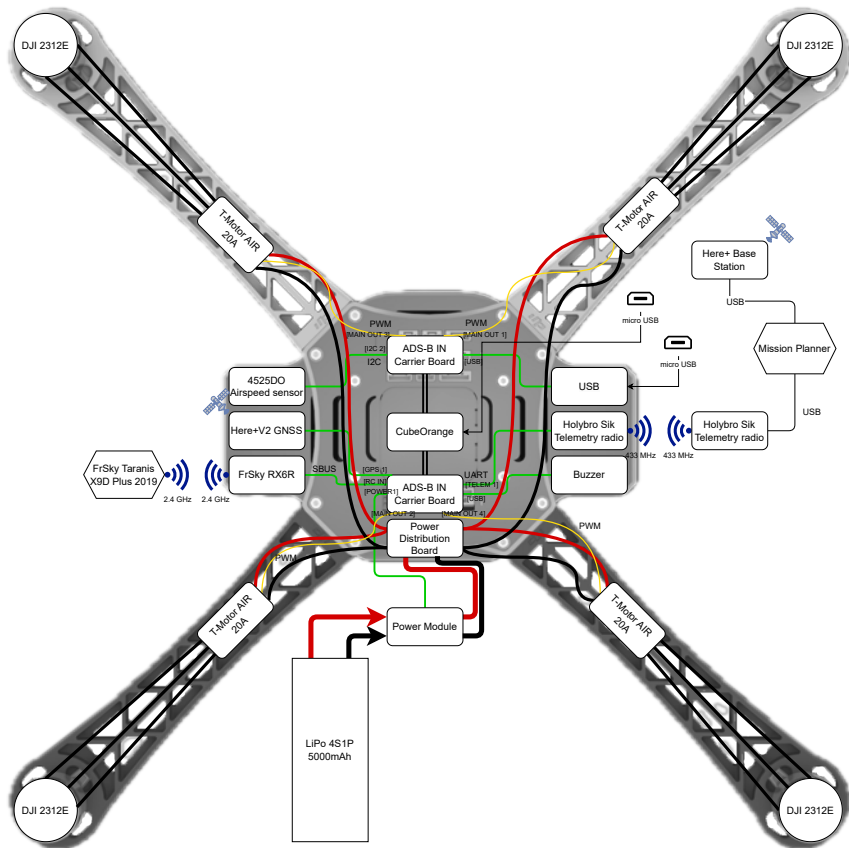


Figure 3.14: Avionics schematic.

3.4.2 Autopilot firmware

Given the need to implement control techniques for such a novel configuration, the flight control firmware either had to be developed from the ground up, or implemented on top of existing open-source firmware. For the vehicle in question, the CubeOrange autopilot was chosen (similar to Pixhawk boards), so the firmware must be compatible with it. Pixhawk is a set of open-source standards providing "hardware specifications and guidelines for drone systems development", developed by the Dronecode Foundation [84]. Taking those constraints into account, two main flight control firmware options are available, PX4 and ArduPilot. The aim of both is to perform the tasks of the autopilot software, which is achieved by implementing different control modes and features.

PX4

PX4 [85] is an autopilot flight stack, supported by the Dronecode Foundation. It supports different airframes, such as Multicopter, Planes, VTOL aircraft, and additionally, but only experimentally, Airships, Autogyros, Balloons, Helicopter, Rovers and Submarines. Of particular interest to the present work, it supports conventional VTOL aircraft, Tailsitters, and Tiltrotors. The Tailsitters supported by PX4 can either require aerodynamic surfaces or be fully dependent on the rotors, as the configuration presented in this work.

From the pilot's point of view, PX4 implements control modes that are very similar to those of ArduPilot, covered in more depth later. As for the Ground Control Station (GCS) software used with PX4, although it is technically compatible with any MAVLink compatible software, the best experience can be obtained by using QGroundControl.

For developers, PX4 uses a single codebase for all different types of vehicles it supports. This codebase is then split into different modules, each responsible for a given task, which work together, inter-changing information using uORB, a messaging API. Lastly, the PX4 code is written in the C++ programming language.

ArduPilot

ArduPilot [62] is an autopilot system originally created by Jordi Munoz, and currently maintained by the ArduPilot Dev Team. It supports the same types of vehicles as PX4, while dividing them into Copters, Planes, Rovers, Subs and Blimps. VTOL aircraft are implemented within the Plane category, as so-called QuadPlanes. QuadPlanes are then divided into tiltrotor aircraft and non-tiltrotor aircraft. The non-tiltrotor aircraft are then categorized according to the number of motors as multicopters or single/dual motors. The multicopter type QuadPlanes can either be Planes (meaning Lift+Cruise VTOL aircraft), or tailsitters. ArduPilot supports the usage of tailsitters with vectored thrust and non-vectored thrust, as well as tailsitters with and without aerodynamic control surfaces.

From the pilot's point of view, ArduPilot implements several different control modes, both for fixed-wing mode and quadcopter mode, which are covered in Section 4.3. ArduPilot, like PX4, also uses the MAVLink protocol, but the best experience can be obtained with the MissionPlanner GCS software.

For development purposes, each vehicle type is implemented using a different version of the ArduPilot firmware, for example, the Plane firmware is implemented in ArduPlane. Each of these versions is a specific implementation which relies on a common set of libraries, shared by all vehicle types. In a general fashion, the code can be split into three different parts, the Hardware Abstraction Layer, which is specific to each board type, the Shared Libraries, where sensors, controllers and estimators are implemented, and lastly, the Vehicle Code, where code specific to each vehicle type is implemented, using the aforementioned libraries. Like PX4, ArduPilot is also written in C++.

In conclusion, PX4 and ArduPilot are similar in the features that they offer. Based on user feedback, the author's experience, and existing documentation, ArduPilot was chosen for its reliability and ease of feature implementation.

Chapter 4

Controller implementation

This chapter provides a description of the implemented control algorithms used to manually control the vehicle and give it automatic capabilities. As ArduPilot was the firmware chosen in Section 3.4.2, this chapter describes the implementation of the existing ArduPlane code, its relevant features, and the modified code to implement ground locomotion on the vehicle. All of the final modified firmware code is available in a GitHub repository at <https://github.com/afonsoVale/ardupilot/tree/QuadPlaneRover-4.4>.

4.1 Vehicle dynamics

The vehicle dynamics and the notation used are presented with the goal of defining the control laws applied. Because the UAV's orientation changes drastically in forward flight, a different notation will be used for hover (and ground) modes and for forward flight modes, such that it is in agreement with commonly used notation for quadcopters and for fixed-wing aircraft. The following will be considered:

Inertial Frame $\{I\} = \{N, E, D\}$

Vehicle Frame $\{V\} = \{X, Y, Z\}$

Body Frame $\{B\} = \{x_b, y_b, z_b\}$

Position in Inertial Frame $\mathbf{P} = (n, e, d)$

Linear Velocity in Inertial Frame

$$\mathbf{V}_I = (v_n, v_e, v_d)$$

Linear Velocity in Body Frame

$$\mathbf{V}_B = (v_x, v_y, v_z)$$

Body Frame rotation w.r.t. Inertial Frame

$$\Phi = (\phi, \theta, \psi)$$

Angular velocity in Body Frame

$$\omega = (p, q, r)$$

Total Force $\mathbf{F} = (F_x, F_y, F_z)$

Total Torque $\tau = (\tau_\phi, \tau_\theta, \tau_\psi)$

Thrust produced by the i^{th} motor T_i

Torque produced by the i^{th} motor τ_i

Lift and Drag produced by the j^{th} wing

$$(L_j, D_j)$$

Weight force in inertial frame

$$W = (0, 0, mg)$$

Inertia tensor in Body Frame

$$I = \text{diag}(I_x, I_y, I_z)$$

Distance from rotors/wing to CG

$$d_{rotors/ca}$$

In general, the equations of motion can be written as

$$\dot{P} = V_I, \quad (4.1a)$$

$$m\dot{V}_I = W + R_B^I F, \quad (4.1b)$$

$$\dot{\Phi} = Q(\Phi)\omega, \quad (4.1c)$$

$$I\dot{\omega} = \tau - \omega \times I\omega, \quad (4.1d)$$

where R_B^I represents the rotation matrix from the body frame to the inertial frame done in a roll-pitch-yaw order, meaning, $R_B^I = R_z(\psi)R_y(\theta)R_x(\phi)$. $Q(\Phi)$ does not represent a rotation, but rather the relation between the angular velocities and the Euler angle derivatives.

To maintain uniformity, a similar notation to that used in ArduPilot is adopted. The inertial frame is considered to be centred at the home point (corresponding to the point where the vehicle is armed), with the axes pointing North, East and Down (towards the centre of the Earth). Similarly, the vehicle frame has the same orientation as the inertial frame but is centred at the vehicle's CG. In all the configurations, the vehicle maintains two planes of symmetry, and as such all products of inertia are approximately null, and the inertia tensor is diagonal. Lastly, s_a , c_a and t_a will be used as an abbreviation for $\sin a$, $\cos a$ and $\tan a$ respectively, with a being a given angle.

4.1.1 Hover dynamics

Both the hover and ground modes use the same notation. The body frame is defined as being centred in the CG, with the x_b axis pointing in the forward direction of the vehicle, the y_b axis pointing to the right-hand side of the drone (and therefore aligned with the wheel rotation axis), and z_b points downwards. This reference frame rotates as the attitude of the UAV changes. Figures 4.1 and 4.2 illustrate the previously described coordinate frames and corresponding notation.

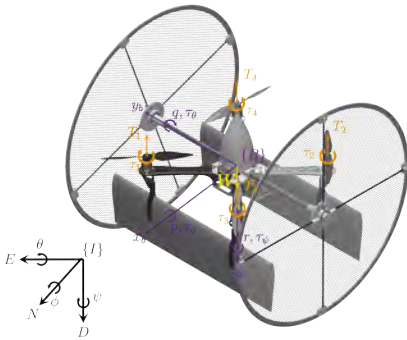


Figure 4.1: UAV model in hover mode.

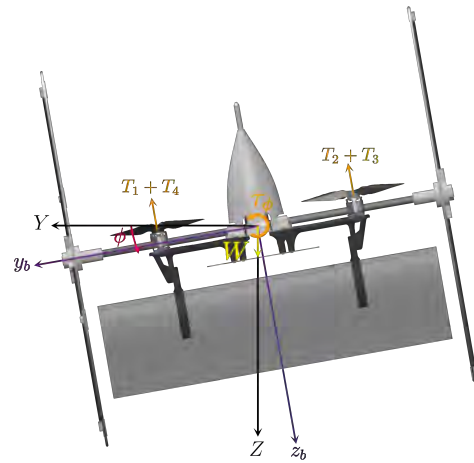


Figure 4.2: Roll manoeuvre in hover mode.

The robots' dynamics in this mode closely resemble those of a regular quadcopter apart from a

modified inertia, and increased aerodynamic footprint. As such, models for a quadcopter amply explored in [86–88] were used as a base for the model that will be described. Commonly, simple quadrotor models neglect aerodynamic forces acting on the aircraft, however, the presence of wings and large wheels results in aerodynamic forces which are not neglectable.

In order to maintain simplicity, aerodynamic drag was considered with two effects, a horizontal (with respect to the inertial frame) drag force and a pitching moment due to the drag of the wings acting below the CG. The horizontal drag force is considered to be the result of the drag generated in the x_b direction, which is mainly due to the wings and wheels, and the drag generated in the y_b direction, largely due to the area of the wheels. These effects are modelled in Equations (4.2b), (4.2c) and (4.3e). In reality, these forces are dependent on airspeed, however, due to the inability to measure airspeed in hover modes, the body frame velocities were considered. Additionally, the drag coefficients $C_{D_x}^{hover}$, $C_{D_y}^{hover}$ and $C_{D_{wings}}^{hover}$ are in fact dependent on the attitude of the vehicle with respect to the airflow, but given the fact that in hover the aircraft moves at small pitch angles, a constant value for the drag coefficient is assumed, in hovering conditions. Having said so, applying the equations of motion to the hover mode, yields, for each state variable, the following:

$$\dot{n} = v_n, \dot{e} = v_e, \dot{d} = v_d \quad (4.2a)$$

$$\begin{aligned} \dot{v}_n = & -\frac{T}{m}(c_\phi s_\theta c_\psi + s_\phi s_\psi) \\ & -\frac{1}{2m}\rho S(\text{sgn}(v_x)C_{D_x}^{hover}v_x^2c_\psi \\ & + \text{sgn}(v_y)C_{D_y}^{hover}v_y^2s_\psi) \end{aligned} \quad (4.2b)$$

$$\begin{aligned} \dot{v}_e = & -\frac{T}{m}(c_\phi s_\theta s_\psi - s_\phi c_\psi) \\ & -\frac{1}{2m}\rho S(\text{sgn}(v_x)C_{D_x}^{hover}v_x^2s_\psi \\ & + \text{sgn}(v_y)C_{D_y}^{hover}v_y^2c_\psi) \end{aligned} \quad (4.2c)$$

$$\dot{v}_d = -\frac{T}{m}c_\phi c_\theta + g \quad (4.2d)$$

$$\dot{\phi} = p + qs_\phi t_\theta + rc_\phi t_\theta \quad (4.3a)$$

$$\dot{\theta} = qc_\phi - rs_\phi \quad (4.3b)$$

$$\dot{\psi} = q\frac{s_\phi}{c_\theta} + r\frac{c_\phi}{c_\theta} \quad (4.3c)$$

$$\dot{p} = qr\frac{I_y - I_z}{I_x} + \tau_\phi\frac{1}{I_x} \quad (4.3d)$$

$$\begin{aligned} \dot{q} = & pr\frac{I_z - I_x}{I_y} + \tau_\theta\frac{1}{I_y} \\ & -\frac{d_{ca}}{2I_y}\text{sgn}(v_x)C_{D_{wings}}^{hover}\rho Sv_x^2 \end{aligned} \quad (4.3e)$$

$$\dot{r} = pq\frac{I_x - I_y}{I_z} + \tau_\psi\frac{1}{I_z}. \quad (4.3f)$$

The actuation torques, produced by the differential thrust and torque of the rotors, are obtained from Equation (4.4).

$$\tau_\phi = \frac{d_{rotors}}{2\sqrt{2}}[(T_2 + T_3) - (T_1 + T_4)] \quad (4.4a)$$

$$\tau_\theta = \frac{d_{rotors}}{2\sqrt{2}}[(T_1 + T_3) - (T_2 + T_4)] \quad (4.4b)$$

$$\tau_\psi = (\tau_1 + \tau_2) - (\tau_3 + \tau_4) \quad (4.4c)$$

In hover, the vehicle's pitch and roll angles are controlled using differential thrust, while the vehicle's

yaw angle is manipulated using differential torque. To move, the vehicle relies on adjusting the pitch/roll angle to point the thrust vector towards the desired direction of movement.

The pitching moment caused by wing drag acts by causing a pitch-down moment when v_x is positive. Compared to the base quadcopter frame, the addition of wheels besides contributing to the aerodynamic drag forces, increases the vehicle's moment of inertia, mainly I_x and I_z . Because the wheel freely rotates around a bearing, the pitch dynamics are largely unaffected by the presence of the wheels, as in this case, the vehicle does not act as a rigid body. Because the equations are written for a rigid body, the moment of inertia I_y can artificially be considered to be unchanged in the presence of the wheels, assuming there is no friction on the bearing. The addition of wings on the other hand, mainly contributes to the aerodynamic forces, as their mass is relatively low, still, the moment of inertia I_y will increase slightly. The previously described model considers the vehicle as a rigid body and neglects any gyroscopic torques produced either by the propellers and motors rotating, or the wheels rotating.

4.1.2 Forward flight dynamics

Unlike the hovering mode, where lift is generated by means of rotating wings (the propellers), in forward flight, lift is generated by means of aerodynamic surfaces (the wings). Given that in this mode the operating speed is inherently higher, aerodynamic forces play a much more important role than in hovering flight. Additionally, as the UAV acts similarly to a tailsitter aircraft, its pitch angle changes by approximately 90° from hover to forward flight, so a different reference frame was used in this mode, corresponding to this 90° rotation in the pitch axis, as shown in Figure 4.3, in accordance with conventional models for fixed-wing aircraft.

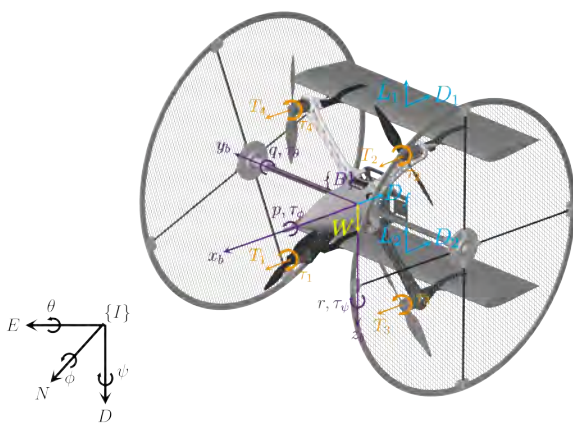


Figure 4.3: UAV model in forward flight mode.

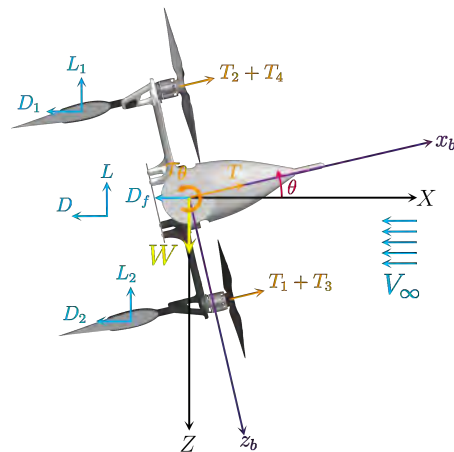


Figure 4.4: Pitch manoeuvre in cruise condition in forward flight mode (tailsitter configuration).

As a base for the forward flight model, [89] was used. Firstly, as a simplification over a detailed dynamic model, lift is assumed to be equally generated by both wings and as such, a resultant lift and drag force is assumed to act at the mid-line uniting the centre of pressure of both wings, coinciding with the x_b axis, as a conventional fixed-wing aircraft. Moreover, as the aircraft is symmetric about the $x_b y_b$ plane, I_{xz} is assumed to be null, further simplifying the equations in [89]. Once again, applying the

equations of motion in Equation (4.1) to the forward flight scenario yields Equations (4.5) and (4.6). It is worth mentioning that, unlike the equations for hovering flight, these are partially written in the body frame, as all aerodynamic forces act orthogonally to the direction of the airflow, which is rotated in relation to the body frame by the angle of attack, α and the side-slip angle β .

$$\dot{n} = v_x c_\theta c_\psi + v_y (s_\phi s_\theta c_\psi - c_\phi s_\psi) + v_z (c_\phi s_\theta c_\psi + s_\phi s_\psi) \quad (4.5a)$$

$$\dot{e} = v_x c_\theta s_\psi + v_y (s_\phi s_\theta s_\psi + c_\phi c_\psi) + v_z (c_\phi s_\theta s_\psi - s_\phi c_\psi) \quad (4.5b)$$

$$\dot{d} = -v_x s_\theta + v_y s_\phi c_\theta + v_z c_\phi c_\theta \quad (4.5c)$$

$$\dot{v}_x = rv_y - qv_z + \frac{F_x}{m} \quad (4.5d)$$

$$\dot{v}_y = pv_z - rv_x + \frac{F_y}{m} \quad (4.5e)$$

$$\dot{v}_z = qv_x - pv_y + \frac{F_z}{m} \quad (4.5f)$$

$$\dot{\phi} = p + qs_\phi t_\theta + rc_\phi t_\theta \quad (4.6a)$$

$$\dot{\theta} = qc_\phi - rs_\phi \quad (4.6b)$$

$$\dot{\psi} = q\frac{s_\phi}{c_\theta} + r\frac{c_\phi}{c_\theta} \quad (4.6c)$$

$$\dot{p} = \frac{1}{I_x I_z} (-I_z(I_z - I_y)qr + I_z\tau_\phi) \quad (4.6d)$$

$$\dot{q} = \frac{1}{I_y} ((I_z - I_x)pr + \tau_\theta) \quad (4.6e)$$

$$\dot{r} = \frac{1}{I_x I_z} (I_x pq + I_x\tau_\psi) \quad (4.6f)$$

Equations (4.7) and (4.8) describe the externally applied forces and torques on the vehicle both due to aerodynamic forces and the actuation of the rotors, written in the body frame. All the coefficients mentioned are shown to depend on a given number of variables, however, simplifications can be made to reduce dependencies. These coefficients (C_L , C_D , C_{D_q} , C_{L_q} , C_Y , C_{τ_ϕ} , C_m and C_{τ_ψ}) depend on the aerodynamic characteristics of the aircraft, and consider the total wing area as a reference area. Furthermore, V_∞ denotes the free stream velocity, while V_a denotes the airspeed of the aircraft, which we assume to be equal, and as such, $V_a = V_\infty$, β is the side-slip angle, b is the combined wing span, c is the wing chord, and S is the total wing area.

$$F_x = -mgs_\theta + T + \frac{1}{2}\rho V_a^2 S [-C_D(\alpha)c_\alpha + C_L(\alpha)s_\alpha + (-C_{D_q}c_\alpha + C_{L_q}s_\alpha)\frac{c}{2V_a}q] \quad (4.7a)$$

$$F_y = \frac{1}{2}\rho V_a^2 S C_Y(\beta, p, r) \quad (4.7b)$$

$$F_z = mgc_\theta c_\phi + \frac{1}{2}\rho V_a^2 S [-C_D(\alpha)s_\alpha - C_L(\alpha)c_\alpha + (-C_{D_q}s_\alpha + C_{L_q}c_\alpha)\frac{c}{2V_a}q] \quad (4.7c)$$

$$\tau_\phi = \frac{1}{2}\rho V_a^2 S b C_{\tau_\phi}(\beta, p, r) + [(\tau_3 + \tau_4) - (\tau_1 + \tau_2)] \quad (4.8a)$$

$$\tau_\theta = \frac{1}{2}\rho V_a^2 S c C_m(\alpha, q) + \frac{d}{2\sqrt{2}} [(T_1 + T_3) - (T_2 + T_4)] \quad (4.8b)$$

$$\tau_\psi = \frac{1}{2}\rho V_a^2 S b C_{\tau_\psi}(\beta, p, r) + \frac{d}{2\sqrt{2}} [(T_2 + T_3) - (T_1 + T_4)] \quad (4.8c)$$

The vehicle is shown in cruise condition (flying at a level altitude, and as such $\theta = \alpha$) in Figure 4.4, with the aircraft flying at the required angle of attack to generate enough lift to maintain level flight. Besides the drag caused by the wings, D_f represents the drag of the remainder airframe. It is also clear from this

figure that the CG is located at a considerable distance from the centre of pressure, a phenomenon that will lead to the need for a constant thrust differential to balance the aerodynamic pitching momentum and maintain the cruise pitch angle, as previously described in Section 3.2.3.

Unlike the hover mode, in forward flight, the vehicle's pitch and yaw angles are controlled using differential thrust, while the vehicle's roll angle is manipulated using differential torque.

4.1.3 Ground dynamics

In ground mode, the vehicle operates similarly to the hover mode, and as such the same coordinate frames as defined in Figure 4.1 are used. From the model defined for hovering, however, several conditions must be defined that characterise the robot's locomotion on the ground. The adaptation required for this type of locomotion is based on [90].

Only locomotion on flat horizontal surfaces will be considered, so the vertical position d is constant, $\dot{d} = 0$ and $v_d = 0$. Since the vehicle rolls on a flat surface and both wheels should be in contact with the ground, the roll angle should be constant and zero, so $\phi = 0$ and $\dot{\phi} = 0$. Assuming no slippage occurs in the wheels, the vehicle may only move in the direction imposed by its wheels, meaning it cannot move in the y_b direction, and so $v_y = 0$, or in the inertial frame $-\dot{n}s_\psi + \dot{e}c_\psi = 0$. To ensure the robot does not lift off the surface it is rolling on, the thrust must satisfy $Tc_\theta < mg$. As there is a component of the thrust vector in the vertical direction, the total reaction force of the wheels with the ground is $N = mg - Tc_\theta$. Lastly, considering the bearing is frictionless, the kinematic friction between the wheel and the ground surface is also neglected, meaning the only dissipative force considered in the robot dynamics is the aerodynamic drag. With no resistance acting on the bearings, the wheels and the UAV's frame act as decoupled bodies. However, when thrust is applied, static friction does act on the wheel, which makes the wheel spin, as seen in Figure 4.5, where we assume there is no slippage.

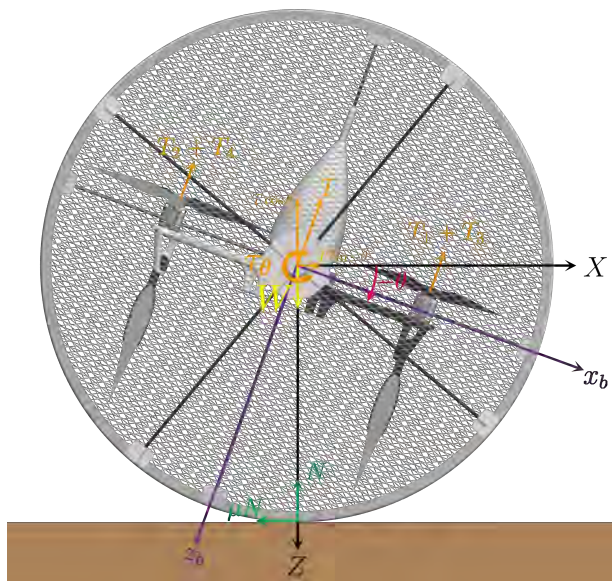


Figure 4.5: UAV model for ground locomotion.

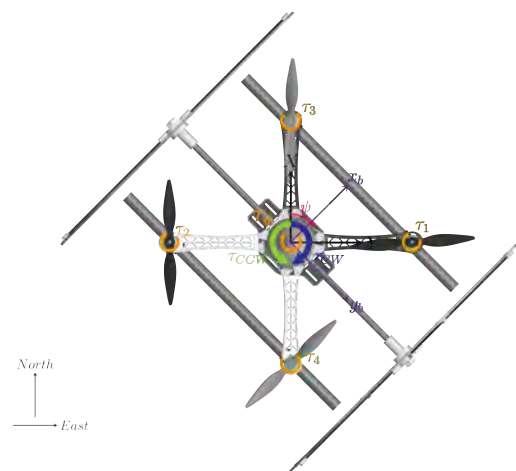


Figure 4.6: UAV model for yaw control in ground mode.

Figure 4.5 illustrates how the vehicle rolls on the ground by pitching forwards, thus partially directing the thrust horizontally. To control the direction of movement of the robot, the yaw angle is controlled, with the same mechanism as a quadcopter, as shown in Figure 4.6.

Equations (4.9) and (4.10) describe the dynamics of the robot while rolling on the ground. Note that these equations are further simplified to reduce the number of state variables.

$$\dot{n} = v c_{\psi} \quad (4.9a) \qquad \dot{\theta} = q \quad (4.10a)$$

$$\dot{e} = v s_{\psi} \quad (4.9b) \qquad \dot{\psi} = \frac{r}{c_{\theta}} \quad (4.10b)$$

$$\dot{v} = -\frac{T}{m} s_{\theta} - \frac{1}{2m} \rho S C_{D_x}^{hover} sgn(v) v^2 s_{\psi} \quad (4.9c) \qquad \dot{p} = qr \frac{I_y - I_z}{I_x} + \tau_{\phi} \frac{1}{I_x} \quad (4.10c)$$

$$\dot{q} = pr \frac{I_z - I_x}{I_y} + \tau_{\theta} \frac{1}{I_y} + \frac{d_{ca}}{2I_y} C_{D_x}^{hover} \rho S sgn(v) v_x^2 \quad (4.10d)$$

$$\dot{r} = pq \frac{I_x - I_y}{I_z} + \tau_{\psi} \frac{1}{I_z} \quad (4.10e)$$

Inclined surfaces

As previously mentioned, the model describes the movement on flat surfaces. For inclined surfaces, the condition ensuring the vehicle is always in contact with the surface must be revised to $T \cos(\gamma - \theta) < mg \cos \gamma$. Similarly, the reaction force becomes $N = mg \cos \gamma - T \cos(\gamma - \theta)$. As the inclination of the surface increases, this reaction force decreases, and so does the contact friction of the wheels with the surface. Considering the case where the robot rolls perpendicular to the direction of the inclination, without rolling up or down ($\dot{d} = 0$), the vehicle relies only on static friction from the wheels not to slip down the inclination, as no component of the thrust vector is directed along the inclination. Therefore, if the inclination is significant enough such that the weight component along the inclination is greater than the maximum static friction, $\mu_{static}(mg \cos \gamma - T \cos(\gamma - \theta)) < mg \sin \gamma$, the vehicle may only roll in the direction of the inclination, or in its close proximity. With this restriction, the vertical velocity now becomes $\dot{d} = \sqrt{v_n^2 + v_e^2} \tan \gamma$. In the limit case where $\gamma = 90^\circ$, the UAV acts as if in the hover mode.

4.2 Control laws

To ensure the vehicle's operability in all modes and to enable automatic operation, control laws need to be applied consistently. Typically, the following architecture is employed in hover, forward-flight and ground modes: In the final stage, a motor mixer receives high-level motor demands and translates them into individual motor requests in PWM. Before this, the attitude controller, based on a given attitude (or attitude rate) request, generates high-level motor demands. When applicable, a position controller outputs attitude targets, from a given position target. Before this, a waypoint navigator handles a given mission,

producing as an output a given position target. Depending on the specific control mode, some or all of these controllers can be active and the pilot input is handled accordingly. In this section, the controllers implemented by ArduPilot and implemented in this work will be described, for all of the vehicle's modes of operation. The order in which they will be described goes from the innermost loop to the outermost loop. This architecture is later described for each control mode in Section 4.3 and additionally in Annex C.

The following description is primarily based upon the existing ArduPilot documentation [62], when available and up to date, but mostly obtained from analysing the code, both existing and modified during this work, where each different controller and control mode is implemented. Note that the described control architecture is relative to version 4.4 of ArduPilot, which was the version used, however, an updated diagram for version 4.5 is provided in Annex A.

Lastly, it is worth mentioning that the Extended Kalman Filter (EKF) implemented by ArduPilot is often used as a source of observations for many of the implemented controllers, however, its implementation is beyond the scope of this work. An overview of the EKF is available in the developer documentation [91].

4.2.1 Motor mixer

The motor mixer is the lowest level layer, acting immediately before the motor output. Its function is to determine the individual motor outputs, from a given input of requested actuation in the pitch, roll and yaw axis (in the body frame) and requested throttle. These inputs are expected in the range from -1 to 1 and are dimensionless. The pitch, roll and yaw inputs are analogues to normalised torque demands, meaning that an input of 1 in pitch corresponds to a request of the maximum differential thrust that can be produced leading to a rotation in the positive direction about the y-axis. The motor mixer is solely dependent on the frame characteristics and as such, is common throughout all operating modes of the vehicle, where the same set of actuators is used. Note however that the pitch, roll and yaw body-frame angles are considered as those described in the hovering frame of reference.

The process through which the inputs are converted into motor outputs is described by Equation (4.11).

$$\begin{bmatrix} M_1 \\ M_2 \\ M_3 \\ M_4 \end{bmatrix} = RPY_{scale} \begin{bmatrix} -\frac{1}{2} & \frac{1}{2} & \frac{1}{2} \\ \frac{1}{2} & -\frac{1}{2} & \frac{1}{2} \\ \frac{1}{2} & \frac{1}{2} & -\frac{1}{2} \\ -\frac{1}{2} & -\frac{1}{2} & -\frac{1}{2} \end{bmatrix} \begin{bmatrix} R_\tau \\ P_\tau \\ Y'_\tau \end{bmatrix} + \begin{bmatrix} 1 \\ 1 \\ 1 \\ 1 \end{bmatrix} T' \quad (4.11)$$

Firstly, the requested roll and pitch actuation, R_τ and P_τ , are directly used. The yaw input is then constrained to the amount of yaw actuation that can be applied, given the physical constraints of the motor output, which must be at a minimum the yaw headroom, defined by the firmware parameter $Q_M_YAW_HEADROOM$, from where Y'_τ is obtained. This vector is multiplied by a matrix which defines the contribution of each motor to the rotation about each axis, which depends on the motor layout, and orientation. This matrix can be easily obtained for an X-type quadrotor frame.

Lastly, the throttle input is scaled, such that the motor output of a given motor is not greater than 1 (to this effect, the result from the pitch, roll and yaw actuation is also scaled, using RPY_{scale}), such that the

attitude requests are not compromised, but the requested average throttle is still produced, from where T' is obtained. This value is multiplied by a vector which characterises the orientation of each motor. As all motors point directly upward, all contributions are defined as 1. With this, the motor outputs (M_1 , M_2 , M_3 and M_4) from 0 to 1 are obtained. Depending on the autopilot output parameters, this value is then converted to a corresponding PWM value (typically from 1000 to 2000). The motor mixer can also include other features, such as compensating the throttle to account for a change in battery voltage [63].

4.2.2 Attitude rate controller

Above the motor mixer, the attitude rate controller is responsible for controlling the angular velocity of the vehicle, ω . To do so, pitch rate, roll rate and yaw rate are controlled separately, following a Single-Input Single-Output (SISO) strategy, as described in Figure 4.7. For each of these rates, a Proportional Integrative Derivative (PID) loop is implemented, following the structure in Figure 4.8, which differs from a simple PID loop.

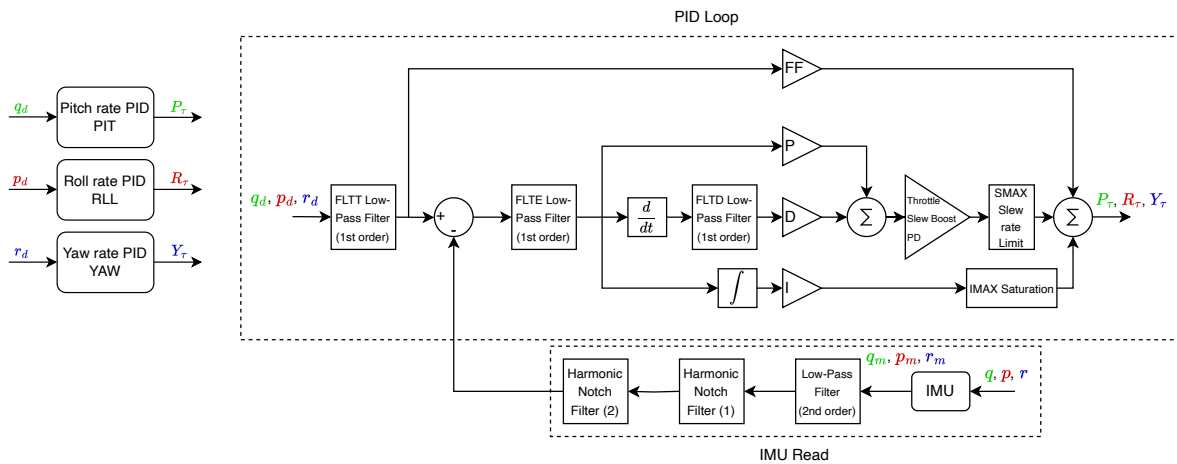


Figure 4.7: Attitude rate controller diagram.

Figure 4.8: PID controller diagram.

The PID loop frequency is tied directly to the main loop frequency of the autopilot. For the Plane firmware, this is set by default at 50 Hz, and for the Copter firmware at 400 Hz. A quadplane, as our vehicle, which runs code from both modes, uses a main loop frequency of 300 Hz by default. Similarly, the EKF used by ArduPilot for state estimation is considered not fast enough to supply observations to the attitude rate controller, therefore, the measurements from the gyroscopes in the IMU are used. However, these measurements are susceptible to noise, so they are passed through a 2nd order low-pass filter, which aims to remove any background noise that may be present, and up to two harmonic notch filters, which reduce the intensity of the blade passage noise, and its corresponding harmonics. Depending on the hardware available, the notch frequencies can be set up differently [92]. This IMU read loop is run at the IMU sampling frequency, which depends on the gyroscope used, with the sampling rates of the CubeOrange gyroscopes varying between 8.108 kHz and 9.100 kHz, as checked in the autopilot logs. Only the first healthy gyroscope is used to provide measurements to the controller.

The control architecture features a PID controller with a feed-forward term (FF), enhancing its versatility across different aircraft configurations. In particular, for tailsitters with aerodynamic control surfaces, the feed-forward component is the main pathway used [93]. The controller gains can be either tuned manually, through the QAUTOTUNE control mode, or using the VTOL QuikTune lua script [94], however, the FF gain must always be tuned manually.

In addition, throughout the control law, several filtering steps are applied, first to the target (FLTD), then to the error (FLTE) and lastly to the derivative component (FLTD). The goal of these filters is to reduce any oscillations that may originate from higher-level control loops. Note that by default all axes have the target filter present, but only the pitch and roll axis controllers have a filter on the derivative component, whose goal is to reduce high-frequency noise, which could increase the D term incorrectly. In the yaw axis on the other hand, the FLTD filter is replaced with a filter on the error, due to the actuation response being faster in this axis, as a rotor will produce a torque faster than thrust.

With regards to limiting the output, a parameter-controlled saturation for the I component is possible using IMAX, and the P and D components can also be limited, if a slew rate higher than SMAX is observed on the control actuation output. Besides that, when a high slew rate is observed on the throttle, a boost multiplier is applied to the P and D components.

Lastly, it is crucial to mention that for a tailsitter with no control surfaces, as is the case, this rate controller is shared by all operating modes. In order to be used in the forward flight mode, the desired rates are previously rotated into the hovering body frame. Due to the implementation of the ground mode, the same rate controller is used, but with the possibility of using different gains due to the change in dynamics from hover to ground. However, the same gains were applied. Despite the implementation of ArduPilot sharing the attitude rate controller with the same gains between the forward flight and hover modes, as previously seen in Section 4.1.2, the dynamics in these two modes are significantly different, mainly due to the higher airspeed experienced in forward flight which implies that aerodynamic forces are much more significant than in the hover mode. Having said that, a better approach might have been to use different gains for the forward flight mode.

4.2.3 Attitude controller

The attitude controller controls the attitude angles of the UAV, roll, pitch and yaw. Unlike the rate controller, the attitude controller uses the EKF as the measurement source to compute the attitude error since the flight controller cannot directly measure attitude angles. These angles are estimated from the available sensors using the EKF. The angle controllers, in all three locomotion modes, are run at the main loop frequency, which in this case is 300 Hz.

Hover controller

The first component of the attitude controller is the input shaping loop. This layer receives the desired attitude angles, from either the pilot input or a higher level input. This input can be provided in several forms, which are appropriately converted. However, the most relevant input is a vehicle attitude defined

by a roll, pitch and yaw angle. It is worth noting that it is also possible to only control the roll and pitch angles at the angle level, with the yaw axis rotation being controlled at the rate level.

The goal of the input shaping, as implied by its name, is to shape the input such that a similar response can be observed across a wide range of different aircraft. To do so, the output to the remainder of the attitude controller is a target angular velocity, which takes into account velocity and acceleration limits, and a time constant of the response. This angular velocity is integrated and appropriately converted to a quaternion format, which is then passed as a desired attitude to the controller. Simultaneously, the requested target angular velocity is passed as a feedforward term at the end. Although shown here, when input is given directly to the attitude rate controller and not through the attitude control, input shaping is also available at that level.

As mentioned, the core of the controller receives the desired attitude of the UAV in a quaternion format, despite the controller being built for Euler angles and receiving angular errors. This is so that problems such as gimbal-lock can be avoided, and with that, the controller can perform better in situations like recovering from a flipped orientation. To obtain the angular errors, two quaternion rotations are computed, one to match the thrust vector with the desired thrust vector, and another to rotate the heading.

Figure 4.9 displays the block diagram of the angle controllers. For each angle, a similar P controller architecture is implemented.

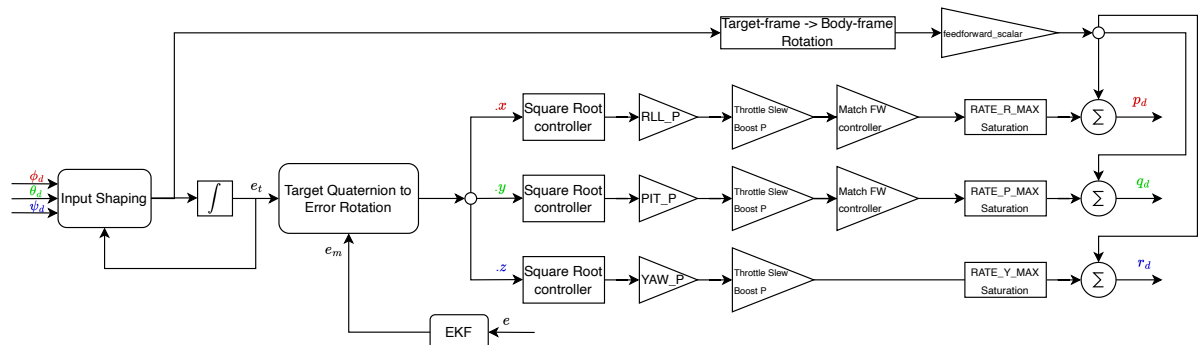


Figure 4.9: Attitude angle controller.

The first aspect worth mentioning is the ability to use a square root controller, which acts as a non-linear proportional controller.

When active, the square root controller schedules the proportional gain in a non-linear fashion, as a function of the error, with the goal of limiting the resultant angular acceleration. It does so by first presenting a linear output when the error is below the linear distance threshold, and after that outputting a square root function. Both the square root function and the linear distance depend on the second order limit, which in the angle controllers is half of the angular acceleration limits defined in the parameters. The linear distance is obtained as $d = \frac{l}{P^2}$, where l is the second order limit, and thereafter, the square root output segment has the following output, $sgn(error) \sqrt{2d(error - \frac{d}{2})}$. In the linear segment, the output is equal to the error, as the output of the square root controller is then multiplied by the P gain. Figure 4.10 illustrates the output function of the square root controller used in the roll and pitch axis.

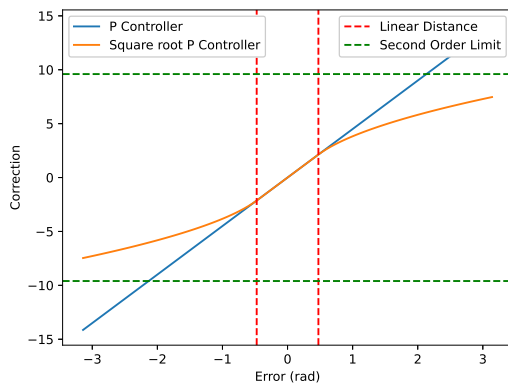


Figure 4.10: Roll/Pitch square root controller output.

In addition to this, the P gain may also be scaled in two scenarios, when there is a high slew rate on the throttle input (similarly to the mechanism present in the rate controller), which applies to all axes, and when the P gain should match the gain of the fixed-wing angle controller, such as in position control modes which transition between modes, which only applies to the roll and pitch axis, as there is no yaw angle controller for fixed-wing modes.

At last, the feedforward term from the input shaping layer can be scaled, such that when the thrust angle error (i.e., the angle between the current thrust vector and the thrust vector in the desired attitude) is higher than 30° , the feedforward component is smoothly removed, until the thrust angle error is twice the limit. At that point, the yaw rate output is also completely removed.

Ground controller

As previously observed, the hover and ground dynamics are similar, in what concerns the vehicle attitude, and as such, the same controller architecture is used in both modes. Such that different gains and mostly angular and angular rate limits could be used, a second instance of this controller is used for ground locomotion.

Unlike the PID solution proposed in [90], where the roll angle is not controlled by the attitude controller, in ground mode the attitude controller has a constant desired roll angle of zero. This means that whenever a disturbance is encountered that lifts only one of the wheels, the controller will try to set the wheel back on the ground. However, when the vehicle is rolling on an inclined surface, perpendicular to the direction of the inclination, setting a roll angle target of zero will lead to an asymmetric normal force on the wheels, as the controller tries to level the vehicle, by trying to lift the lower wheel, which is undesired. Ideally, the roll angle target would be set equal to the lateral (with respect to the vehicle) inclination of the surface the vehicle is rolling on, which would require knowing the inclination angle.

Although not present in the developed vehicle, several solutions could be implemented to measure the inclination. For example, an array of three distance measuring sensors (such as SONAR or LiDAR) pointing downward could be installed, from where knowing the attitude of the frame with respect to the inertial frame, and the position of each sensor, the inclination of the surface could be computed.

Forward flight controller

In forward flight mode, only roll and pitch are controlled, with the yaw rate being provided as an input, and so, only pitch and roll angle controllers are active in any fixed-wing mode. These controllers are present in Figures 4.11 and 4.12.

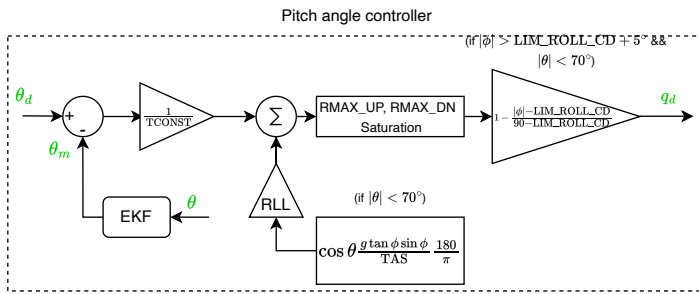


Figure 4.11: Pitch angle controller.

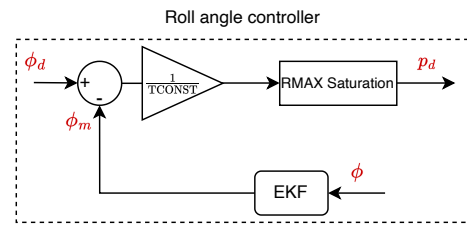


Figure 4.12: Roll angle controller.

The main component of both controllers is the $\frac{1}{T_{CONST}}$ proportional gain, which for each axis uses a time constant to define how quickly the aircraft responds by obtaining an angular rate from the angular error. A higher TCONST value means that the aircraft will respond more slowly in that particular axis and vice-versa.

The pitch angle controller in particular, besides the proportional gain and rate saturation, features two extra steps. The first corresponds to a rate offset that is added, corresponding to the pitch rate necessary for the aircraft to maintain altitude in a coordinated turn. This offset is multiplied by a parameter-defined gain, which by default is 1. The second is a protective mechanism for when the aircraft is operating in high roll angle conditions. Whenever the roll angle of the aircraft is above the defined threshold, the pitch rate output is linearly scaled such that it is zero at a roll angle of 90° . This is because the priority is to bring the aircraft back to level flight, and in fact, a pitch rate in such conditions will induce inertial frame yaw. Both of these steps are only active when the pitch angle is below 70° .

Finally, it is important to note that the angles referenced in this controller are in the forward-flight frames of reference, while the attitude rate controller previously described, works with angles in the hovering reference frames. As such, the pitch and roll rates (q_d and p_d) output by this controller, and the yaw rate commanded are rotated into the multicopter body frame before they are sent as inputs to the attitude rate controller, in forward flight mode.

4.2.4 Position controller

The position controller enables control over the translational dynamics of the vehicle. Unlike the attitude controllers, the position controller design for hover and fixed-wing mode differs significantly due to the different nature of how flight is maintained in each mode, as the aircraft can hold a position in hover with no velocity, while in forward flight a minimum airspeed is required, so the UAV cannot hold a position in mid-air. The forward flight position and waypoint controllers are separately described in Annex B.1.

Hover controller

When operating in hover modes, the position controller is split into two separate controllers, a horizontal controller, responsible for controlling the north and east components of the UAV's position, and a vertical controller, which controls the vehicle's height. Both controllers receive as inputs a target position, velocity

and acceleration. In doing so, higher-level controllers or specific control modes can achieve specified manoeuvres and adequately handle the pilot input. Both controllers in this mode are run at the main loop frequency, of 300 Hz.

At a higher level, both controllers can be split into three different components. The first is a P controller which converts a position error into a velocity correction. After that, a PID controller converts a velocity error into an acceleration correction. Lastly, in the horizontal controller, the target accelerations are converted into the target lean angles, and a target yaw and yaw rate are calculated. In the case of the vertical controller, this last step is a PID controller which converts an acceleration error into a throttle output. In between each of these components, the target velocity and acceleration, respectively, are added as feedforward terms. The horizontal position controller block diagram is presented in Figure 4.13.

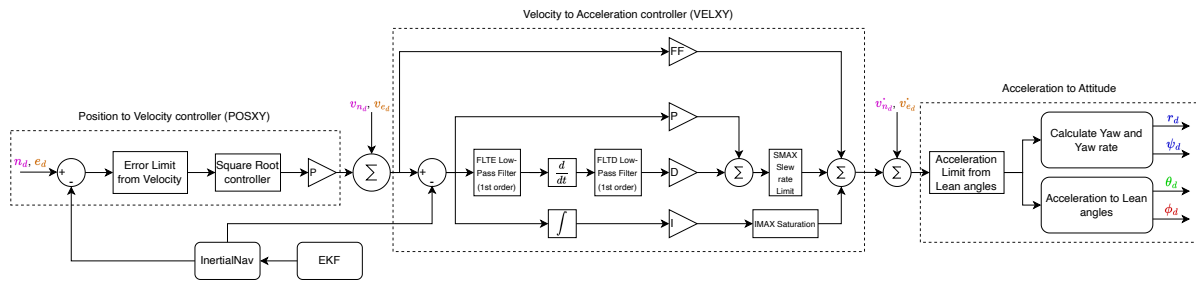


Figure 4.13: Horizontal position controller.

First, it is important to notice that the error (and target) of the position controller are limited according to the maximum velocity correction. Since a square root controller is used, to obtain the error limit from the maximum velocity output, the inverse of the square root controller is used, which in the linear part follows simply as $\frac{V_{\max}}{P^2}$, and in the non-linear segment follows as $\frac{a_{\max}}{2P^2} + \frac{V_{\max}^2}{2a_{\max}}$. This limit is also referred to as a leash limit, as from the maximum velocity correction it limits the position target. Having said this, the second-order limit used in the square root controller is an acceleration limit.

The PID controller used for velocity control follows a similar structure to those previously presented in the attitude rate controller, apart from not filtering the target, and boosting the P and D components. By default, the feedforward gain is null.

At last, the desired acceleration commands are converted to desired lean angles. First, the north and east component accelerations are rotated into a forward and lateral acceleration, from the vehicle frame of reference. These are then limited from what is achievable by the UAV, given its maximum lean angles, by inversely converting these maximum lean angles into maximum accelerations. With that, the pitch and roll angles are obtained directly from the forward and lateral acceleration, respectively, by applying the formula $\theta = \arctan\left(\frac{a_f}{g}\right)$, for the example of the pitch axis. To calculate the desired yaw, the angle of the desired velocity vector is used, with respect to the north direction. A yaw rate is also calculated, which is obtained from the turn rate, which is calculated from the forward and turn acceleration, although it is unused.

To control the vertical position of the vehicle, a similar architecture is used. The vertical position controller block diagram is shown in Figure 4.14. Similar to the horizontal controller, a vertical position,

velocity and acceleration can be passed as input to the controller, although usually either a position or velocity target is used.

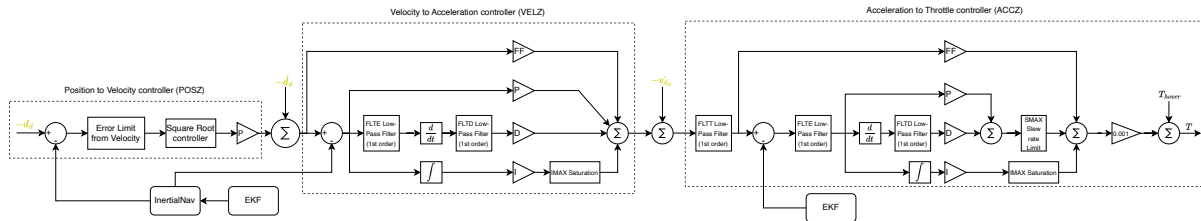


Figure 4.14: Vertical position controller.

As in the horizontal controller, a P controller is used to go from position to velocity, where in this case the velocity limitation is not symmetric, as the climb rate limit can be different from the descent rate limit. The PID controller used to convert a velocity error into an acceleration correction, however, does not have a slew rate limit on the output.

Finally, the PID controller used to obtain the throttle output follows the same structure as the PID controller used in the attitude rate controller, without the possibility of boosting the PD gains. The output of this controller corresponds to the throttle correction with respect to the hover throttle value, and so, to obtain the throttle output, the hover throttle must be added. This output is sent directly to the motor mixer. The hover throttle is updated, when the parameters are set to do so, by whenever the vehicle is maintaining altitude, setting the hover throttle value to the current throttle output. Although not mentioned, the acceleration to throttle controller can have a mechanism to compensate for vibrations, which changes the behaviour of the PID loop. By default, both PID controllers also have a null feedforward gain.

Ground controller

To maintain position control while operating in ground mode, a position controller that follows the same architecture as the hover controller is used. This is because the translational dynamics are very similar in both situations. However, while rolling on the ground, the direction of movement is exclusively controlled by the yaw, as the vehicle can only move forward. Despite using the same architecture, different parameters for this controller are used, particularly for the velocity limits. As the vehicle cannot move using its roll angle on the ground, only the pitch target is used from the lean angle outputs. Note that in hover mode, only the pitch and roll angles are required to fully control the horizontal position of the aircraft (with the yaw angle possibly being separate from this controller), while in ground mode, the pitch and yaw angles are required. The yaw angle comes from the higher-level waypoint controller in ground modes.

Since the vehicle is designed to operate primarily on flat surfaces, only the horizontal controller is used. As will be detailed in Section 4.3.3, in all ground modes the throttle value is set to a fixed value. This results in the ground velocity being controlled using the pitch angle, which limits the maximum speed of the vehicle, and its ability to climb inclinations. In order to better tackle these challenges, a separate controller would be required, that ensures the no take-off condition is respected, and that the aircraft adequately adjusts its throttle to control both velocity and height (when rolling up inclinations). A similar

approach to the Total Energy Control System (TECS) used in forward flight could be followed with this goal. Still, knowledge of the inclination of the surface the vehicle is on would once again be required.

4.2.5 Waypoint controller

Hover controller

In hover mode, a navigation controller acts on top of the position controller, running at the same main loop frequency. It takes in an origin (usually the previous waypoint) and the next waypoint, and computes an S-curve trajectory to reach the next waypoint. Then, at each iteration, the navigation controller provides updated target positions, velocities, and accelerations to the position controller, by advancing along the computed trajectory. The S-curve path corresponds to flying directly toward the next waypoint, with attention to both the previously covered track and the next track to be covered, such that a smooth continuous trajectory is achieved. Note that this is done both for the horizontal position and for the vertical position, with each waypoint being a 3D position in space.

The full description of the S-Curve navigation algorithm is beyond the scope of this work, with a more detailed description being available in [95], but in summary, it generates a trajectory with continuous position, velocity, acceleration and jerk (the acceleration rate of change). It does so by calculating a path between two different waypoints with 23 segments, corresponding to:

1. 1 initial segment;
2. 7 segments forming the acceleration (which bring the vehicle up to its target velocity for that path);
3. 7 segments forming the velocity change (which bring the vehicle up to its target velocity, when it is changed during the path);
4. 1 constant velocity segment;
5. 7 segments forming the deceleration (which bring the vehicle down to its target velocity for the next path).

Figure 4.15 illustrates the described segments in an example situation where the velocity is not changed during the path. The periods where the snap is not null are given by the function $J(t) = \pm \frac{J_p}{2}(1 - \cos(\frac{\pi}{T}t))$, where J_p is the maximum snap, and T is the duration of the segment. Note that in Figure 4.15, each segment has a duration of 1 time unit for illustration purposes, but each segment may have a different duration.

The desired position, velocity and acceleration are obtained by sampling the S-curve, and applying a scaling factor to the time instant sampled, which accounts for the tracking error. This scaling factor slows the progression along the S-curve if the position target is moving too far ahead. Each S-curve leg is computed taking into account the previous leg, the current leg, and the next leg, and all the requirements for the aircraft to be able to achieve the specified trajectory, meaning, in each leg, it must be able to accelerate and decelerate back, taking into account the velocity, acceleration and jerk limits, and the maximum snap (the rate of change of jerk), obtained from the maximum angular accelerations.

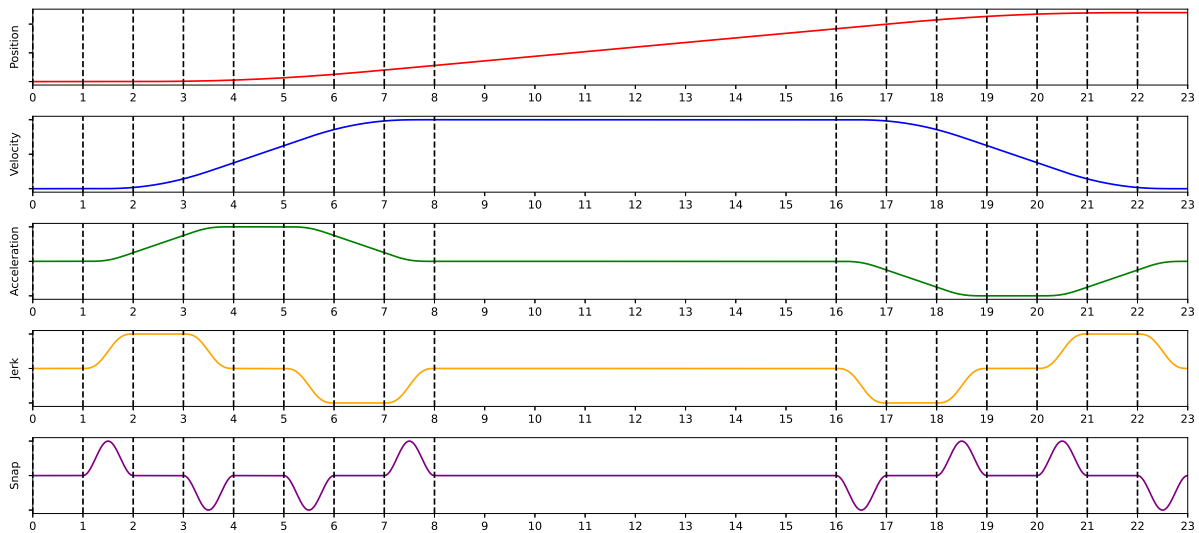


Figure 4.15: S-Curve Navigation Profile example.

Ground controller

While operating in ground mode, the same navigation controller architecture is used as in hover mode, with the exception that no vertical position controller is used, and thus, the vertical position target is unused. Nonetheless, different parameters are used in ground mode, namely the waypoint speed, and acceleration and jerk limits. Not related to the vehicle dynamics but rather to the operating environment, in ground mode the vehicle should generally move slower, as it is not moving in an obstacle-free environment. To obtain the desired yaw angle, the bearing from the current position to the target waypoint is used.

4.3 Control modes

As a higher-level layer, with which the pilot directly interacts, are the different control modes. Each mode defines and characterises the input that is received from the pilot and the control that is provided by the autopilot. Except for the AUTO mode, each control mode is specific to a type of locomotion, either hover, forward flight or ground. For each mode, a block diagram is presented, displaying how the different controllers are used and linked together in each mode. The full list of the default ArduPlane flight modes is available in [96]. The p subscript denotes pilot input. Whenever the pilot input is obtained via the remote controller, parameters define the corresponding values of maximum and minimum stick deflection, as well as the centre value.

4.3.1 Hover modes

In hover mode, the aircraft can be flown with different levels of control, depending on the type of mission being flown. The modes that are specific to hovering flight are prefixed with the letter Q, as a reference to QuadPlane, being the default modes available to QuadPlanes in ArduPlane [97].

QHOVER

In QHOVER mode, the aircraft hovers maintaining altitude and levels itself on the roll and pitch axes. The pilot inputs the target pitch and roll angles and yaw rate, using the sticks, and the throttle stick commands the desired climb rate.

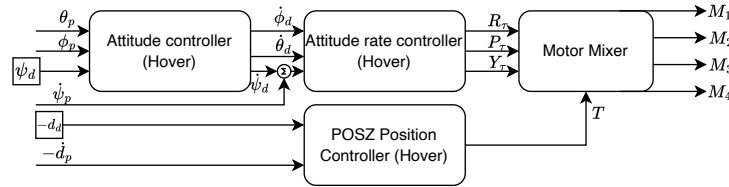


Figure 4.16: QHOVER mode.

QLOITER

In QLOITER mode, the aircraft hovers maintaining altitude and position. The pilot requests a target climb rate and yaw rate, and with the pitch and roll sticks, the pilot inputs lean angles are converted to accelerations which are the input to the position controller, to change the position of the vehicle.

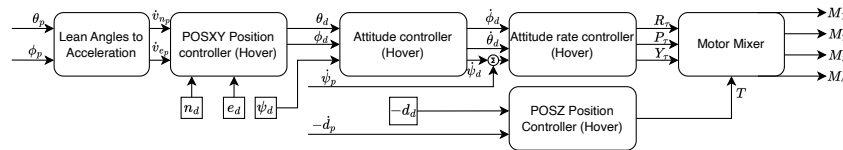


Figure 4.17: QLOITER mode.

4.3.2 Forward-flight modes

When operating in forward flight, as the vehicle is fully controlled by its motors, with no aerodynamic control surfaces, it always flies in what is called assisted fixed-wing flight. As this feature is always active, flying in MANUAL mode is not possible.

FBWA

In FBWA mode the aircraft levels itself on the roll and pitch axis. With the pitch and roll stick, the pilot controls the desired pitch and roll angles, with the yaw stick controlling yaw rate and the throttle stick the throttle sent to the motor mixer.

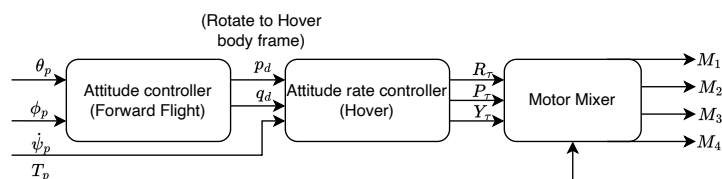


Figure 4.18: FBWA mode.

4.3.3 Ground modes

The original ArduPlane implementation does not provide any ground modes (other than ground steering, for planes that support it), and so the following modes were added to enable ground functionality. All ground modes are prefixed with the letter R, standing for Rover. Note that ArduPilot supports rovers in the ArduRover firmware, however, that is implemented separately from the aerial vehicle code and is not directed towards passively actuated multimodal vehicles, as is the case, so a different approach from that used in ArduRover was taken.

RMANUAL

In RMANUAL mode, the vehicle levels itself on the pitch axis. A fixed roll target of 0 is set, as previously explained. The pilot controls the pitch angle, which causes the vehicle to roll forward or backward, and the roll stick controls the steering of the robot, meaning the yaw rate. The throttle stick is solely used to control the throttle, which together with the pitch angle determines the velocity at which the vehicle rolls. In this mode, the pilot throttle is limited to a quarter of the maximum throttle so that the vehicle does not take-off.

This mode was implemented as a way to tune the ground attitude controllers, and manually perform high-speed manoeuvres on the ground.

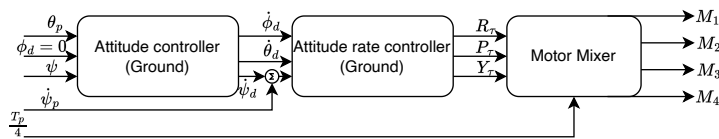


Figure 4.19: RMANUAL mode.

AUTO

While driving on the ground through an AUTO mission, the robot rolls to each waypoint. The velocity at which it does so is characterised by a parameter. No pilot input is necessary, apart from the mission planning. Due to the adopted implementation of the position controller, ground missions are only possible on close to flat surfaces.

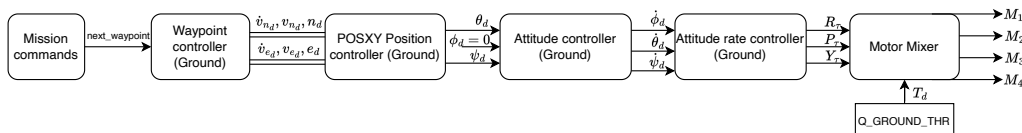


Figure 4.20: Ground AUTO mode.

4.4 Transition controller

A transition between modes occurs whenever a MAV_CMD_DO_VTOL_TRANSITION command is present in a mission (some of these commands are described in Annex B.2, including this command which was modified to implement the transition to ground mode), a control mode commands a transition, or there is a change in control mode that requires the vehicle to transition modes. For example, changing from QHOVER mode to FBWA mode requires the vehicle to go from hover to forward-flight.

4.4.1 Hover \longleftrightarrow Fixed-wing transition

The transition between hover and forward flight corresponds to a pitch manoeuvre where the aircraft is rotated on the pitch axis by about 90° , and gains or loses airspeed. During these transitions, the attitude control is fully assured by this controller, with the pilot having no control over it.

To execute both transitions, a similar implementation is followed. During the first segment, this controller sends a pitch input to the attitude controller, corresponding to a slope starting at the current pitch angle and with a rate defined by a parameter. When a parameter-defined angle is reached, the aircraft is considered to have successfully completed the transition, and so, control is handled over to the corresponding target mode, and the pitch angle slope is continued until 0° or 90° , now as a target limit, rather than an input. Both transitions can have different parameters, although, by default, the same parameters are used [98].

During the hover to fixed-wing transition, before the transition angle is reached, the throttle output is the pilot throttle, or the hover throttle, whichever is greater, while in the fixed-wing to hover transition, a fixed defined value is used (which can be defined as the hover throttle value). In either case, during the transition a target roll value of 0 is sent to the attitude controller. Figure 4.21 illustrates both transitions along time and the respective commands that are sent. Note that the pitch angle reference is considered as that in the mode the vehicle is transitioning from.

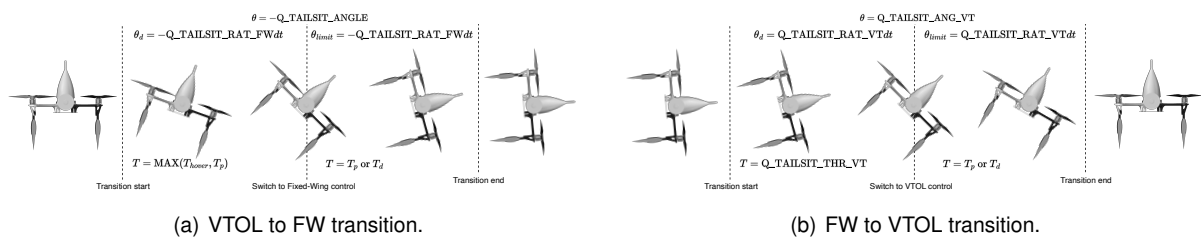


Figure 4.21: Tailsitter transition.

4.4.2 Hover \longleftrightarrow Ground transition

Unlike the other transitions, which typically occur in flight, a transition to or from ground mode only occurs while the vehicle is on the ground, stationary. As such, no controller is required for a smooth transition, and instead, as the architecture of the hover controllers is very similar to that of the controllers used in ground mode, the control is instantly switched from one mode to another.

Chapter 5

Experiments & Results

In this section, all experiments made during both the design phase and in an operational environment are described. The results obtained from each test are analysed and appropriate conclusions are drawn.

5.1 Propulsive system

The first experiments conducted during the design phase were the propulsion tests. Their goal was to support the design process by validating the predictions from eCalc, upon which the design choices were based comparing different configurations, and to provide further insights into the performance of the propulsive system. Lastly, given its potential relevance in both establishing a method for estimating the inclination of a surface in ground locomotion and further analysis of flight logs, a thrust mapping of the throttle value for the chosen motor propeller combination was also established from the tests. To achieve these goals, static and dynamic tests were performed to replicate the conditions experienced in both hovering flight/ground locomotion and forward flight, respectively.

5.1.1 Test bench

To evaluate the performance of the propulsive system, each configuration was tested separately using a Tyto Robotics Series 1585 thrust stand [99]. This thrust stand can measure the thrust and torque produced by the propeller. By running the power to the ESC that feeds the motor through the measuring circuit, the voltage and current going into the ESC can also be measured. An accelerometer fitted in this measuring circuit measures vibration and an optical RPM sensor was installed to measure the rotational speed of the motor. During all tests, the published limits for the test bench were adhered to, which can be consulted in the datasheet available in [99], along with the error margins for each measurement.

To control the PWM signal sent to the ESC, the RCBenchmark software was used, where automated tests were set up. For each test, the throttle was increased to the maximum over 15 seconds at a constant rate, maintained at the maximum for 5 seconds, such that an average measurement could be taken, and then lowered back down over 20 seconds. The relevant measurements are taken as an average over the 5 seconds at maximum throttle. From the smooth throttle increase, a look-up table of PWM

signals and corresponding thrust value was also created. Before each test, the load cells were tared to remove the drag of the structure from the measurements. The data was sampled at a variable frequency (approximately 60 Hz), depending on the speed of the computer that runs the software, and each data point taken is the average of 20 samples.

The propulsion tests were carried out in the Portuguese Air Force Academy (AFA) wind tunnel, to be later described in Section 5.2.1, where both dynamic and static (i.e. with and without an incoming flow) propulsion tests were carried out. For all tests, a Hobbywing Skywalker 60A ESC was used to control the motor. Instead of powering the system using a battery which would become depleted during the tests, and thus present a lower voltage, a fixed voltage power supply was used, set to a voltage of 16.8 V (which is that of a full 4S battery) and connected by a long cable. Figure 5.1 shows the setup used in the wind tunnel for the propulsion tests.

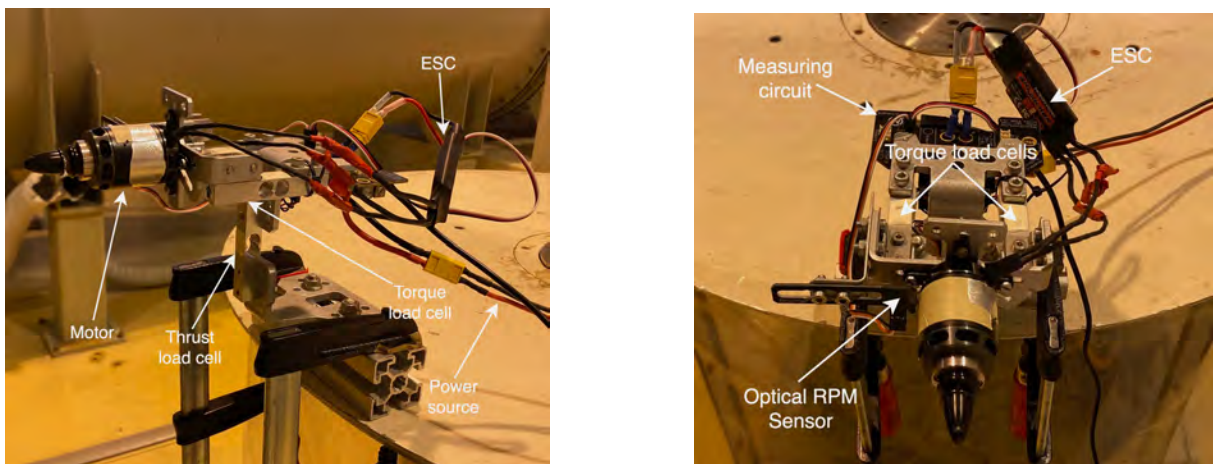


Figure 5.1: Wind tunnel propulsion tests setup.

Considering the results obtained in Section 3.3, the configurations with the T-Motor AIR 2213 motor were excluded, due to their reduced performance and efficiency. Only the DJI 2312E motor with the APC 9x6E and DJI 9450 propellers and the T-Motor AT2814 motor with the APC 9x6E propeller were tested. Each configuration was tested at different airspeeds, ranging from static (0 m/s) to 22.3 m/s.

5.1.2 Propulsive performance

From the direct results of the propulsion tests, a mapping of the corresponding thrust value of each motor for a given PWM value was obtained. These results are plotted in Figure 5.2, for the static case and for a situation similar to the forward flight cruise scenario, with a free stream velocity of 22.3 m/s, which was also the highest airspeed tested. From these results, as expected, the overall thrust decreases as the airspeed increases, which becomes a limitation to the proper

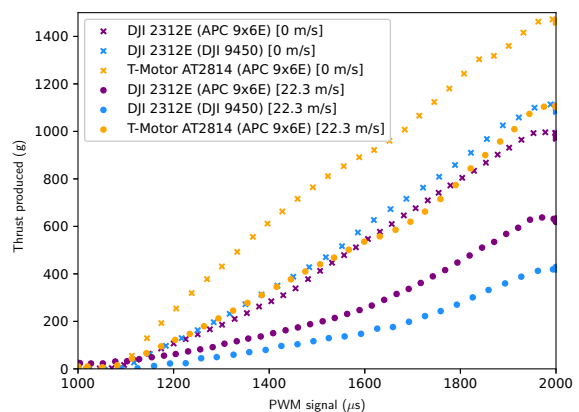


Figure 5.2: PWM-Thrust map.

estimation of the thrust produced from the PWM value. Another factor to consider is the effect of the battery voltage drop on the motor speed and consequently on the propeller thrust, which was not taken into account in this case. To account for that, a 3D mapping with the battery voltage as a third variable can be made.

Table 5.1 presents results relating to the power consumption, efficiency, and voltage conditions at maximum throttle during the propulsive tests. Note that the error presented is the standard deviation of the measurements taken during the maximum throttle interval. First, compared to the eCalc predictions from Section 3.3.5, the prediction for the DJI motor and propeller combination was very accurate, within the margin of error of the experimental measurement ($261.4 \text{ W} \pm 39.21$ vs $260.7 \text{ W} \pm 1.00$). On the other hand, both combinations using the APC 9x6E propeller show that the eCalc prediction underestimates power consumption with an error of 6.27% and 14.80% for the DJI and T-Motor motors, respectively, which is still within the 15% margin of error claimed by the tool [57]. In dynamic tests at 22.3 m/s, all configurations show a decrease in electrical power, with the DJI 9450 propeller showing the greatest power decrease, because the lower pitch of this propeller means that at higher speeds, where the effective angle of attack of the propeller is lower, the torque produced by the propeller is lower.

Table 5.1: Power and efficiency (at maximum throttle) experimental results.

Propeller Motor	Flight Condition	APC 9x6E		DJI 9450
		DJI 2312E	T-Motor AT2814	DJI 2312E
Electrical power (W)	Static	277.3 ± 1.23	451.9 ± 0.57	260.7 ± 1.00
	22.3 m/s	263.4 ± 1.45	440.9 ± 0.97	187.5 ± 0.34
Voltage drop (V)	Static	1.54 ± 0.01	2.98 ± 0.004	1.68 ± 0.01
	22.3 m/s	1.43 ± 0.01	2.96 ± 0.01	1.33 ± 0.004
Motor + ESC efficiency (%)	Static	66.38 ± 0.33	80.00 ± 0.06	69.43 ± 0.29
	22.3 m/s	71.30 ± 0.23	80.20 ± 0.14	79.30 ± 0.32
Total efficiency (g/W)	Static	3.53 ± 0.01	3.24 ± 0.01	4.20 ± 0.02
	22.3 m/s	2.58 ± 0.01	2.67 ± 0.003	1.30 ± 0.02

Regarding the electric efficiency, which comes from the efficiency of both the motor and ESC the T-Motor AT2814 clearly presents a higher efficiency. This is because while the DJI 2312E motor in both configurations operates close to its maximum power of 280 W, the T-Motor motor is operating much further from its maximum of 700 W. It is also worth mentioning that, as verified, all configurations are within the power limits of both motors. Moreover, note that the electrical efficiency is obtained from the ratio of mechanical power output (torque multiplied by the angular velocity) to electrical power consumption.

When looking at the total efficiency of the system, which is the ratio of thrust produced per unit of electrical power consumed, the DJI propeller combination actually proves to be the most efficient in static conditions, which would be found in hovering flight, as once again the lower pitch of the propeller means that the torque on the motor will be lower. On the other hand, in cruise conditions, this combination decreases in efficiency significantly, while the two others decrease, but not as significantly. As such, the DJI motor and APC propeller combination shows the best trade-off in efficiency for both modes.

Lastly, an abnormal voltage drop was observed at the ESC terminals. As a comparison point, the

chosen configuration, powered with a fully charged Gensace Soaring battery in a static test showed a voltage drop of only $0.66 \text{ V} \pm 0.03$, while the same configuration powered by this power supply shows a voltage drop of 1.54 V . Likely, this was caused by the long cable used to connect the power supply to the ESC, which introduced resistance to the connection. This increased voltage drop consequently leads to a lower motor speed and thrust.

Putting the results from all tests together, the change in thrust produced with airspeed is presented in Figure 5.3, where the experimental results are compared with eCalc predictions from Section 3.3.5. Note that the band around the eCalc data corresponds to the 15% margin of error previously mentioned. Although the load cells were tared before each test to ensure that the drag from the structure did not affect the measurement, an offset could be created as the propeller was rotating during taring. As such, for dynamic tests, the thrust is considered as the difference from the mean measurement during the period where the throttle command was zero. Finally, although small, the uncertainties presented correspond to the standard deviation of the measurements taken.

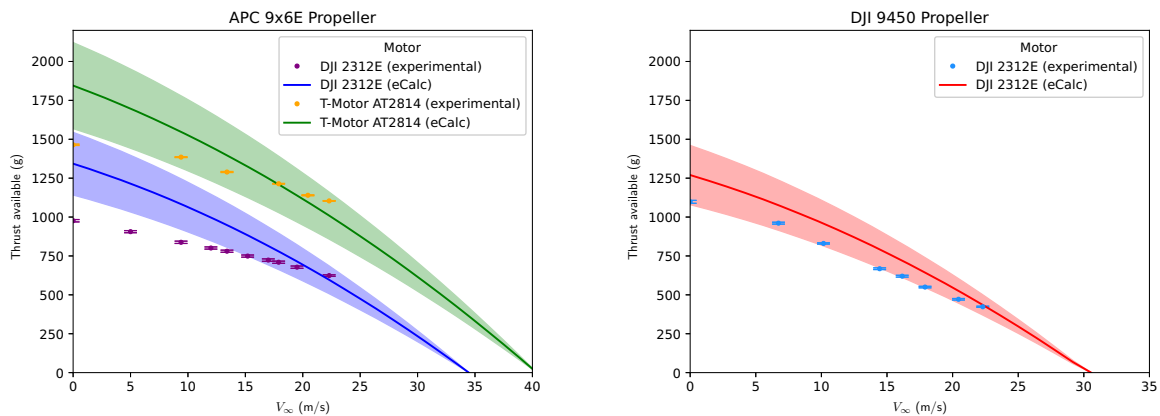


Figure 5.3: Dynamic thrust experimental results.

The first point worth mentioning is that a consistent overestimation of thrust is observed when comparing the eCalc data with the experimental results, likely due to the high voltage drop that was previously observed. This difference is more pronounced at lower airspeeds, as the increase in airspeed reduces the torque demanded to the motor.

Regarding the propeller choice, the DJI motor and propeller configuration, unlike the eCalc prediction, produces more static thrust than the DJI motor with the APC propeller, however, as the airspeed increases, the latter clearly produces more thrust than the DJI motor and propeller. Overall, the higher pitch APC propeller's thrust decreases slower (and even more slowly than predicted by eCalc) with the airspeed than the lower pitch DJI propeller. Once again, as previously observed, the eCalc prediction for the DJI propeller is much closer to the experimental results than for the APC propeller. According to these tests, the Full, Ground, Tailsitter and Quadcopter configurations will present a thrust-to-weight ratio of 1.642 ± 0.003 , 1.733 ± 0.003 , 2.333 ± 0.005 and 2.523 ± 0.005 , respectively, in hover conditions. These results further support the design choice made in Section 3.3.

5.2 Wind tunnel

As one of the key advantages of a trimodal vehicle like the one described in this work is its ability to operate more efficiently (compared to hovering), it is important to address the most relevant source of energy loss in aerial modes, which is aerodynamic drag. To quantify its impact, wind tunnel tests were performed, simulating the conditions experienced in hover and forward flight. In addition, given the unconventional design used, wind tunnel testing was used for validation of the design, before any flight tests. In particular, it is important to assess whether the additional drag of the components required for locomotion on the ground and forward flight is justified by the efficiency obtained in each of these modes.

5.2.1 Wind tunnel setup

The wind tunnel tests were performed in the Portuguese Air Force Academy (AFA) wind tunnel, characterised in [100]. It has a working section of 0.8 m by 1.3 m, which is enough to fit the whole vehicle. Its maximum speed is 70 m/s, which also covers the flight envelope of the UAV. During the tests, it was noted that resonance in the structure occurs at around 25 m/s. The model being tested is assembled in the middle of the test section, as seen in figure 5.4. This is where the balance is located, which measures forces and moments acting on the model. The section where the model is placed is open.

To control the speed of the airflow in the tunnel, a knob is used, with an indicator for the airspeed. This indicated value however has an error relative to the true airspeed that flows in the work section. Other measurements were available, including a differential pressure sensor at a given section in the tunnel, a pitot tube placed at the exit of the tunnel, and the pitot tube used in the vehicle (whose measurement turned out to be inaccurate, as discussed in Section 3.2). After analysing the flow with a portable anemometer, the differential pressure sensor was concluded to be the most accurate measurement. With comparative measurements from each source, a second-degree polynomial fit was made from the indicated airspeed in the control panel and from the pitot tube at the exit, to the true airspeed which should be considered for the experimental results. In tests where either of the two was used as a reference, the polynomial fit was used to obtain the true airspeed. Whenever a differential pressure was available, that was used to calculate the true airspeed. A weather station was present in the wind tunnel building, which was used to calculate the dry air density, using the measured temperature and ambient pressure.

To attach the model to the balance, a movable arm and a flat plate are available, as presented in Figure 5.4. Using the movable arm, the model is mounted near the centre of the working section, whereas with the flat plate, the model is mounted at the bottom. Both options allow for control of the side-slip angle, in the range of -90° to 90° , however, only the movable arm allows for control of the angle of attack, in the range of -30° to 30° .

For tests in hover conditions, the movable arm was used. To attach it to the arm, a 3D printed part was used, which held the UAV by the four quadcopter frame arms. In this configuration, the CG is fixed, and only the wheels (and propellers, when present) are free to rotate. Due to the limited range of motion of the arm, however, the fixed-wing mode tests were performed with the UAV fixed to the flat plate by its wheels. In this setup, the angle of attack of the wings is controlled as it would be in forward flight, with



(a) Movable arm.

(b) Flat plate.

Figure 5.4: Wind tunnel mounting.

the attitude controller running on the vehicle, and with the propellers providing differential thrust. When measuring the drag in forward flight conditions, the propellers were removed, and a level attitude was considered.

The balance used can provide measurements of the forces in three axes, and moments about three axes. Each measurement is by default considered by the software as an average of a series of measurements and is thus accompanied by a standard deviation.

Depending on the type of test being performed, either the angle of attack or the airspeed was varied throughout the test. When varying the angle of attack, with the movable arm, an automatic test program was used, which varied the angle from 10° to -30° , taking a sample at intervals of 1° . With the flat plate, the angle of attack was varied from 0° to 20° , using a Python script running in the MissionPlanner ground station, which changed the pitch angle target in intervals of 1° . Then, the true angle of attack was considered by looking at the logs from the flight controller and checking what angle the vehicle was able to achieve. In both scenarios, the forces resulting from the support and not the vehicle were removed, by running a test in the same conditions only with the support.

In the hover attitude, all tests were done at a fixed velocity of 20.80 m/s with the angle of attack being changed by the arm, except for the assessment of the crosswind drag, where the attitude of the UAV was fixed, and the airspeed was varied, and the measurement of the side force produced by the E396 aerofoil, which was taken in a hover attitude in the flat plate, with no flow from the wind tunnel. Apart from this last test, all other tests were conducted with the E169 wing fitted. For the forward flight attitude, tests were done with both the E169 and E396 aerofoils, at speeds of 12.91 m/s and 17.67 m/s.

5.2.2 Aerodynamic performance

Hover

From the tests performed in the hover attitude, the aerodynamic drag of the airframe can be estimated. These results already have the drag from the arm and support removed, a task which was done by the

balance software. Note that when thrust is present, the drag measured at angles different from 0° also has a component from the thrust in the direction of the airflow, which changes depending on the angle. For that reason, the tests were done without the propellers rotating. From these results, as the vehicle pitches down, as it would in hovering flight to move forward, an increase in drag is observed in all configurations, as the wetted area of the frame increases.

Disregarding the interactions between different removable components, the contribution to the drag coefficient of each vehicle component (considering the total wing area as a common reference area) can be obtained, as presented in Table 5.2.

Table 5.2: Experimental hover forward drag coefficient contributions and totals.

Component / Configuration	Level hover $C_D (0^\circ)$	Forward hover $C_D (-30^\circ)$	Mean $C_D (10^\circ, -30^\circ)$
Quadcopter frame	0.297 ± 0.001	0.331 ± 0.002	0.308 ± 0.010
Wheels	-	-	0.193 ± 0.003
Wings	0.546 ± 0.017	0.647 ± 0.005	0.573 ± 0.061
Quadcopter	0.297 ± 0.001	0.331 ± 0.002	0.308 ± 0.010
Ground	0.490 ± 0.002	0.522 ± 0.002	0.501 ± 0.009
Full	1.037 ± 0.017	1.169 ± 0.004	1.074 ± 0.068

The wheel drag was considered independent of the angle of attack, as the area exposed to the flow is always the same, regardless of the angle. As expected, the addition of wheels and wings represents an increase in vehicle drag. The most significant increase in this case comes from the wings, which in a hover attitude are placed perpendicular to the flow, thus presenting as a vertical wall. Still, the wheels contribute significantly to the forward drag, despite their thin profile, a fact that can likely be explained by the interior mesh present in the wheels, whose aerodynamic effect is not clear. In fact, during the wind tunnel tests the wheels were observed to spin at certain angles of attack and with other objects in their vicinity (such as the wings)¹. From the observations made during the tests, it looks like the airflow hitting the wings is redirected to the sides, towards the mesh of the wheels.

Comparing the drag coefficient of the complete vehicle with values available in [101], although the drag of the vehicle is much higher than that of a fixed-wing aircraft, it is still within the range of what would be expected for a hovering helicopter, which was the most similar to this use case.

Assuming that the drag coefficient in hover does not depend on the airspeed and considering the maximum pitch angle of 30° , the minimum thrust required for flight at a constant speed at that pitch angle was estimated. Considering the known required thrust for hover at the maximum pitch angle, when the thrust required for hover at a given speed is equal to it, it indicates the maximum achievable speed while maintaining altitude. Using the same maximum lean angle in ground operation means that these results apply to it as well. It is worth noting however that this is only a rough estimate, given the assumptions made. Furthermore, considering the propulsive tests of the chosen propulsive system at a speed of 5 m/s (note that this is the component of the airspeed perpendicular to the propeller), with the required thrust an estimate of the power consumption at the maximum speed can be obtained, as well as the energy

¹This phenomenon can be observed in the video present at: <https://youtu.be/bLnQPr-VixY>.

consumption. These results are presented in Table 5.3.

Table 5.3: Estimated energy consumption at the maximum speed in hovering flight.

Configuration	Max. speed (m/s)	Power consumed (W)	Energy consumption (Wh/km)
Quadcopter	16.19	430.3	7.38
Ground	15.55	740.5	13.23
Full	10.68	787.3	20.48
Full (with lift)	9.66	610	17.54

It is crucial to bear in mind that these results do not account for the fact that the wings, present in the Full configuration, also generate lift. This effect reduces the required thrust for forward hovering, and the real maximum speed of the Full configuration is therefore lower, but the power consumption is lower too. This begs the question of whether the addition of wings can increase the efficiency in hovering flight. Figure 5.5 shows the lift and drag contribution from the wings, while in hovering flight. It is clear that lift increases as the angle of attack of the wings decreases, but simultaneously, the drag increases too. This is because in a level hover, most of the drag comes from the wing that faces the flow, but as the aircraft pitches down, the rear wing becomes exposed too. However, at a given point, the drag of the wings starts to decrease, as the flow is able to attach to the wings, while the lift continues to increase. Due to the 30° limit on the movable arm, no tests were carried out at 40°, however, given the tendencies observed, it is likely that if the aircraft pitches further down, there will be a point where the lift will equal the drag. Now taking the lift produced by the wings into account (as a reduction in the thrust required for hover), an energy consumption of 17.54 Wh/km was estimated, higher than even the Ground configuration.

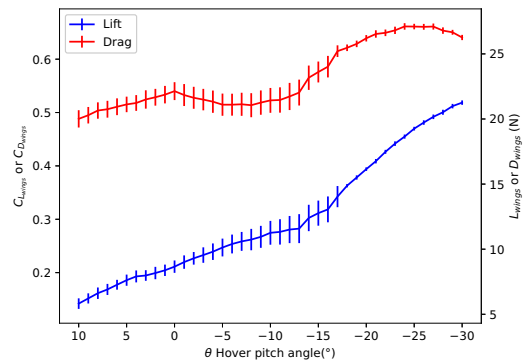
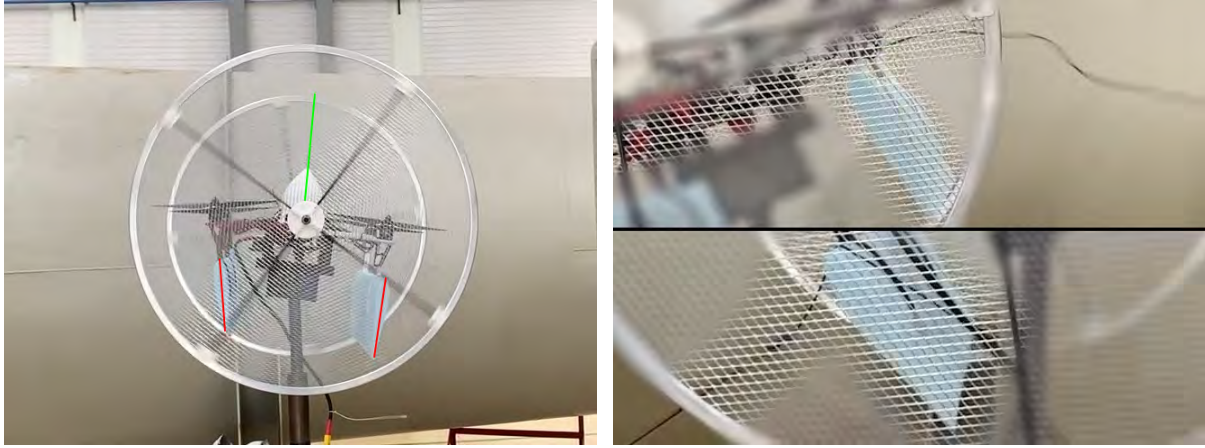


Figure 5.5: Wing performance in hover at 20.80 m/s.

In Figure 5.5, it is clear that until a given angle of attack, high uncertainty is present, which then disappears. This was caused by shaking of the wings (mainly the rear one, as it experiences turbulent flow), which was observed during the tests². Unexpectedly, a positive lift coefficient is observed throughout the entire range of pitch angles, as due to the strong drag force on the front wing, bending of the frame was observed (see Figure 5.6(a)), which caused the angle of attack of the front wing to be further reduced. Lastly, although the airflow over the wings at these angles of attack is stalled, the flow observed over the front wing was partially attached, as seen in Figure 5.6(b).

To quantify the effect of crosswind on the vehicle, tests were conducted at different speeds (6, 8, 10 and 12 m/s) with airflow impacting the UAV from the side. Table 5.4 shows the results from these tests, which show that a significant impact is observed in the lateral drag due to the presence of the wheels. Because of this, lateral movement (using roll) while hovering would be significantly more inefficient and

²Shown in the video present at: <https://youtu.be/DSFuCYjg9q8>.



(a) Frame deformation (chord lines indicated in red, and frame vertical in green). (b) Flow over front (bottom) and rear (top) wings @ $\alpha = 60^\circ$.

Figure 5.6: Hover 20.80 m/s test.

Table 5.4: Experimental lateral drag coefficient.

Configuration	Quadcopter	Tailsitter	Full
C_D	0.156 ± 0.004	0.216 ± 0.008	1.742 ± 0.030

the vehicle will be considerably perturbed by crosswind.

Finally, the lateral force produced by non-symmetrical aerofoil E396 in hover due to the propeller flow was estimated at $1.546 \text{ N} \pm 0.126$, which compared to the drag forces the vehicle experiences while hovering is much smaller. As such, the fact that this aerofoil produces lift during stationary hover should not affect the vehicle's stability.

Forward flight

First, using the flat plate on the wind tunnel, the Full vehicle configuration with the E169 wings was tested with no propellers attached. In this case, the pitch angle was the equilibrium point in which the pitching moment is null (0°). By running this test at different speeds, and assuming the C_D of the vehicle is independent of the velocity, a drag coefficient was obtained for the forward flight attitude, in the Full configuration of 0.383 ± 0.048 . Now subtracting the drag induced by the wheels, whose contribution should be the same in hover and forward flight, a drag coefficient of 0.19 ± 0.05 is obtained for the Tailsitter configuration, which is the other possible configuration for fixed-wing flight. Once again, compared with [101], these values are high for a fixed-wing aircraft, as the frame was not designed for forward flight. This coefficient could also be reduced if a larger wing span was used.

As previously done for the hover scenario, assuming that the drag coefficient of the vehicle does not change as the speed changes, an estimate can be obtained for the drag acting on the vehicle at a given speed. Furthermore, assuming a cruise angle of attack of 16° , the thrust required for each motor to maintain constant speed can be calculated. With this, using the propulsion tests data (choosing for each speed, the test done at the closest airspeed), an estimate for the power consumed and the energy consumption can be obtained, as presented in Figure 5.7.

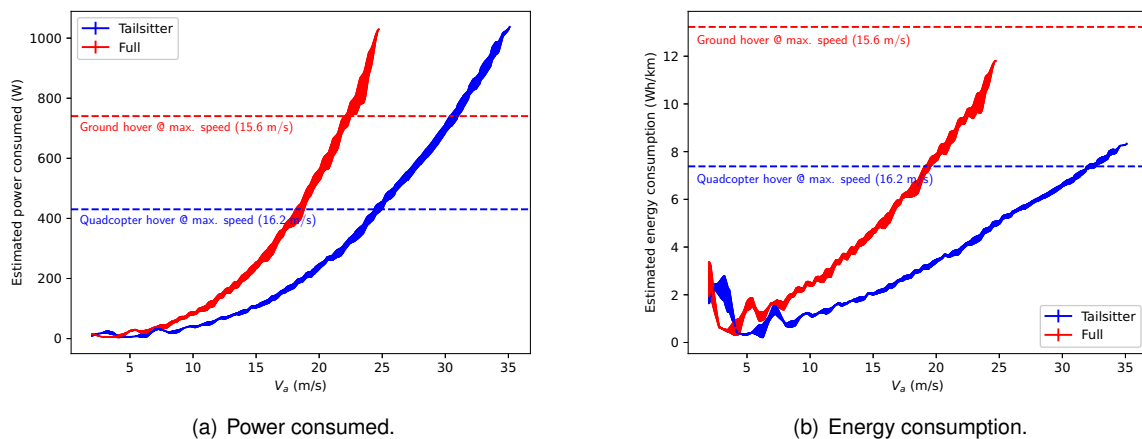


Figure 5.7: E169 forward flight performance estimate.

This result is only an assumption, with two particular caveats that should be taken into account. First, as the drag was estimated with no propellers, in real flight, the drag estimate would be slightly higher due to the drag induced by the propellers. Moreover, propulsion tests were only performed up to a speed of 25 m/s, therefore the results for speeds above that use this as the estimate for the thrust. As observed in Section 5.1.2, the power consumed per gram of thrust produced increases as the airspeed increases, and thus our estimate above 25 m/s for the consumed power and energy is underestimated. The apparent noise in the estimates originates from the uncertainties in all the associated measurements.

Nonetheless, comparing the forward flight results with those previously obtained for hovering flight in the Quadcopter configuration, not only does the UAV operate more efficiently in forward flight, but it can also operate at much higher top speeds. At the same speeds, the fixed-wing operation is estimated to consume 3.02 and 2.58 times less power for the Tailsitter and Full configurations respectively, when compared to their wingless counterparts in hover. Moreover, these configurations are estimated to achieve a maximum speed that is 2.17 and 1.59 times faster, respectively.

Finally, using the data from the tests in forward flight attitude with a varying angle of attack, the lift produced by the wings in these conditions is presented in Figure 5.8, in terms of lift coefficient and force.

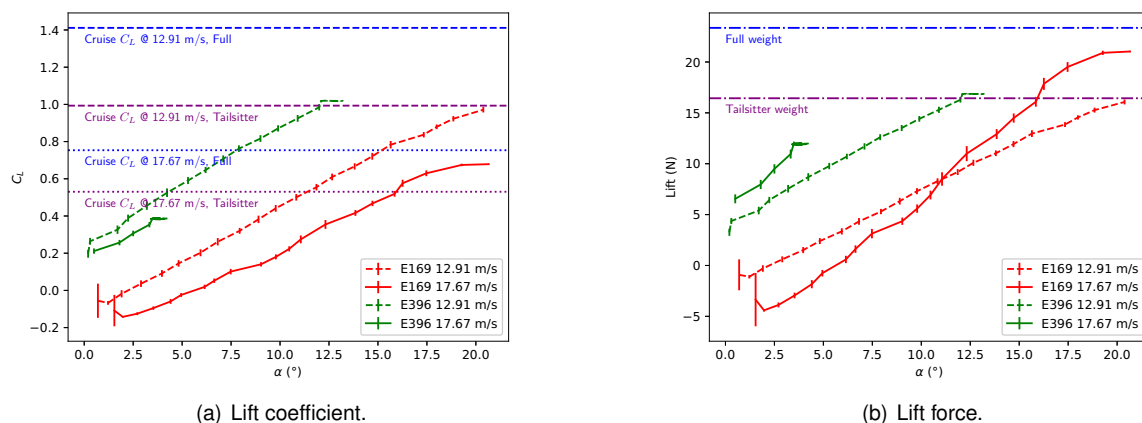


Figure 5.8: Lift in forward-flight conditions.

First, as previously predicted, the non-symmetric aerofoil appears to show an increased pitching moment, as during the tests, at neither of the speeds tested, it was able to reach the desired angle of attack, as the motors could not provide enough differential thrust. Secondly, at both speeds, neither of the aerofoils is able to provide enough lift to maintain level flight in the Full configuration. At a higher speed of 17.67 m/s, only the E169 profile can sustain level flight, in the Tailsitter configuration, as the E396 wing could not achieve an angle of attack greater than 5° . In fact, at the speeds tested, level and climbing flight is only possible with the Tailsitter configuration, with the E169 wing, and at 17.67 m/s. These results confirm the design choice from Section 3.2. In both wings, the lift coefficient decreases as the airspeed increases. It is important to mention that although these results are considered as the wing lift, at angles different from zero, as the motors were used to control the pitch of the vehicle, a component of the measured lifting force is caused by the thrust. In a real scenario, to achieve flight this net lifting force is what is experienced, and so these results are considered relevant.

These tests validated that forward flight is possible in the Tailsitter configuration at these speeds, thus that will be the configuration tested in forward flight tests. Despite this, flying in the Full configuration can be possible at higher speeds.

5.3 Operational tests

Lastly, the vehicle was tested in real-world conditions in all modes of locomotion. The goals of these tests were to validate the design of the vehicle, debug the developed code, evaluate the vehicle's potential efficiency gains, and prove its viability and versatility in multimodal operation.

With these goals in mind, the UAV was tested for a total of 10 hours of flight/drive time, according to the autopilot logs. The tests first took place in the development stage, namely to validate structural changes and debug the implementation of the ground modes. With that stage concluded, the aircraft was tested at Aeroclube da Lourinhã³, at different places at IST, and at Centro de Experimentação Operacional da Marinha (CEOM) of the Portuguese Navy, a facility made for experimentation and where the largest unmanned systems experimentation exercise in the world (REPMUS) takes place. Most of the final flight tests were performed on the same day, when calm wind was observed (under 2 m/s). The other tests were done on different days, when stronger winds were experienced (5 m/s and above).

The attitude controller gains were tuned in the Quadcopter configuration, according to pilot feedback. Extensive tuning [102] was not pursued, as it goes beyond the scope of this work. For all the other controllers, the default gains were used. Initially, the tuning process used QAUTOTUNE, however unsatisfactory results were obtained.

The data used to obtain the presented results was extracted from the flight controller logs. All readings were used directly, except for the measured battery current, which had to be filtered due to this measurement being riddled with noise. To filter the battery current, only the relative maximums of the signal were considered, which were then passed through a low-pass filter.

³Aeroclube da Lourinhã's location: <https://maps.app.goo.gl/fyYFqC2Ws5KX6jgG8>.

5.3.1 Hovering flight

In hovering flight, the vehicle was tested in all possible configurations such that their impact can be observed in the base hovering flight mode. In addition, the Tailsitter configuration was tested both with the chosen E169 symmetrical aerofoil, as well as with the E396 cambered aerofoil, to assess its impact on hovering stability. Figure 5.9 shows the tested configurations in-flight.



Figure 5.9: Different flight configurations in hove flight.

In the Quadcopter and Tailsitter configurations, the aircraft was flown for as long as possible on a single battery, while flights in the other configurations were shorter in length, due to safety concerns with the stability of the UAV. To the extent possible, the drone was flown both against and in favour of the wind, as well as perpendicular to it⁴, so that its impact on the measurements taken would be minimised. Because in the hovering attitude the pitot tube is completely misaligned with the incoming flow of air (with respect to the vehicle), no reliable airspeed measurement is available, and therefore, in all hover (and for the same reason, ground) tests, when speed is mentioned, the ground speed, as measured by the GNSS receiver is used.

For the controller analysis, only a 60 second (or as close as possible) segment of the flight is considered, in QHOVER mode, as presented in Figure 5.10. Additionally, for the same segment, in Table 5.5, the Root Means Square Error (RMSE) and Mean Absolute Error (MAE) are shown for each axes' angle controller, as well as the control effort for each axes' rate controller. The control effort is defined as the integration of the absolute controller output, which, since different length segments are compared, is then normalised to the length of the interval considered.

Analysing the results obtained for the pitch axis, a good tracking of the desired inputs is observed overall. With the same gains, a similar response is seen for all configurations, meaning that the pitch axis control is largely unaffected by the addition of wheels and wings. Moreover, the stability in the pitch axis appears to be largely unaffected by the non-symmetrical aerofoil.

On the other hand, the performance in the roll axis appears to be significantly affected by the presence of the wheels, as the inertia of the vehicle is more distant from the CG. In fact, when the wheels are present, oscillations are observed in the roll axis.

Finally, the tuning obtained in the yaw axis was not as good as in the other two axes, but still, for the wheel-less configurations it produced satisfactory results. When the wheels were added, however, once again due to the shift of the vehicle inertia, oscillations were observed. To contribute to this fact,

⁴Video of the Quadcopter and Tailsitter configurations available at: https://youtu.be/JcS1_F6t17w.

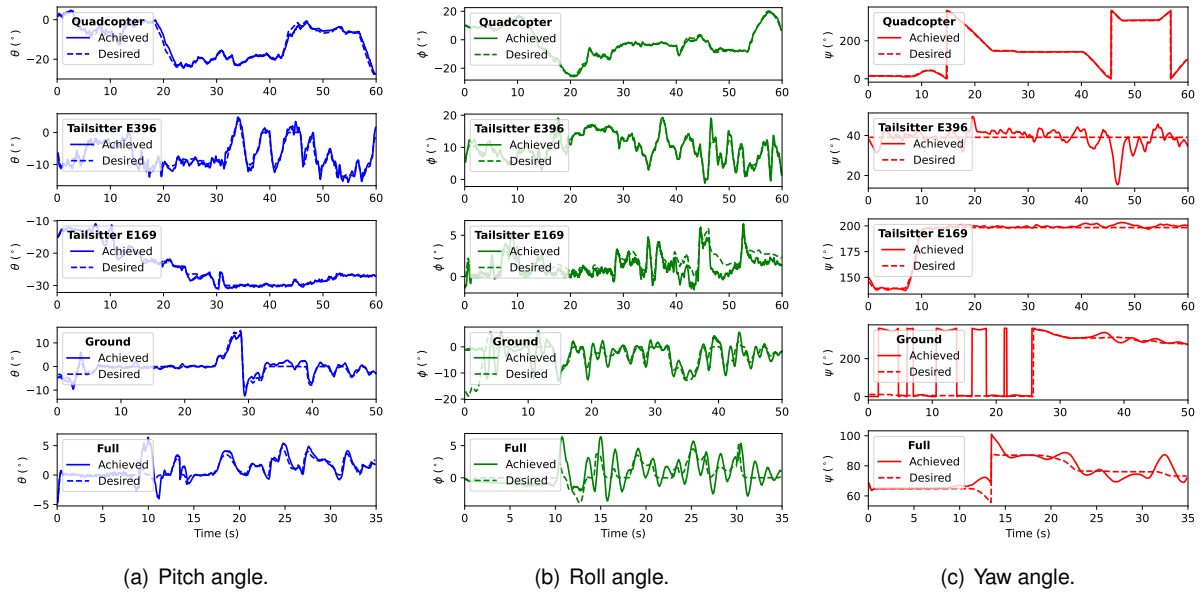


Figure 5.10: Attitude controller performance.

Table 5.5: Hover attitude controller metrics.

Axis	Configuration	Quadcopter	Tailsitter E396	Tailsitter E169	Ground	Full
Pitch	RMSE	1.29	1.10	0.57	1.09	1.12
	MAE	0.92	0.88	0.42	0.84	0.59
	Control effort	0.069	0.070	0.077	0.041	0.038
Roll	RMSE	0.90	1.01	0.90	4.34	1.55
	MAE	0.69	0.66	0.71	2.61	1.23
	Control effort	0.034	0.044	0.021	0.083	0.036
Yaw	RMSE	7.31	4.57	1.98	14.76	4.48
	MAE	2.30	3.09	1.56	8.02	2.86
	Control effort	0.132	0.221	0.195	0.115	0.102

throughout the different testing stages, several times issues with the compass measurements were encountered. This was in part due to the metal present in the wheels surrounding the avionics, and due to current flowing through wires below the compass. This issue was partly resolved with a simple calibration of the compass with flight logs. Lastly, it is clear that the yaw axis demanded the most control effort overall, once again, due to the weaker tuning achieved⁵.

Better responses could have been obtained if different and appropriate gains had been used for different configurations. Still, considering that achieving an optimal tune is not a quick task [102] and is out of the scope of this work, the results obtained are sufficient to prove the concept of the vehicle.

Regarding the effect the wind has on the stability of the vehicle, it was clear that both the wings and wheels make the vehicle more susceptible to wind disturbances. Still, even with the E396 aerofoil which was flown in windy conditions⁶, the vehicle was able to maintain a stable attitude.

⁵Video of the Ground and Full configurations, where both roll and yaw oscillations are visible, available at: <https://youtu.be/qY0zMYQmxDI>.

⁶Video of the Tailsitter E396 in flight available at: <https://youtu.be/rKFx7GFzZQc>.

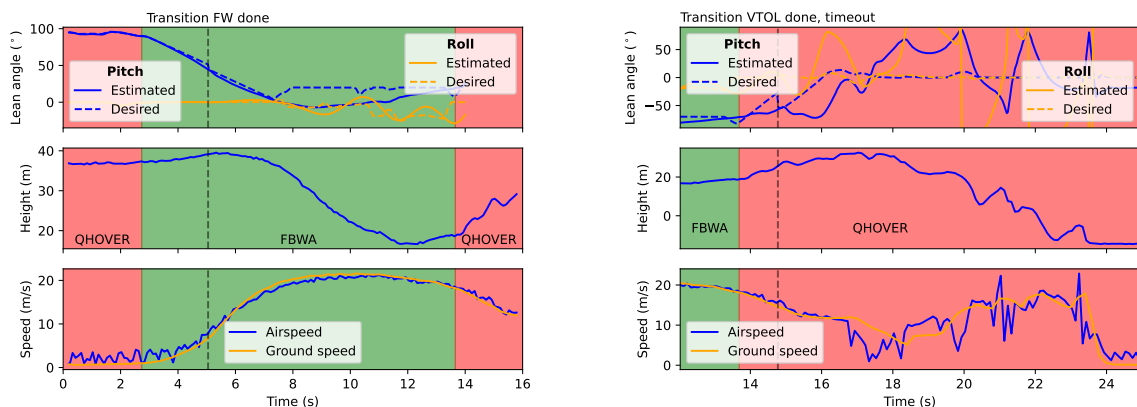
5.3.2 Forward flight & transition

To test the UAV in forward flight mode, the transition had to also be tested. Unlike other types of VTOL aircraft, where both modes can be tested separately and once both are safe to fly in, the transition can be tested, in a tailsitter VTOL aircraft as this one, fixed-wing flight can only be achieved by transitioning to it in the air, and then back to a VTOL mode for landing. For safety reasons, this flight was performed at a higher height above the ground and over soft grass. Even though the wind was calm, the transition was done against the wind, as would be done for a conventional fixed-wing aircraft take-off. Figure 5.11 shows the vehicle flying in forward flight⁷.



Figure 5.11: UAV in forward flight.

Figures 5.12 and 5.13 show how the aircraft performed in both transitions and the behaviour of the pitch rate controller. The messages on the top indicate the ArduPilot output to the GCS, indicating when control is handed over to fixed-wing/VTOL controllers.



(a) Hover → Fixed-Wing transition (Pitch in forward flight frame of reference).

(b) Fixed-Wing → Hover transition (Pitch in hover frame of reference).

Figure 5.12: Transition analysis.

To initiate the transition, the control mode was switched from QHOVER to FBWA. After that, the vehicle was able to successfully pitch down, at the desired rate, all the way to zero, as previously described

⁷Video of the UAV in forward flight is available at: <https://youtu.be/dgemtPbkP04>.

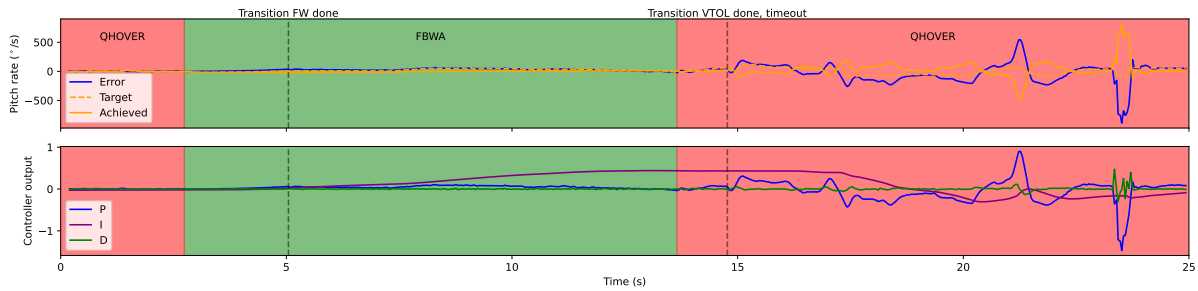


Figure 5.13: Pitch rate controller during both transitions.

in Section 4.4. Once control was given back to the pilot, the pilot immediately attempted to pitch up, as the vehicle was simultaneously losing altitude. At this point, the vehicle has accelerated to about 20 m/s, and the aerodynamic forces acting on the vehicle are much stronger. For this reason, the attitude controller was unable to provide a quick response and the vehicle took approximately 6 seconds to reach the desired pitch requested by the pilot. By this point, the vehicle was already regaining altitude, and maintaining aerodynamic flight, sustained by its wings.

During the time it took for the slow response to catch up, however, the rate controller built up a significant integrative term and saturated its integrator. Simultaneously, a slow oscillation on the roll axis is observed (recall that in forward flight, the roll rate is controlled by the yaw rate controller for hover flight), likely caused by the tuning of the yaw rate controller. Even though the UAV was already recovering altitude, because it was already too low, and getting far away, the pilot decided to transition back to hover flight by switching to QHOVER mode. Still at a high speed, the vehicle was unable to keep up with the requested pitch-up rate, the transition timed out and control was forced back to the hover controller. As the vehicle slows down, the motors are able to pitch up the vehicle, but with the integrator still saturated, a strong actuation was provided and the UAV completely overshoots the level flight attitude. Combining that with the amplitude-increasing oscillations in the roll angle, the vehicle enters an uncontrollable state. The flight ended with a hard landing on the grass⁸.

Table 5.6 shows the controller metrics during the portion of the FBWA control mode, where it is clear that the controller whose tuning most affected the flight was the pitch controller. Note that the angular error measurements are relative to the forward flight angles, while the control effort is obtained from the rate controllers, which are executed in the hover frame of reference.

Table 5.6: Forward flight attitude controller metrics.

Axis	RMSE	MAE	Control effort
Pitch	198.24	10.71	0.255
Roll	55.30	4.74	0.0254
Yaw	-	-	0.0722

To improve the performance in forward flight, unlike the approach followed by ArduPilot, different gains should be used for the forward flight mode of this type of tailsitter aircraft. As the much increased aerodynamic forces change the dynamics of the vehicle, even though the actuators are the same, the response is significantly changed, thus a different set of gains is needed. Moreover, the integrative term on the rate controllers should be reset upon a mode switch, so that the saturation is not carried over to

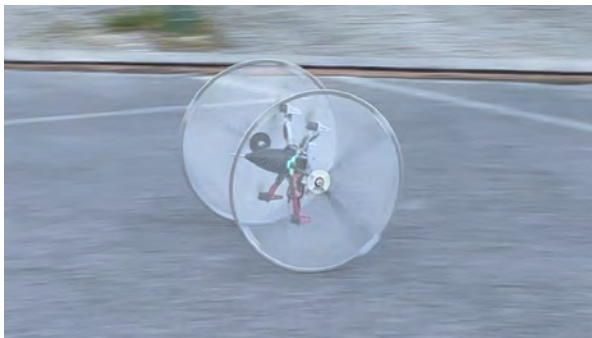
⁸An animation of this flight is available at: <https://youtu.be/mKGV9woDMro>.

the next mode. Additionally, as the vehicle cannot decelerate as fast as it can accelerate, for the transition to hover mode, a slower pitch rate should be used so that the vehicle can better keep up with it and properly decelerate. Although not crucial to the outcome of the flight, the trim cruise pitch angle should also have been set (default value is zero), so that the aircraft would try to maintain the cruise pitch angle without corrective pilot input.

As previously mentioned, the CG of the vehicle is placed too far forward with respect to the wings, thus making the pitch-up manoeuvre harder to achieve. Still, forward flight was achieved, and results could be obtained regarding the energy efficiency of the vehicle.

5.3.3 Ground locomotion

As most of the code development was done to implement the ground modes, these were the most extensively tested. Both the Ground and Full configurations were tested, however, it became clear that the wings altered the longitudinal dynamics of the vehicle in windy conditions, so the results presented were obtained in the Ground configuration only. For all results except for the performance in AUTO mode, the RMANUAL mode was used.



(a) Ground configuration, $\theta_{max} = 80^\circ$.



(b) Full configuration, $\theta_{max} = 30^\circ$.

Figure 5.14: Robot in ground locomotion tests.

The first point to address is the fact that, at least on flat horizontal surfaces, there is no need to support any of the weight of the vehicle with a thrust force. Thus, in an ideal scenario, all the thrust produced by the propellers would contribute to vehicle locomotion, meaning that the robot would operate with a pitch angle of 90° , unlike the maximum used in hover of 30° .

First, the vehicle was tested in static conditions to determine the minimum power required to maintain a given pitch angle. This test revealed that almost the same power is required to maintain any pitch angle until 50° . From that point on, until the maximum of 80° ⁹, the power required increases. The robot was then tested over a 40m stretch, in back and forth segments, to determine the most efficient pitch angle setting, as shown in Table 5.7. Using $\theta_{max} = 50^\circ$ proved to be the most efficient. Note that the power measurement has a very high uncertainty because the power module is not designed to measure currents this low.

⁹Video of the test with $\theta_{max} = 80^\circ$ is available at: <https://youtu.be/JW0CDfEj8MQ>.

Table 5.7: Ground θ_{max} comparison.

θ_{max} ($^{\circ}$)	30	50	80
Maximum speed (m/s)	3.73 ± 0.12	5.01 ± 0.27	7.69 ± 0.49
Power (W) [before filtering]	63.4 ± 4.7	64.7 ± 22.6	135.8 ± 32.4
Energy consumption (Wh/km)	5.07 ± 0.07	3.48 ± 0.14	4.06 ± 0.04

From the same tests, and an additional test performed at a different location where there was no lateral inclination, the results in Figure 5.15 were obtained.

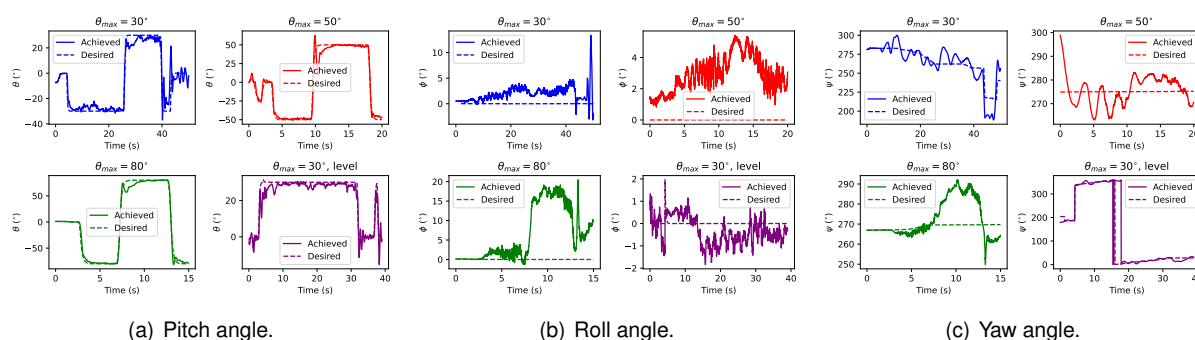


Figure 5.15: Ground attitude controller performance.

These results show that the pitch target is adequately tracked, supporting the assumption that any friction from the wheel bearings can be neglected. Even when a maximum pitch of -80° was used, a good response was observed. When the robot brakes, which requires changing the pitch angle from its current value to its symmetric (for maximum braking force), a quick response is observed, with slight oscillations initially that quickly fade away, not being significant to the performance of the vehicle. On the roll axis, the discrepancy observed relative to the fixed target of zero was caused by the test surface having a lateral inclination. Ideally, the target would be set to the surface inclination value.

Table 5.8: Ground attitude controller metrics ($\theta_{max} = 50^{\circ}$).

Axis	RMSE	MAE	Control effort
Pitch	39.03	3.38	0.111
Roll	9.93	2.95	0.084
Yaw	41.23	5.24	0.063

In the yaw axis, as previously observed, oscillations are present. One key observation however is that by using a higher pitch angle, these oscillations decrease in intensity. This is caused by yaw being controlled more by differential thrust than motor torque as the pitch angle increases, and by the vehicle being more stable at higher speeds.

From Table 5.8 it is clear that the pitch axis requires the most control effort, as expected, due to it being the main pathway to make the vehicle move in a given direction. At this angle, roll and yaw are almost equally controlled by body frame roll and yaw, hence the high control effort on the roll rate and yaw rate controllers.

The ground AUTO mode was tested in the CEOM facilities, with 6 consecutive target waypoints being given¹⁰. The terrain here is made of both gravel and asphalt. Figure 5.16 shows the covered track

¹⁰Video of the robot completing this waypoint mission is available at: <https://youtu.be/Khr2rDbhbSY>.

and position controller performance during this test. Note that for the velocity and position, the desired value corresponds to the input given from the mission, while the target is the value used by the position controller after adding the desired velocity.

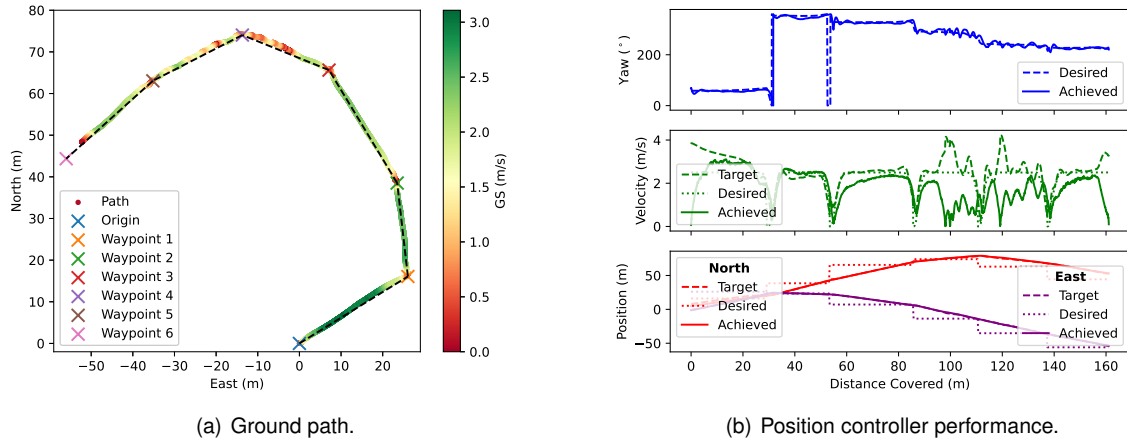


Figure 5.16: Ground AUTO mode waypoint test.

The first conclusion to be obtained is that the AUTO mode is able to successfully reach the target waypoints. Moreover, the vehicle was able to reasonably maintain the desired speed of 2 m/s, which is worth mentioning as it is similar to the GNSS receiver error itself. Despite this, there are points along the track where the robot significantly drops in speed, potentially due to small obstacles in the uneven gravel terrain portion. Slight yaw oscillations were observed, which did not affect the vehicle's ability to track a requested position, but caused it to do so in a subtle zig-zag motion. If a higher target speed had been used, as previously noted, these oscillations would likely have diminished.

With an improved and sturdier wheel design, dedicated tuning for the ground modes and increased yaw authority, achieved by slightly tilting each motor to partially obtain yaw control from differential thrust, the results obtained could potentially be improved.

5.3.4 Energy efficiency

One of the advantages of operating on the ground or in forward flight, compared to hovering, is the improved energy efficiency inherent to these modes. To calculate the energy consumption of the vehicle in different modes, only segments where the speed was constant were considered, to obtain the most accurate figure possible, with the drone not accelerating. Table 5.9 presents the measured energy consumption from these tests. As the maximum pitch angle was not achieved in the Ground and Full configurations due to the aircraft's instability, only the hovering power is presented for those configurations in hover mode. Moreover, for ground locomotion, the maximum pitch angle of 50° was used, as it was determined to be the most efficient. It is also worth mentioning that because the pitot tube is not aligned with the direction of movement in hover and ground modes, in these modes the ground speed is considered, whereas in forward flight the indicated airspeed is considered.

Regarding the hover mode, the addition of wings increases the aircraft's drag, making its operating



Figure 5.17: Aerial view of the ground waypoint test.

Table 5.9: Measured energy consumption.

Mode	Configuration	Quadcopter	Tailsitter	Ground	Full
Hover ($\theta_{max} = 30^\circ$)	Energy (Wh/km)	9.71 ± 1.78	21.45 ± 5.01	-	-
	@ Speed (m/s)	8.92 ± 1.48	2.97 ± 1.13	-	-
	Power (W)	302.6 ± 13.5	210.4 ± 13.2	-	-
	Stationary Power (W)	226.6 ± 10.0	223.4 ± 11.6	321.1 ± 14.1	355.6 ± 19.1
Forward flight	Energy (Wh/km)	-	6.55 ± 0.76	-	-
	@ Speed (m/s)	-	19.66 ± 1.46	-	-
	Power (W)	-	459.8 ± 16.0	-	-
Ground locomotion ($\theta_{max} = 50^\circ$)	Energy (Wh/km)	-	-	3.48 ± 0.14	-
	@ Speed (m/s)	-	-	5.01 ± 0.27	-
	Power (W)	-	-	62.8 ± 4.7	-

speed much slower and, thus, its energy consumption higher. Nonetheless, the lift produced by the wings at the pitch angle of 30° proves to be beneficial, as the power consumption in this scenario is actually lower than that required to hover stationary in the same configuration, and much lower than that required to fly in the same attitude without wings. This results in a reduced range for the Tailsitter configuration, but slightly increased endurance, as seen in Table 5.10. In forward flight, on the other hand, the range increases compared to both configurations in hover, due to the higher achievable speeds but, due to the increased power requirement, the endurance decreases. The energy consumption per distance in forward flight is lower than in any configuration in hover mode, thus proving its efficiency benefit. Due

to the stability characteristics of the UAV in forward flight, as previously mentioned, to maintain a given positive angle of attack, a constant thrust differential is required to counteract the down pitching torque. The overall drag of the aircraft could be reduced with an improved aerodynamic design, and its stability characteristics improved by reducing the static margin.

The configurations with wheels, due to their increased mass, show a significantly lower endurance in hover. Nonetheless, when the robot operates on the ground, both the range and endurance increase, as this was shown to be the most efficient operating mode. If tests in ground mode had been conducted with higher power (and consequently higher speed), as the vehicle's airspeed nears that which is experienced in forward flight, both modes would be similar in energy consumption, as the drag acting on the vehicle would be approximately the same. At lower speeds, where the ground mode is most effective, and where forward flight is not possible, the ground locomotion shows its great advantage.

Table 5.10: Estimated maximum range and endurance (Gensace Bashing battery, 74 Wh used).

Mode	Configuration	Quadcopter	Tailsitter	Ground	Full
Hover ($\theta_{max} = 30^\circ$)	Range (km)	7.868 ± 1.372	3.763 ± 1.454	-	-
	Endurance (H:M:S)	00:14:42 ± 00:00:40	00:21:11 ± 00:01:19	-	-
	Stationary endurance (H:M:S)	00:19:37 ± 00:00:51	00:19:55 ± 00:01:04	00:13:51 ± 00:00:37	00:12:31 ± 00:00:41
Forward flight	Range (km)	-	11.418 ± 1.095	-	-
	Endurance (H:M:S)	-	00:09:39 ± 00:00:20	-	-
Ground locomotion ($\theta_{max} = 50^\circ$)	Range (km)	-	-	21.293 ± 0.844	-
	Endurance (H:M:S)	-	-	01:11:05 ± 00:05:26	-

As previously seen, the addition of wings brought some benefits to hovering flight. This was further explored by mounting the wings with two different incidence angles, of -10° and -30° . As shown in Table 5.11, the range and endurance both increased with these changes. The configuration with the wings mounted at -30° even became more efficient than forward flight, when moving forward. However, mounting the wings like this brings on additional challenges, as a lift force is produced due to the flow from the propellers. Not only did the aircraft become unstable in hovering flight, but a coupled roll-yaw motion was observed, as the differential thrust required for yaw results in a differential flow over the wing, which in turn produces differential lift along the span, producing a yaw torque. This instability was significantly more pronounced when the wing was mounted at -30° .

Table 5.11: Wing incidence angle comparison in hover ($\theta_{max} = 30^\circ$) (Gensace Bashing battery, 74 Wh used).

Incidence angle	0° (Tailsitter)	-10°	-30°
Energy (Wh/km)	21.45 ± 5.01	18.88 ± 4.14	4.23 ± 0.39
@ Speed (m/s)	2.97 ± 1.13	3.47 ± 0.98	8.38 ± 0.06
Power (W)	210.4 ± 13.2	199.9 ± 20.4	127.7 ± 12.5
Stationary Power (W)	223.4 ± 11.6	266.3 ± 15.0	290.1 ± 15.3
Range (km)	3.763 ± 1.454	4.611 ± 1.133	17.565 ± 1.599
Endurance (H:M:S)	00:21:11 ± 00:01:19	00:22:27 ± 00:02:44	00:34:56 ± 00:03:25
Stationary endurance (H:M:S)	00:19:55 ± 00:01:04	00:16:43 ± 00:00:57	00:15:20 ± 00:00:50

Figure 5.18 summarises all the data considered for the energy analysis of the different modes. It is clear that adding the ground and forward flight capability expands the operating envelope of the base multirotor, allowing it to operate at a wide range of speeds, and simultaneously improves its efficiency. Although no data is present from tests in inclined surfaces, this operating environment would be situated in between the ground and hover areas, depending on the inclination.

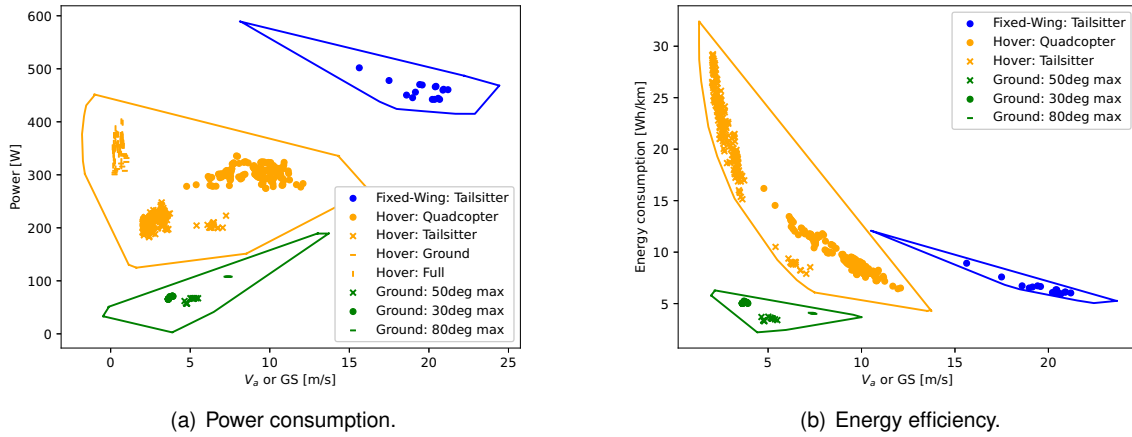


Figure 5.18: Energy-velocity mapping.

Overall, both added modes proved to be more energy efficient than the existing base hovering mode, with the required modifications having different levels of impact on the hover mode, which could even be positive, as the wings were shown to be able to increase the endurance in hovering flight. Depending on each mission's requirements, and given the vehicle's high modularity, the operating configuration must be chosen, even possibly changed during the operation.

5.3.5 Multimodality

Lastly, besides the observed efficiency improvement, the vehicle's multimodality enables it to operate in more complex scenarios, combining all three operating modes, as needed. As the vehicle was built in a modular fashion, only the components required for a given mission need to be assembled on the drone. With the same platform, all three modes were demonstrated to be possible, in all configurations, except for forward flight, where the vehicle was not tested with wheels.

Table 5.12: Maximum measured speed (m/s).

Mode	Quadcopter	Tailsitter	Ground	Full
Hover ($\theta_{max} = 30^\circ$)	19.54 ± 0.27	8.15 ± 0.23	4.38 ± 0.46	1.47 ± 0.14
Forward flight	-	21.37 ± 0.08	-	-
Ground locomotion ($\theta_{max} = 80^\circ$)	-	-	7.69 ± 0.49	-

As seen in Figure 5.18 and Table 5.12 (note that the speed achieved in ground mode was using the minimum throttle required to achieve a pitch angle of 80°), the operating envelope of the vehicle is greatly expanded, compared to the base Quadcopter configuration. Not only was the vehicle able to

reach higher speeds in forward flight, but the operation at lower speeds was also made more efficient. With the modular integration of the three modes, the advantages of conventional fixed-wing aircraft and autonomous rovers could be retained, while maintaining the ability to hover. This way, the aircraft can cover long distances quickly in forward flight mode, approach proximity inspection targets in ground mode, and maintain position in the air in hover mode. With the implemented AUTO mode, a mission can be planned combining all modes of operation, as required for each step of the mission, with no operator input required, provided that the mode transitions are specified in the mission commands or that an onboard computer commands these transitions.



Figure 5.19: Aerial-ground locomotion.

This versatility also extends the possible operating environments of the robot, in particular on the ground. As an example, the vehicle can roll on the ground efficiently, when an aerial perspective is not required, and go over obstacles on the ground by flying over them. This capability is shown in Figure 5.19, where the vehicle flies over an obstacle on the ground, combining both ground and aerial modes¹¹.



Figure 5.20: Wall climb test.

Moreover, although automatic ground locomotion capability was only developed for approximately flat surfaces, the robot is able to roll over surfaces with any inclination¹². As any inclination may be climbed, the vehicle was also tested in vertical walls, which it was able to climb, as seen in Figure 5.20¹³. In this mode, compared to hovering in the air, a power consumption increase was observed, with an average power consumption of $386.0 \text{ W} \pm 3.0$ during the portion where the robot was holding height. This is because the vehicle is using thrust to push itself into the wall, as an average pitch angle of $-12.6^\circ \pm 0.3$ was registered during the climb. Ideally, only a minimal pitch angle would be applied, such that only the required force to maintain the vehicle adhered to the

wall is applied onto the wall, but as this test was performed manually, a higher angle was commanded.

¹¹Video of the robot going over this obstacle is available at: <https://youtu.be/4Cwt6n7e0qw>.

¹²Video of the vehicle moving on an inclined surface (at IST - Alameda) is available at: <https://youtu.be/j1jjxoIg-Fg>.

¹³Video of the robot climbing walls is available at: <https://youtu.be/z6IsmNJf77U>.

Chapter 6

Conclusions

Considering the results obtained throughout the present work, the final conclusions are laid out, as well as suggestions for future work on the subject of multimodal UAV's.

6.1 Achievements

Multimodal vehicles are capable of operating in broader environments and, in doing so, can operate more efficiently than single-mode vehicles, using less energy. In this work, a prototype trimodal vehicle was proposed, capable of achieving ground locomotion, hovering flight, and forward flight. This prototype proved to be fully functional and capable of achieving its purpose throughout more than 10 hours of tests. Additionally, it was able to do so using only a single set of actuators, an approach which significantly simplifies the overall control architecture used on the vehicle with the use of a single common approach. This prototype demonstrates the feasibility of combining hover, forward flight and ground locomotion in a single platform.

During the UAV's test campaign, hovering flight was considered as the base reference mode, and expanding on that, the robot was able to move on the ground in a controlled manner and to fly thanks to lift produced by its wings, in forward flight. Across all three modes, satisfactory flight/drive characteristics were observed, bearing in mind that the focus of this work was not to fine-tune a finished product. In particular, on the ground, automatic locomotion was achieved, thanks to modifications made to the ArduPilot firmware. This enabled the possibility of executing fully automatic missions, interchanging between all three operating modes. As a careful analysis of the ArduPilot source code was required, a description of all applicable ArduPilot controllers (existing and implemented in this work) was also made. In addition, a comprehensive characterisation of the aerodynamic behaviour of the trimodal UAV was made in wind tunnel testing, providing valuable data for future design iterations.

Besides achieving multimodal operation, the following conclusions from the tests conducted are of particular relevance. In ground operations, the vehicle can achieve its peak efficiency, with an improvement of 2.7 times increase in range and a 4.8 times increase in endurance compared to the base Quadcopter operating in hover. Moreover, in forward flight, the vehicle showed an increase of 1.5 times in range.

Additionally, not only was an efficiency increase possible with these two modes, but the addition of wings also made hovering flight more efficient. With the originally intended wings, an improvement in endurance of 1.4 times was observed. By mounting the wings with an incidence angle of -10° relative to the propeller rotation axis, an improvement in endurance of 1.5 times was observed. When the wing was mounted at -30° , the endurance significantly improved, by a factor of 2.4, with even the range increasing 2.2 times, at the cost of greatly reduced stability.

In the end, a prototype was obtained which fulfilled the initial objectives of multimodal capability, with an expanded operating envelope, upon which additional features and applications can be built.

6.2 Future work

Taking into account the limitations and recommendations made throughout this work, the following aspects should be the focus of future work on this topic.

Regarding the design of the vehicle, improved designs for the wheels should be explored. A lighter wheel with more rigidity and a reduced aerodynamic footprint could be manufactured using carbon fibre composites. In addition, mechanisms that reduce the wheel's impact on the aerial flight modes or blend it into the frame could also prove beneficial. Furthermore, an improved aerodynamic design could not only improve the efficiency of the aircraft but also enhance its flying characteristics. Proper placement of the wings with respect to the centre of gravity, by blending the frame with the wings could make the vehicle more stable in forward flight. Similarly, the shape of the frame should be optimised to minimise the drag experienced in forward flight. At last, the possibility of actuating the wings to control their incidence angle should be explored, so that the benefits of lowering the angle of attack of the wing can be explored in forward hover while maintaining stability in stationary hover.

Now considering improvements to the vehicle's control, these mainly concern forward flight and ground operations. First, the approach used to implement position control on the ground modes should be revisited, taking the position control used in ArduRover as an example, and building up on that to obtain yaw, pitch and throttle commands. Maximising the amount of pitch with minimal throttle on the ground could increase efficiency, and thus any approach to velocity control should aim to achieve this. Proper throttle control implementation should also enable automatic motion on inclined surfaces, making the vehicle fully automatic. Considering the forward flight attitude controller, the approach of using the exact same controller for hovering flight and forward flight for control surface-less tailsitters implemented by ArduPilot should be rethought, given the significant change in dynamics that is observed. Lastly, proper gain tuning techniques and procedures should be studied and implemented, in particular for the ground controllers.

Considering the potential applications of a similar prototype, higher-level applications should be built on top of the existing prototype to implement autonomous obstacle avoidance and navigation using the vehicle's multimodality. Finally, depending on the desired application for the vehicle, sensor payloads should be researched, bearing in mind the changes in attitude that can be experienced across all operating modes.

Bibliography

- [1] X. Liu, M. Dou, D. Huang, S. Gao, R. Yan, B. Wang, J. Cui, Q. Ren, L. Dou, Z. Gao, J. Chen, and B. M. Chen. TJ-FlyingFish: Design and Implementation of an Aerial-Aquatic Quadrotor with Tilttable Propulsion Units. In *2023 IEEE International Conference on Robotics and Automation (ICRA)*, pages 7324–7330, London, United Kingdom, May 2023. doi:10.1109/ICRA48891.2023.10160899.
- [2] Y. Zeng, Q. Hu, S. Yin, B. Tong, and T. Zhang. The Ground Motion Dynamics Analysis of a Bionic Amphibious Robot with Undulatory Fins. In *2021 IEEE International Conference on Real-time Computing and Robotics (RCAR)*, pages 1385–1390, Xining, China, July 2021. doi:10.1109/RCAR52367.2021.9517681.
- [3] M. Sivakumar and N. M. TYJ. A Literature Survey of Unmanned Aerial Vehicle Usage for Civil Applications. *Journal of Aerospace Technology and Management*, 13:e4021, 2021. doi:10.1590/jatm.v13.1233.
- [4] A. K. V. de Oliveira, M. Aghaei, and R. Rütther. Automatic Inspection of Photovoltaic Power Plants Using Aerial Infrared Thermography: A Review. *Energies*, 15(6), 2022. doi:10.3390/en15062055.
- [5] P. Radoglou-Grammatikis, P. Sarigiannidis, T. Lagkas, and I. Moscholios. A compilation of UAV applications for precision agriculture. *Computer Networks*, 172:107148, 2020. doi:10.1016/j.comnet.2020.107148.
- [6] S. Jordan, J. Moore, S. Hovet, J. Box, J. Perry, K. Kirsche, D. Lewis, and Z. T. H. Tse. State-of-the-art technologies for UAV inspections. *IET Radar, Sonar & Navigation*, 12(2):151–164, 2018. doi:10.1049/iet-rsn.2017.0251.
- [7] P. Addabbo, A. Angrisano, M. L. Bernardi, G. Gagliarde, A. Mennella, M. Nisi, and S. L. Ullo. UAV system for photovoltaic plant inspection. *IEEE Aerospace and Electronic Systems Magazine*, 33(8):58–67, 2018. doi:10.1109/MAES.2018.170145.
- [8] P. Skorput, S. Mandzuka, and H. Vojvodic. The use of Unmanned Aerial Vehicles for forest fire monitoring. In *2016 International Symposium ELMAR*, pages 93–96, Zadar, Croatia, September 2016. doi:10.1109/ELMAR.2016.7731762.
- [9] E. Sihite, A. Kalantari, R. Nemovi, A. Ramezani, and M. Gharib. Multi-Modal Mobility Morphobot (M4) with appendage repurposing for locomotion plasticity enhancement. *Nature Communications*, 14(1):3323, June 2023. doi:10.1038/s41467-023-39018-y.

- [10] T. Dias. Design and development of a multi-modal aerial-ground vehicle for long-endurance inspection applications. MSc Thesis in Electrical and Computer Engineering, Instituto Superior Técnico, Lisboa, Portugal, December 2021. URL <https://fenix.tecnico.ulisboa.pt/cursos/mec/dissertacao/1691203502344693>.
- [11] M. Cao, X. Xu, S. Yuan, K. Cao, K. Liu, and L. Xie. DoubleBee: A Hybrid Aerial-Ground Robot with Two Active Wheels. 2023. doi:10.48550/arXiv.2303.05075.
- [12] Z. Zheng, J. Wang, Y. Wu, Q. Cai, H. Yu, R. Zhang, J. Tu, J. Meng, G. Lu, and F. Gao. Roller-quadrotor: A novel hybrid terrestrial/aerial quadrotor with unicycle-driven and rotor-assisted turning. In *2023 IEEE/RSJ International Conference on Intelligent Robots and Systems (IROS)*, pages 6927–6934, Detroit, USA, October 2023. doi:10.1109/IROS55552.2023.10341703.
- [13] H. C. Choi, I. Wee, M. Corah, S. Sabet, T. Kim, T. Touma, D. H. Shim, and A. Agha-mohammadi. BAXTER: Bi-Modal Aerial-Terrestrial Hybrid Vehicle for Long-Endurance Versatile Mobility”, booktitle=“Experimental Robotics. pages 60–72, Cham, 2021. Springer International Publishing. ISBN 978-3-030-71151-1.
- [14] N. Meiri and D. Zarrouk. Flying STAR, a Hybrid Crawling and Flying Sprawl Tuned Robot. In *2019 International Conference on Robotics and Automation (ICRA)*, pages 5302–5308, Montreal, Canada, May 2019. doi:10.1109/ICRA.2019.8794260.
- [15] W. Wang, C. y. Li, L. h. Chu, and C. y. Qu. Study on air-ground amphibious agricultural information collection robot. In *2016 13th International Conference on Ubiquitous Robots and Ambient Intelligence (URAI)*, pages 938–944, Xian, China, August 2016. doi:10.1109/URAI.2016.7734115.
- [16] L. A. Young. A Multi-Modality Mobility Concept for a Small Package Delivery UAV. In *AHS International Technical Meeting on VTOL Unmanned Systems and Autonomy*, 2017.
- [17] D. D. Fan, R. Thakker, T. Bartlett, M. B. Miled, L. Kim, E. Theodorou, and A. Agha-Mohammadi. Autonomous Hybrid Ground/Aerial Mobility in Unknown Environments. In *2019 IEEE/RSJ International Conference on Intelligent Robots and Systems (IROS)*, pages 3070–3077, Macau, China, November 2019. doi:10.1109/IROS40897.2019.8968276.
- [18] J. R. Page and P. E. I. Pounds. The Quadroller: Modeling of a UAV/UGV hybrid quadrotor. In *2014 IEEE/RSJ International Conference on Intelligent Robots and Systems*, pages 4834–4841, Chicago, USA, September 2014. doi:10.1109/IROS.2014.6943249.
- [19] S. Sabet, A. Agha-Mohammadi, A. Tagliabue, D. S. Elliott, and P. E. Nikravesh. Rollocopter: An Energy-Aware Hybrid Aerial-Ground Mobility for Extreme Terrains. In *2019 IEEE Aerospace Conference*, Big Sky, USA, March 2019. doi:10.1109/AERO.2019.8741685.
- [20] A. Kalantari and M. Spenko. Design and experimental validation of HyTAQ, a Hybrid Terrestrial and Aerial Quadrotor. In *2013 IEEE International Conference on Robotics and Automation*, pages 4445–4450, Karlsruhe, Germany, May 2013. doi:10.1109/ICRA.2013.6631208.

- [21] H. Jia, S. Bai, R. Ding, J. Shu, Y. Deng, B. L. Khoo, and P. Chirarattananon. A Quadrotor With a Passively Reconfigurable Airframe for Hybrid Terrestrial Locomotion. *IEEE/ASME Transactions on Mechatronics*, 27(6):4741–4751, 2022. doi:10.1109/TMECH.2022.3164929.
- [22] O. Walvekar and S. R. Chakravarthy. A hybrid rans-les transient study of propeller-airframe interaction for electric uav. In *AIAA AVIATION 2023 Forum*, San Diego, USA, June 2023. doi:10.2514/6.2023-3765.
- [23] P. Ruchała. Aerodynamic Interference Between Pusher Propeller Slipstream and an Airframe – Literature Review. *Journal of KONES*, 24(3):237–244, 2017. doi:10.5604/01.3001.0010.3084.
- [24] UAVision Ogassa OGS42V, 2016. URL <https://www.uavision.com/ogassa-ogs42v>. (accessed on 27-09-2023).
- [25] Tekever AR3, 2022. URL <https://www.tekever.com/models/ar3/>. (accessed on 27-09-2023).
- [26] VTOne, 2023. URL <https://beyond-vision.com/vtone-ai-powered-vtol-drone/>. (accessed on 06-05-2024).
- [27] M. Okulski and M. Ławryńczuk. A Small UAV Optimized for Efficient Long-Range and VTOL Missions: An Experimental Tandem-Wing Quadplane Drone. *Applied Sciences*, 12(14), 2022. doi:10.3390/app12147059.
- [28] Evolonic NF3, 2022. URL evolonic.de. (accessed on 23-09-2023).
- [29] M. Ashish, A. Muraleedharan, S. CM, R. R. Bhavani, and N. Akshay. Autonomous Payload Delivery using Hybrid VTOL UAVs for Community Emergency Response. In *2020 IEEE International Conference on Electronics, Computing and Communication Technologies (CONECCT)*, pages 1–6, Bangalore, India, July 2020. doi:10.1109/CONECCT50063.2020.9198490.
- [30] AeroTéc UAV-ART, 2022. URL <https://www.aerotec.pt/atlas>. (accessed on 22-09-2023).
- [31] Y. T. Yeo and H. H. Liu. Transition control of a tilt-rotor vtol uav. In *2018 AIAA Guidance, Navigation, and Control Conference*, Kissimmee, USA, January 2018. doi:10.2514/6.2018-1848.
- [32] J. A. Bautista, A. Osorio, and R. Lozano. Modeling and analysis of a tricopter/flying-wing convertible UAV with tilt-rotors. In *2017 International Conference on Unmanned Aircraft Systems (ICUAS)*, pages 672–681, Miami, USA, June 2017. doi:10.1109/ICUAS.2017.7991502.
- [33] C. Papachristos, K. Alexis, and A. Tzes. Towards a high-end unmanned tri-TiltRotor: design, modeling and hover control. In *2012 20th Mediterranean Conference on Control & Automation (MED)*, pages 1579–1584, Barcelona, Spain, July 2012. doi:10.1109/MED.2012.6265864.
- [34] O. Gur and G. Lazar. Prop-rotor design for an electric tilt-rotor vehicle. In *American Helicopter Society, Future Vertical Lift Aircraft Design Conference*, pages 328–339, San Francisco, USA, January 2012.

- [35] M. Mousaei, J. Geng, A. Keipour, D. Bai, and S. Scherer. Design, Modeling and Control for a Tilt-rotor VTOL UAV in the Presence of Actuator Failure. In *2022 IEEE/RSJ International Conference on Intelligent Robots and Systems (IROS)*, pages 4310–4317, Kyoto, Japan, October 2022. doi:10.1109/IROS47612.2022.9981806.
- [36] C. Papachristos, K. Alexis, and A. Tzes. Dual–authority thrust–vectoring of a tri–tiltrotor employing model predictive control. *Journal of intelligent & robotic systems*, 81:471–504, 2016. doi:10.1007/s10846-015-0231-1.
- [37] J. Zhang, P. Bhardwaj, S. A. Raab, S. Saboo, and F. Holzapfel. *Control Allocation Framework for a Tilt-rotor Vertical Take-off and Landing Transition Aircraft Configuration*. 2018. doi:10.2514/6.2018-3480.
- [38] H. Zhao, B. Wang, Y. Shen, Y. Zhang, N. Li, and Z. Gao. Development of Multimode Flight Transition Strategy for Tilt-Rotor VTOL UAVs. *Drones*, 7(9), 2023. doi:10.3390/drones7090580.
- [39] K. Muraoka, N. Okada, and D. Kubo. Quad tilt wing vtol uav: Aerodynamic characteristics and prototype flight. In *AIAA Infotech@Aerospace Conference*, Seattle, USA, April 2012. doi:10.2514/6.2009-1834.
- [40] E. Cetinsoy, S. Dikyar, C. Hancer, K. Oner, E. Sirimoglu, M. Unel, and M. Aksit. Design and construction of a novel quad tilt-wing UAV. *Mechatronics*, 22(6):723–745, 2012. doi:10.1016/j.mechatronics.2012.03.003. Special Issue on Intelligent Mechatronics (LSMS2010 & ICSEE2010).
- [41] D. Rohr, M. Studiger, T. Stastny, N. R. J. Lawrance, and R. Siegwart. Nonlinear Model Predictive Velocity Control of a VTOL Tiltwing UAV. *IEEE Robotics and Automation Letters*, 6(3):5776–5783, 2021. doi:10.1109/LRA.2021.3084888.
- [42] G. J. Ducard and M. Allenspach. Review of designs and flight control techniques of hybrid and convertible VTOL UAVs. *Aerospace Science and Technology*, 118:107035, 2021. doi:10.1016/j.ast.2021.107035.
- [43] Wingtra One Gen II, 2020. URL <https://wingtra.com/mapping-drone-wingtraone/#intro>. (accessed on 22-09-2023).
- [44] S. Fuhrer, S. Verling, T. Stastny, and R. Siegwart. Fault-tolerant Flight Control of a VTOL Tailsitter UAV. In *2019 International Conference on Robotics and Automation (ICRA)*, pages 4134–4140, Montreal, Canada, May 2019. doi:10.1109/ICRA.2019.8793467.
- [45] V. Hrishikeshavan, C. Bogdanowicz, and I. Chopra. Performance and testing of a quad rotor biplane micro air vehicle for multi role missions. In *52nd Aerospace Sciences Meeting*, National Harbor, USA, January 2014. doi:10.2514/6.2014-0727. URL <https://arc.aiaa.org/doi/abs/10.2514/6.2014-0727>.

- [46] P. Ryseck, G. Jacobellis, D. Yeo, and I. Chopra. Experimental Flight Testing of Wing Configurations for High-Speed Mini Quadrotor Biplane Tail-sitter. In *9th Biennial Autonomous VTOL Technical Meeting*, Online, January 2021.
- [47] B. Phillips, V. Hrishikeshavan, O. Rand, and I. Chopra. Design and Development of a Scaled Quadrotor Biplane with Variable Pitch Proprotors for Rapid Payload Delivery. In *AHS 72nd Annual Forum*, West Palm Beach, FL, USA, May 2016.
- [48] N. Raj, R. Banavar, Abhishek, and M. Kothari. Attitude Control of Novel Tail Sitter: Swiveling Biplane–Quadrotor. *Journal of Guidance, Control, and Dynamics*, 43(3):599–607, 2020. doi:10.2514/1.G004697.
- [49] C. D. Wagter, B. Remes, R. Ruijsink, F. van Tienen, and E. van der Horst. Design and Testing of a Vertical Take-Off and Landing UAV Optimized for Carrying a Hydrogen Fuel Cell with a Pressure Tank. *Unmanned Systems*, 08(04):279–285, 2020. doi:10.1142/S2301385020500223.
- [50] *DJI Flame Wheel ARF Kit*. DJI, 2013. URL <https://www-v1.dji.com/flame-wheel-arf.html>. (accessed on 04-10-2023).
- [51] J. Ahn and D. Lee. *Aerodynamic Characteristics of a Micro Air Vehicle and the Influence of Propeller Location*. 2013. doi:10.2514/6.2013-2655.
- [52] *LW-PLA NATURAL*. ColorFabb, 2024. URL <https://colorfabb.com/lw-pla-natural>. (accessed on 18-05-2024).
- [53] A. N. D. Lucena, B. M. F. D. Silva, and L. M. G. Goncalves. Double Hybrid Tailsitter Unmanned Aerial Vehicle With Vertical Takeoff and Landing. *IEEE Access*, 10:32938–32953, 2022. doi:10.1109/access.2022.3161490.
- [54] *Airfoil Tools*. Airfoil Tools, 2023. URL <http://airfoiltools.com>. (accessed on 27-11-2023).
- [55] *XFLR5*, 2021. URL <https://web.mit.edu/drela/Public/web/xfoil/>. (accessed on 28-11-2023).
- [56] *flow5*. Cère-Aéro, 2023. URL <https://flow5.tech>. (accessed on 28-11-2023).
- [57] *eCalc*. Markus Müller, 2023. URL <https://www.ecalc.ch/index.htm>. (accessed on 05-12-2023).
- [58] J. Gundlach. *Designing Unmanned Aircraft Systems: A Comprehensive Approach, Second Edition*. American Institute of Aeronautics and Astronautics, Inc., July 2014. doi:10.2514/4.102615.
- [59] *Gensace Bashing 4S1P 5000mAh XT90*. Gensace, 2013. URL <https://www.gensace.de/gensace-5000mah-14-8v-4s1p-60c-lipo-battery-pack-with-xt90-plug-bashing-series.html>. (accessed on 06-11-2023).
- [60] *Gensace Soaring 4S1P 4000mAh EC5*. Gensace, 2013. URL <https://www.gensace.de/gensace-soaring-4000mah-14-8v-30c-4s1p-lipo-battery-pack-with-ec5-plug-2298.html>. (accessed on 06-11-2023).

- [61] O.Tremblay and L. Dessaint. Experimental Validation of a Battery Dynamic Model for EV Applications. *World Electric Vehicle Journal*, 3(2):289–298, 2009. doi:10.3390/wevj3020289.
- [62] *ArduPilot*. ArduPilot, 2024. URL <https://ardupilot.org>. (accessed on 24-05-2024).
- [63] *Battery Voltage Compensation*. ArduPilot, 2022. URL <https://ardupilot.org/plane/docs/battery-voltage-compensation.html>. (accessed on 09-11-2023).
- [64] A. Gong and D. Verstraete. Experimental Testing of Electronic Speed Controllers for UAVs. In *53rd AIAA/SAE/ASEE Joint Propulsion Conference*, Atlanta, USA, July 2017. American Institute of Aeronautics and Astronautics. doi:10.2514/6.2017-4955.
- [65] C. R. Green and R. A. McDonald. Modeling and Test of the Efficiency of Electronic Speed Controllers for Brushless DC Motors. In *15th AIAA Aviation Technology, Integration, and Operations Conference*, Dallsa, USA, June 2015. American Institute of Aeronautics and Astronautics. doi:10.2514/6.2015-3191.
- [66] *Airgear 350 Combo Set Multi-Rotor UAV Power*. T-Motor, 2015. URL <https://store.tmotor.com/product/air-gear-350-combo-set.html>. (accessed on 07-11-2023).
- [67] *E305 Tuned Propulsion System*. DJI, 2015. URL <https://www-v1.dji.com/e305.html>. (accessed on 07-11-2023).
- [68] O. Solomon and P. Famouri. Dynamic Performance of a Permanent Magnet Brushless DC Motor for UAV Electric Propulsion System - Part I. In *IECON 2006 - 32nd Annual Conference on IEEE Industrial Electronics*, pages 1400–1405, Paris, France, November 2006. doi:10.1109/IECON.2006.347808.
- [69] O. Gur and A. Rosen. Optimizing Electric Propulsion Systems for Unmanned Aerial Vehicles. *Journal of Aircraft*, 46(4):1340–1353, July 2009. doi:10.2514/1.41027.
- [70] *T-Motor 2814 Long Shaft*. T-Motor, 2019. URL https://uav-en.tmotor.com/html/2019/AT_0226/214.html. (accessed on 07-11-2023).
- [71] M. H. McCrink and J. W. Gregory. Blade Element Momentum Modeling of Low-Reynolds Electric Propulsion Systems. *Journal of Aircraft*, 54(1):163–176, Jan. 2017. doi:10.2514/1.c033622.
- [72] W. Johnson. *Rotorcraft Aeromechanics*. Cambridge University Press, Apr. 2013. doi:10.1017/cbo9781139235655.
- [73] *Technical Information*. APC Propellers, 2023. URL <https://www.apcprop.com/technical-information/file-downloads/>. (accessed on 09-11-2023).
- [74] W. Khan and M. Nahon. A propeller model for general forward flight conditions. *International Journal of Intelligent Unmanned Systems*, 3(2/3):72–92, May 2015. doi:10.1108/ijius-06-2015-0007.

- [75] Z. Czyż, P. Karpiński, K. Skiba, and M. Wendeker. Wind Tunnel Performance Tests of the Propellers with Different Pitch for the Electric Propulsion System. *Sensors*, 22(1):2, Dec. 2021. doi:10.3390/s22010002.
- [76] P. Zhao, Q. Quan, S. Chen, D. Tang, and Z. Deng. Experimental investigation on hover performance of a single-rotor system for Mars helicopter. *Aerospace Science and Technology*, 86:582–591, Mar. 2019. doi:10.1016/j.ast.2019.01.052.
- [77] *FrSky Taranis X9D Plus 2019*. FrSky, 2019. URL <https://www.frsky-rc.com/product/taranis-x9d-plus-2019/>. (accessed on 07-12-2023).
- [78] *FrSky RX6R*. FrSky, 2020. URL <https://www.frsky-rc.com/product/rx6r/>. (accessed on 07-12-2023).
- [79] *CubePilot CubeOrange*. CubePilot, 2023. URL <https://docs.cubepilot.org/user-guides/autopilot/the-cube-module-overview>. (accessed on 07-12-2023).
- [80] *ADS-B IN Carrier Board*. CubePilot, 2023. URL <https://docs.cubepilot.org/user-guides/carrier-boards/ads-b-carrier-board>. (accessed on 07-12-2023).
- [81] *UT203R/UT204R AC/DC Clamp Meters User Manual*. UNI-T, 2022. URL <https://meters.uni-trend.com/download/ut203r-ut204r-user-manual/?wpdmdl=7239&refresh=6696222b7852b1721115179>. (accessed on 09-01-2024).
- [82] *Here+V2 User Manual*. CubePilot, 2019. URL <https://docs.cubepilot.org/user-guides/here+/here+v2-user-manual>. (accessed on 07-12-2023).
- [83] *Holybro Sik Telemetry*. Holybro, 2018. URL <https://docs.holybro.com/radio/sik-telemetry-radio-v3>. (accessed on 07-12-2023).
- [84] *Pixhawk standards*. Dronecode Project, Inc., 2023. URL <https://pixhawk.org>.
- [85] *PX4*. DroneCode Foundation, 2024. URL <https://px4.io>. (accessed on 24-05-2024).
- [86] H. Bouadi, M. Bouchoucha, and M. Tadjine. Sliding Mode Control based on Backstepping Approach for an UAV Type-Quadrotor. *International Journal of Applied Mathematics and Computer Sciences*, 4:12–17, 01 2007. doi:10.5281/zenodo.1077447.
- [87] R. Beard. Quadrotor dynamics and control. *Brigham Young University*, 2008.
- [88] M. Hua, T. Hamel, P. Morin, and C. Samson. Introduction to feedback control of underactuated VTOLvehicles: A review of basic control design ideas and principles. *IEEE Control Systems Magazine*, 33(1):61–75, 2013. doi:10.1109/MCS.2012.2225931.
- [89] R. W. Beard and T. W. McLain. *Small Unmanned Aircraft: Theory and Practice*. Princeton University Press, Princeton, NJ, Feb. 2012. ISBN 978-0-69-114921-9.

- [90] M. Pimentel. Design and Control of a Bimodal aerial robot for locomotion in flat and inclined surfaces. MSc Thesis in Aerospace Engineering, Instituto Superior Técnico, Lisboa, Portugal, April 2021. URL <https://fenix.tecnico.ulisboa.pt/cursos/meaer/dissertacao/283828618790642>.
- [91] *Extended Kalman Filter Navigation Overview and Tuning*. ArduPilot, 2021. URL <https://ardupilot.org/dev/docs/extended-kalman-filter.html>. (accessed on 27-03-2024).
- [92] *Managing Gyro Noise with the Dynamic Harmonic Notch Filters*. ArduPilot, 2024. URL <https://ardupilot.org/copter/docs/common-imu-notch-filtering.html>. (accessed on 28-02-2024).
- [93] *Tailsitter VTOL Tuning*. ArduPilot, 2023. URL <https://ardupilot.org/plane/docs/tailsitter-tuning-guide.html>. (accessed on 28-02-2024).
- [94] *QuikTune*. ArduPilot, 2024. URL <https://ardupilot.org/copter/docs/quiktune.html>. (accessed on 26-05-2024).
- [95] L. Hall. ArduPilot Developer Conference 2021: S-Curves by Leonard Hall, 2021. URL <https://youtu.be/MQiNDJGJDWs>.
- [96] *Flight Modes*. ArduPilot, 2024. URL <https://ardupilot.org/plane/docs/flight-modes.html>. (accessed on 27-03-2024).
- [97] *QuadPlane Flight modes*. ArduPilot, 2022. URL <https://ardupilot.org/plane/docs/quadplane-flight-modes.html>. (accessed on 25-03-2024).
- [98] *Tailsitter Planes*. ArduPilot, 2024. URL <https://ardupilot.org/plane/docs/guide-tailsitter.html>. (accessed on 25-03-2024).
- [99] *Series 1585 Thrust Stand*. Tyto Robotics, 2022. URL <https://www.tytorobotics.com/pages/series-1580-1585>. (accessed on 01-04-2024).
- [100] M. Wemans. Caracterização do túnel aerodinâmico da Academia da Força Aérea, 2019. URL <http://hdl.handle.net/10400.26/39772>.
- [101] A. Filippone. *Advanced Topics in Aerodynamics*. 1999.
- [102] *Tuning Process Instructions*. ArduPilot, 2024. URL <https://ardupilot.org/plane/docs/quadplane-vtol-tuning-process.html>. (accessed on 23-04-2024).
- [103] *TECS (Total Energy Control System) for Speed and Height Tuning Guide*. ArduPilot, 2023. URL <https://ardupilot.org/plane/docs/tecs-total-energy-control-system-for-speed-height-tuning-guide.html>. (accessed on 15-03-2024).
- [104] *Mission Commands*. ArduPilot, 2024. URL https://ardupilot.org/plane/docs/common-mavlink-mission-command-messages-mav_cmd.html. (accessed on 21-03-2024).
- [105] *MAVLINK Common Message Set*. Dronecode Project, 2024. URL <https://mavlink.io/en/messages/common.html>. (accessed on 21-03-2024).

Appendix A

ArduPilot 4.5.0 controllers

At the time of writing, version 4.5 of ArduPilot has been released as a stable version, which introduces the following changes to the PID controllers: A derivative feed-forward term, a notch filter to both the target and error, and a saturation limit to the combined P and D term output were added.

Figures A.1 and A.2 show the updated block diagrams for the affected controllers, the attitude rate controller and vertical position controller (the ACCZ section) respectively. Note that the Attitude rate controller for aircraft with control surfaces follows the same architecture.

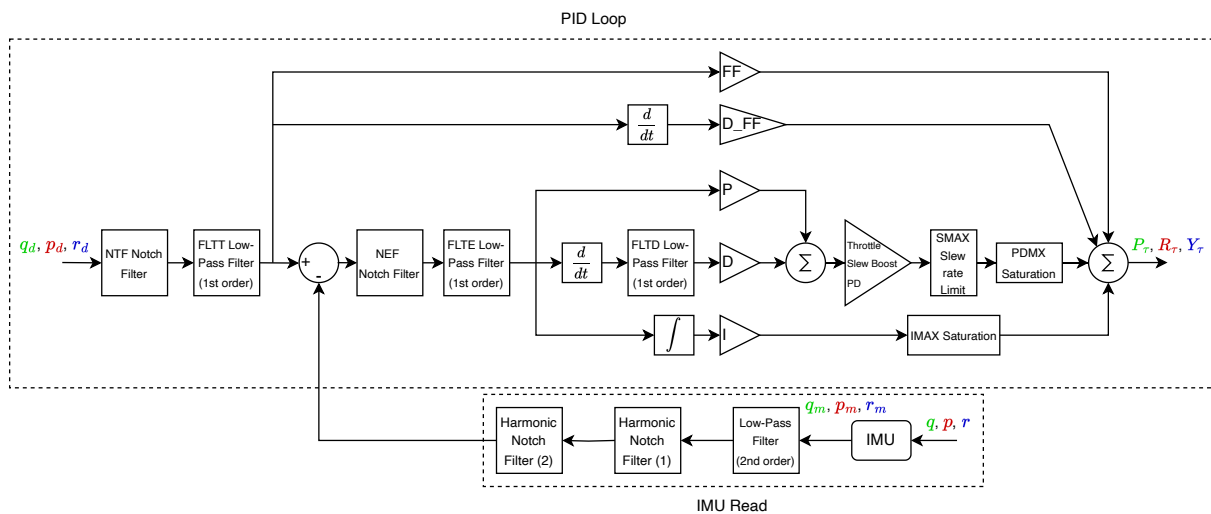


Figure A.1: Attitude rate PID controller (v4.5.0).

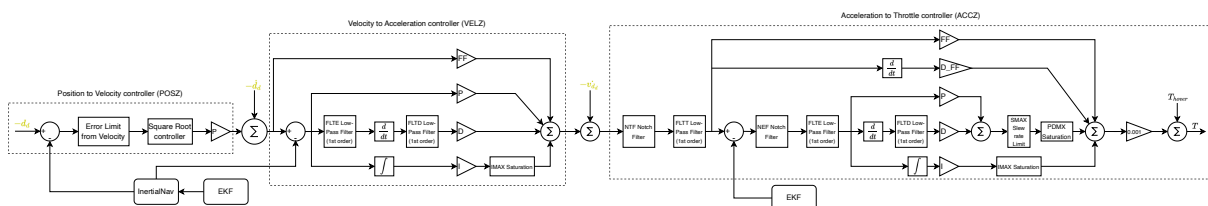


Figure A.2: Vertical position controller (v4.5.0).

Appendix B

ArduPilot controllers

This appendix describes the ArduPilot controllers which were not used during the testing of the prototype.

B.1 Forward flight

B.1.1 Position control

In forward flight, position control is assured by the L1 controller and the Total Energy Control System (TECS).

L1 controller

The L1 controller ensures horizontal position control and outputs a required lateral acceleration (to track the desired position) which is in turn converted to a commanded roll angle, via $\phi_d = \cos \theta \arctan\left(\frac{\text{latAccDem}}{g}\right)$. Unlike the hover position controller, the L1 controller and TECS are run at 10 Hz.

The L1 controller can be run in different modes, depending on the kind of input provided. First, a target heading can be provided, from where the lateral acceleration directly follows as $\text{latAccDem} = 2GS \frac{\sqrt{2}\pi}{L1_{period}} \sin \nu$, where ν is $\psi_d - \psi$, constrained to $-\pi$ to $+\pi$ radians. Analogue to the hovering position controller, where the UAV can maintain a given position, a loitering mode is available, where instead of maintaining a position, which is impossible in fixed-wing flight, the aircraft loiters around a given position, WP A, with a given radius, and in a specified direction, *loiter_direction* (+1 for CW and -1 for CCW).

When loitering, the controller has two stages, capture and circle. The capture mode is active when the aircraft is beyond the loiter radius, but to ensure a smooth transition, the switch between modes only occurs at the point where the demanded acceleration from both modes is equal. Figure B.1 illustrates the calculations from both modes.

In capture mode, the L1 controller points the aircraft's ground speed vector at the centre of the loiter circle. The resultant lateral acceleration depends on the angle between the ground speed vector and the radial line uniting the aircraft with the centre, according to Equation B.1d.

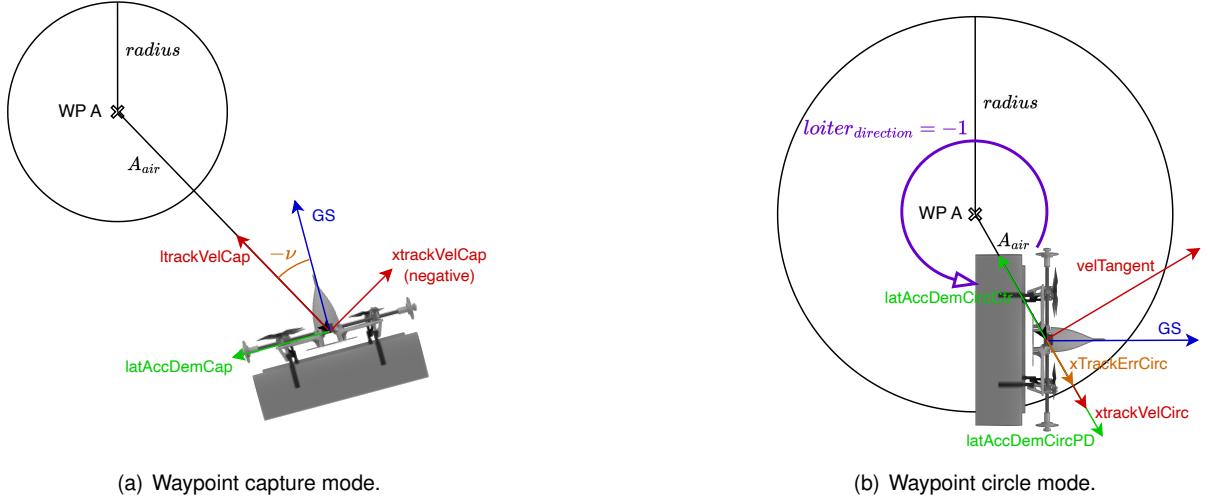


Figure B.1: L1 loiter controller.

On the other hand, in circle mode, the L1 controller calculates two different lateral accelerations, one to fix any tracking error of the loiter circle ($latAccDemCircPD$), which acts as a PD controller as it depends on the position and velocity error in the radial direction, and a second one ($latAccDemCircCtr$) which corresponds to the centripetal acceleration required to loiter at that given radius and direction. The output lateral acceleration corresponds to the sum of these two components, as seen in Equation B.1e. Note that although in Figure B.1 the lateral accelerations are indicated in the direction they intend to act, in fact, they are only scalars.

Lastly, it is worth mentioning that a positive lateral acceleration corresponds to a positive roll angle demand. The gains used in the loiter controller are computed according to Equation B.1a, which depends on the L1 controller parameters.

$$K_x = \left(\frac{2\pi}{L1_{period}}\right)^2, K_v = \frac{4\pi L1_{damping}}{L1_{period}}, K_{L1} = 4L1_{damping}^2, L1_{dist} = \frac{L1_{damping} L1_{period} GS}{\pi} \quad (B.1a)$$

$$xtrackVelCap = \langle \vec{A}_{air} \rangle \times \vec{GS}, ltrackVelCap = -\langle \vec{A}_{air} \rangle \cdot \vec{GS}, \nu = \text{atan2}(xtrackVelCap, ltrackVelCap) \quad (B.1b)$$

$$xtrackVelCirc = \langle \vec{A}_{air} \rangle \cdot \vec{GS}, xtrackErrCirc = A_{air} - radius \quad (B.1c)$$

$$latAccDemCirc = \frac{K_{L1} GS^2}{L1_{dist}} \sin \nu \quad (B.1d)$$

$$latAccDemCirc = loiter_{direction} (xtrackErrCirc K_x + xtrackVelCirc K_v + \frac{(loiter_{direction} xtrackVelCap)^2}{MAX(0.5radius, radius + xtrackErrCirc)}) \quad (B.1e)$$

Besides the loitering mode previously described, an additional waypoint controller is available in the L1 controller in forward flight. This controller receives as input the previous waypoint and the next waypoint, returning a desired roll angle, to follow the path that unites both points and thus reach the next waypoint.

In its operation, three different stages are available, for when the aircraft is behind the previous waypoint (WP A), in between both waypoints, or after the next waypoint (WP B), as depicted in Figure B.3. The UAV is considered to be behind the previous waypoint if it is further away from it than $L1_{dist}$, and behind a 135° arc around the point. If so, ν is computed such that the aircraft flies in the direction of WP A. Similarly, the vehicle is considered to be after the next waypoint if its distance to it along the track that unites points A and B is greater than three times the vehicle ground speed (meaning the aircraft is 3 seconds after WP B). In this situation, ν points the aircraft in the direction of WP B. Figures B.3(a) and B.3(b) illustrate both waypoint capture modes. Equation B.2 describes the computation of the lateral acceleration in both capture modes.

$$xtrackVel = \vec{GS} \times -\langle A/\vec{B}_{air} \rangle, ltrackVel = \vec{GS} \cdot -\langle A/\vec{B}_{air} \rangle \quad (B.2a)$$

$$\nu = \text{atan2}(xtrackVel, ltrackVel) \quad (B.2b)$$

Lastly, when the vehicle is in the region in between the two waypoints, it attempts to follow the path that unites both waypoints. To do so, the aircraft points itself toward the L1 point, which is the point on the track line that is located at a distance of $L1_{dist}$ from the vehicle. Figure B.3(c) illustrates this mode. Two separate contributions go into the output of this mode, one from the velocity vector error, ν_2 , and another one from the position error, with respect to the track, ν_1 , as described in Equation B.3.

$$xtrackVel = \vec{GS} \times \langle \vec{AB} \rangle, ltrackVel = \vec{GS} \cdot \langle \vec{AB} \rangle \quad (B.3a)$$

$$\nu_2 = \text{atan2}(xtrackVel, ltrackVel) \quad (B.3b)$$

$$crosstrack_{error} = A_{air} \times \vec{AB} \quad (B.3c)$$

$$\nu_1 = \arcsin\left(\frac{crosstrack_{error}}{L1_{dist}}\right) \quad (B.3d)$$

In addition, when $\nu_1 < 5^\circ$ (meaning that the vehicle is close to the track), an integrative component is added, as seen in Figure B.2 where ν is obtained, such that the crosstrack error converges to zero.

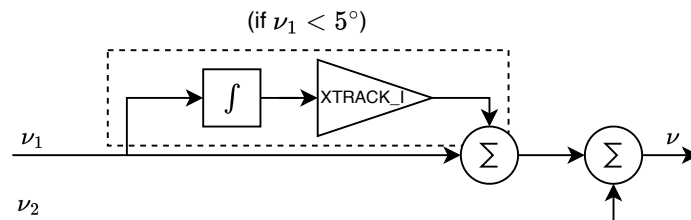


Figure B.2: L1 waypoint tracking loop.

In all three stages, the demanded lateral acceleration is obtained as previously seen in Equation B.1d, and the corresponding roll angle as previously described.

Note that this controller only handles the horizontal position in forward flight. The target height is sent differently depending on the control mode.

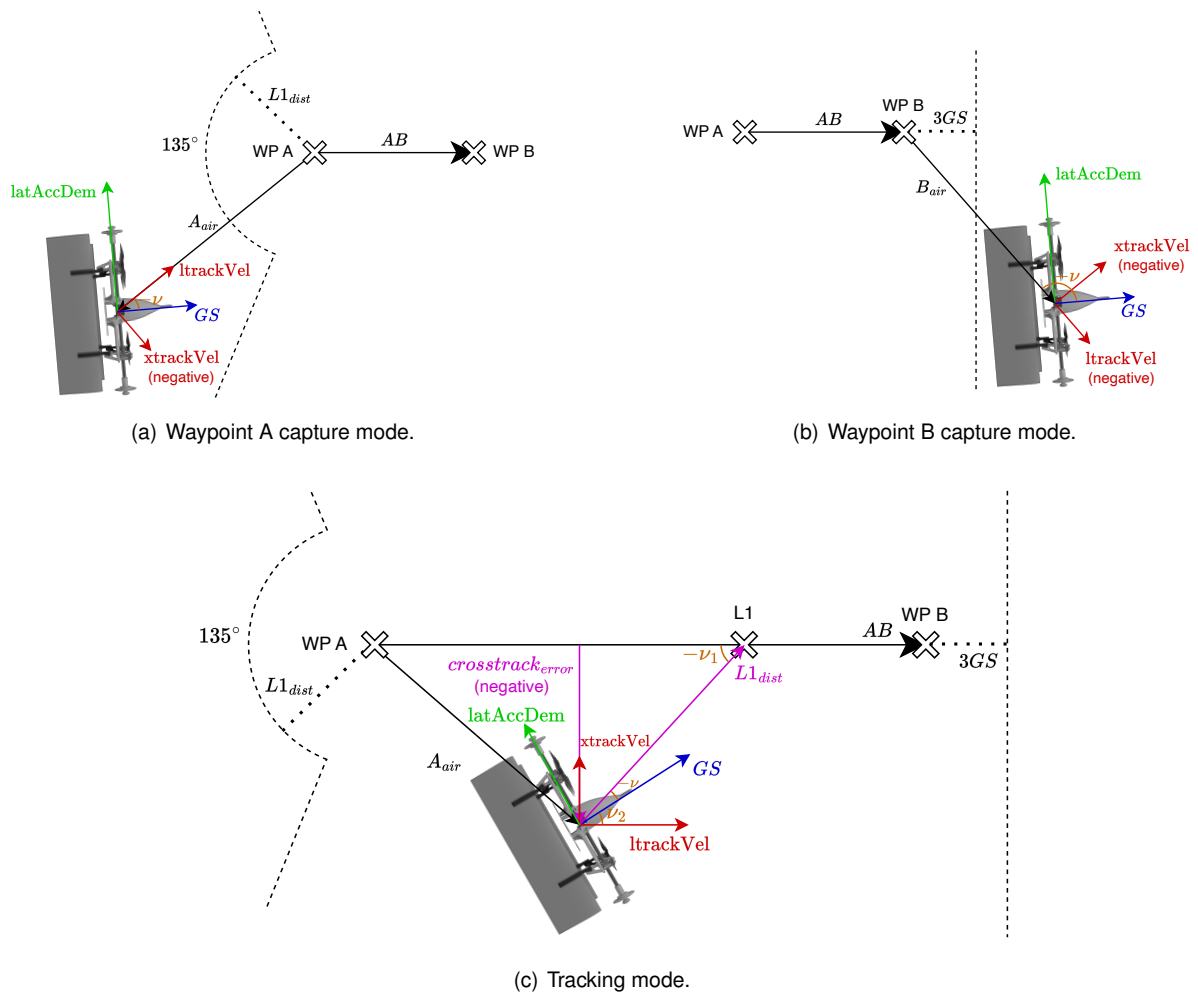


Figure B.3: L1 waypoint controller.

Total Energy Control System

The Total Energy Control System is responsible for controlling height and airspeed. To do so, it outputs a commanded pitch angle and throttle. However, the height and airspeed dynamics are significantly coupled, as a pitch command for example will have both an impact on height and airspeed. Because of this, TECS does not directly control pitch or throttle from either target airspeed or height. Instead, the total energy and the energy balance of the system are controlled. The total energy is defined as the sum of the kinetic and potential energies, whereas the energy balance represents the transfer of energy from kinetic to potential energy, and vice-versa, being hence defined as the difference between potential and kinetic energy. In turn, potential energy only depends on the height, and the kinetic energy depends on the airspeed.

Although approach and landing modes of this system are also available, only the mode active during cruising flight will be described. Additionally, although not directly implemented in the TECS, support for glide slopes is possible, where the height target is updated at each iteration in order to follow a desired

height slope. This is used for example in waypoint missions, such that the UAV does not instantly climb to the altitude of the next waypoint, but rather reaches that altitude at the same time as it reaches that waypoint. This is done by updating the altitude target with the proportion of the path that has been covered.

Changing the pitch angle leads to a change in the energy balance, as a change in the vehicle attitude from the level-flight scenario either leads to an exchange of potential energy for kinetic energy when pitching down or the opposite when pitching up. As such, to command the pitch output, the energy balance variation is used, as seen in Figure B.4, which fully describes this control loop. This in particular uses a proportional and integrative controller, as well as a direct feedforward from the desired energy balance rate. In addition, an integrative component of the kinetic energy error is present, as well as a feedforward from the measured airspeed, which is only used if the aircraft is gliding.

The PE_W and KE_W gains define the weight given to both potential energy and kinetic energy in the pitch control, derived from the SPDWEIGHT parameter, where $PE_W = \text{MIN}(2\text{-SPDWEIGHT}, 1)$ and $KE_W = \text{MIN}(\text{SPDWEIGHT}, 1)$. By default SPDWEIGHT is equal to one, giving equal importance to both energies. If SPDWEIGHT is 0, then the pitch output will solely be used for height control, and if it is 2, then the pitch output will be used exclusively for speed control [103].

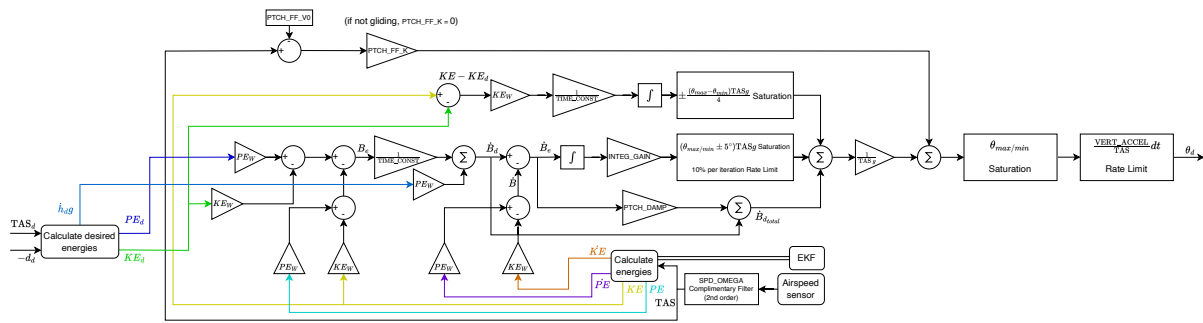


Figure B.4: Pitch TECS control loop.

Throttle, on the other hand, changes the total energy of the system. When the aircraft is flying at its trim throttle, the system maintains its total energy, above this value the total energy increases, and below it decreases. To obtain the throttle output, the total energy is used via a derivative, a proportional and an integrative component. In addition, there is a feedforward component from the rate of change of the desired total energy, which also includes a compensation component, such that in turn, the aircraft does not lose airspeed. The gain K_{TE2Thr} is obtained as $K_{TE2Thr} = \frac{T_{max} - T_{min}}{\text{TIME.CONST}(T_{E_{max}} - T_{E_{min}})}$. The throttle control loop is described in detail in Figure B.5.

Lastly, to obtain the energies used in both control loops, the computations described in Figure B.6 are applied. Note that PE denotes potential energy, KE is the kinetic energy, TE is the total energy, and B is the energy balance. Note that the airspeed used here is filtered, to remove any noise that is commonly found with airspeed sensor measurements, and that the variables indicated in grey, are not directly measured, but rather derived, either from the EKF or by computing finite differences from the measured variables. In particular, it is worth mentioning that \dot{V} is not obtained from finite differences of

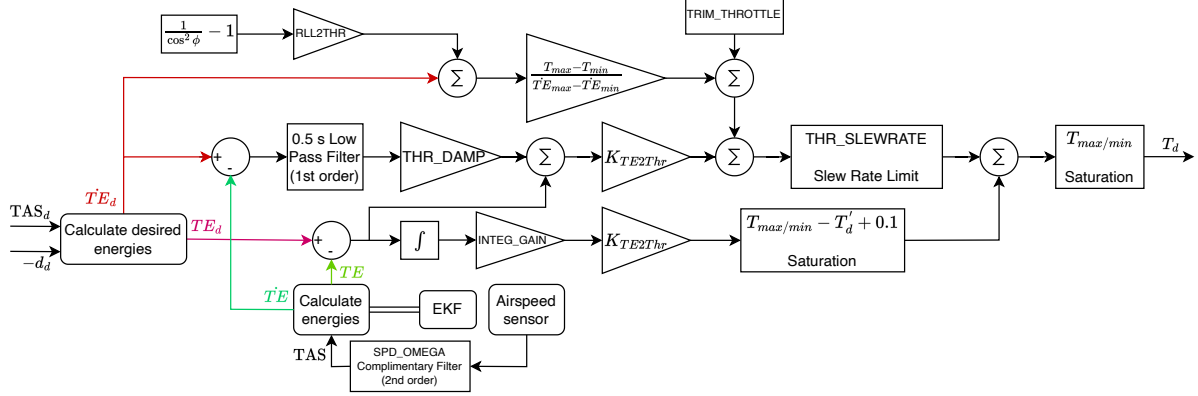


Figure B.5: Throttle TECS control loop.

the airspeed measurement, but rather by using the accelerometer measurements and applying a filter to them.

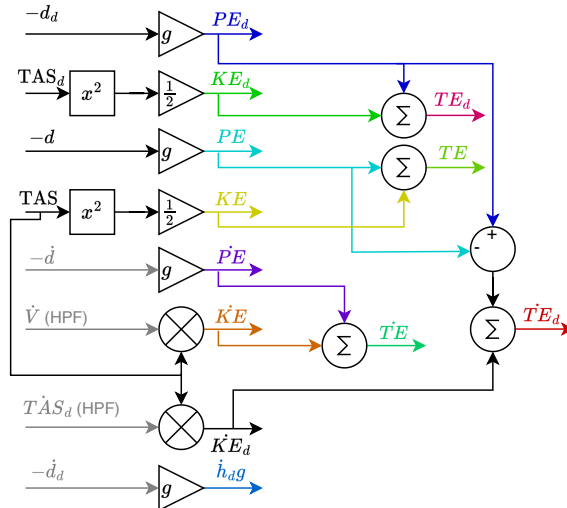


Figure B.6: TECS energy calculation (simplified).

B.2 Mission commands

The final layer, common to all modes, is the handler for mission commands. It is typically used during the AUTO control mode, where the pilot can define a fully automatic mission, with both hovering flight, forward flight and ground locomotion. These commands can be of two types, NAV and DO. NAV-type commands indicate the autopilot information to control the movement of the UAV, while DO-type commands tell the autopilot to perform a given action. The full documentation of the available commands supported by ArduPilot is available in [104]. Note that these commands are defined by the MAVLINK protocol, a universal standard used by several autopilots, however, ArduPilot does not support the full list of commands defined by MAVLINK, which is available in [105]. For each given command, a handler is implemented in ArduPilot for starting it, and for verifying its completion (mostly for NAV commands).

The Mission controller is updated at 10 Hz, and for each update, the current NAV command is run, as well as the current DO command. Whenever a NAV command is finished, the next NAV command is loaded and run (if available), but whenever a DO command is executed, only the DO commands before the next NAV command are executed. The following commands will be considered, for their relevance.

MAV_CMD_NAV_WAYPOINT

This is the main command used for navigation, as it sets a target waypoint for the aircraft to go to. It indicates the waypoint coordinates and altitude, the distance from the waypoint at which the waypoint is considered reached, and an optional pass-by distance from the waypoint.

It is the handler for this command that sets the next waypoint as the waypoint target, which is appropriately used by the waypoint controller. Navigation will be performed on whatever locomotion mode the vehicle is on, which can be set to a given default value for automatic missions, and changed during the mission, using the MAV_CMD_DO_VTOL_TRANSITION command. At this stage, the parameters for a smoother climb/descent gradient are calculated.

At each mission controller update, the waypoint controller target is updated to account for the pass-by distance and to verify if the waypoint has been reached. The waypoint is considered to be reached if the waypoint is at a user-defined distance from it (either by the mission or in the parameters).

MAV_CMD_NAV_TAKEOFF and MAV_CMD_NAV_VTOL_TAKEOFF

These two commands command the aircraft to take-off, either in a fixed-wing mode or in hover mode, respectively. In forward flight, the aircraft takes off to a specified altitude, and at a provided pitch angle. In hovering mode, on the other hand, the UAV takes off vertically and climbs a given height above its starting point. Alternatively, by changing the QuadPlane parameters, a final take-off altitude can be provided.

MAV_CMD_NAV_LAND and MAV_CMD_NAV_VTOL_LAND

Similarly, these two commands instruct the aircraft to land in fixed-wing or hover mode respectively. For fixed-wing landing, a target touchdown point is provided (and optionally landing altitude, should the aircraft land at a different place from the home point) and a flag to enable the aircraft to abort the landing automatically. For hovering landing, an optional landing point is specified (the current location is used otherwise) and an altitude difference from the default value for the aircraft to enter the final landing stage, in which it descends at a slower speed defined in the parameters. Optionally, the approach to the landing point can be made in fixed-wing mode.

MAV_CMD_DO_VTOL_TRANSITION

This command is used to command a change to a specified flight mode. Originally, this command used a value of 3 to switch to hover mode and a value of 4 for fixed-wing flight mode [104]. This command was meant to be applied to VTOL aircraft and as such, does not allow for a transition to a third mode. To

enable that, the MAVLINK implementation was modified to allow for a value of 5, where a transition to ground mode is commanded.

Unlike the transitions between hovering and fixed-wing modes, which can happen regardless of whether the aircraft is on the ground or not, a transition to ground mode can only be executed if the vehicle is not flying, and is in a VTOL (hover) mode. To account for that, a check was implemented that only allows the aircraft to execute the automatic transition to ground mode if the conditions are met. The aircraft is considered to be flying based on a probabilistic estimate, implemented by ArduPilot.

Appendix C

ArduPilot control modes

This appendix describes some relevant ArduPilot control modes that were not crucial to the results obtained in the present work.

C.1 Hover modes

C.1.1 QSTABILIZE

In QSTABILIZE mode, the aircraft hovers and levels itself on the roll and pitch axis. When the pilot does not provide any input, the aircraft maintains the heading. The pilot directly controls the throttle, and inputs the target pitch and roll angles and yaw rate, using the sticks.

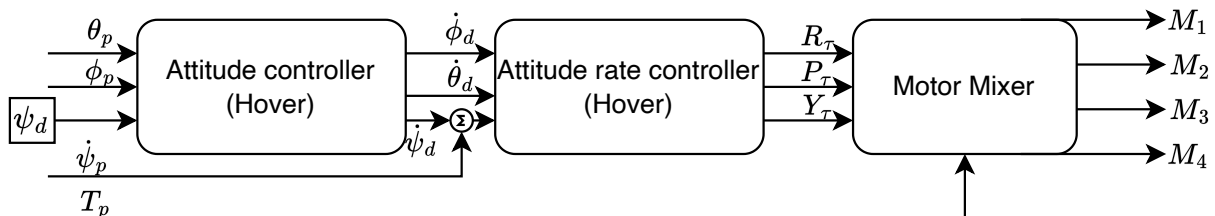


Figure C.1: QSTABILIZE mode.

C.1.2 AUTO and QRTL

While flying in hover mode in an AUTO mission, the aircraft hovers to each waypoint. The vehicle can fly in hover AUTO mode either by transitioning to it using a mission command or by setting the default AUTO mode to hover. In AUTO mode, the pilot does not control the UAV. The velocity the vehicle travels at is determined by the parameters.

In addition, the QRTL mode is available where the next waypoint is set as the home point from where the aircraft was launched, with the target altitude determined by a parameter. In this mode, the aircraft hovers back to the home point.

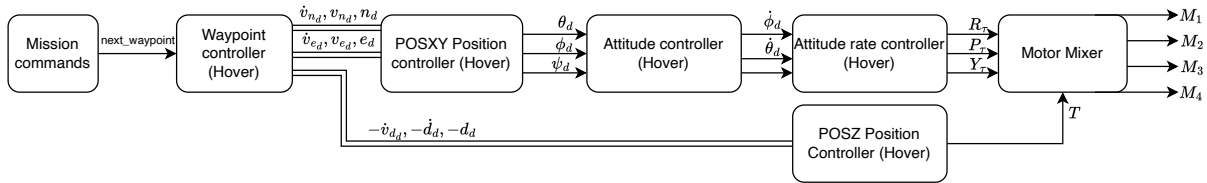


Figure C.2: Hover AUTO mode.

C.2 Forward flight modes

C.2.1 FBWB

In FBWB mode, the aircraft flies forward and maintains altitude and airspeed. The pilot is still in control of the roll angle and yaw rate, and the pitch stick now commands the climb rate, and the throttle stick the desired airspeed.

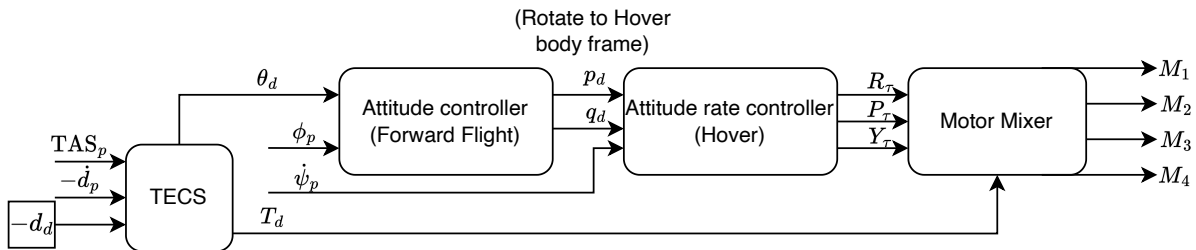


Figure C.3: FBWB mode.

C.2.2 AUTO, GUIDED and RTL

In forward flight, there are several possibilities for automatic flight. The most relevant, AUTO, navigates through a mission in fixed-wing mode. In GUIDED mode, the aircraft flies directly to a desired waypoint, usually sent from a GCS, and upon reaching it, loiters the waypoint. It is also possible for the aircraft to transition to hovering flight, and hover at the waypoint position, upon reaching it. Lastly, RTL, usually used as a failsafe mode, flies the aircraft directly to the home point, in fixed-wing mode. The velocity at which the aircraft flies in these modes is determined by the cruise airspeed.

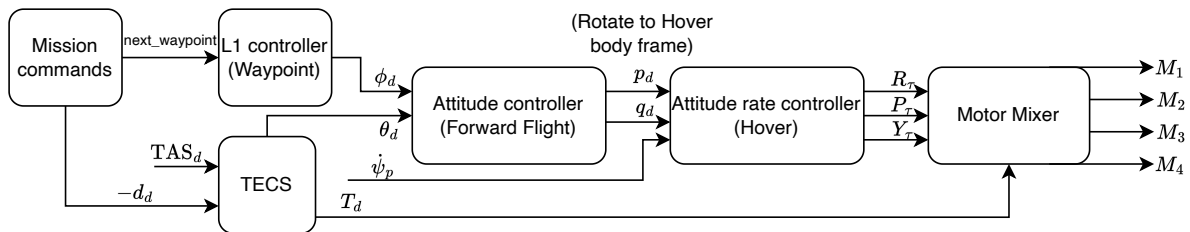


Figure C.4: Fixed-wing AUTO mode.

C.3 Ground modes

C.3.1 RDBWA

In RDBWA mode, the robot attempts to maintain longitudinal position. The pilot provides a pitch input, which is converted to forward acceleration, and a desired yaw rate. The throttle input is fixed, and the heading is maintained. This mode is designed to be used in conditions where disturbances, such as wind, are present so that the vehicle can overcome them.

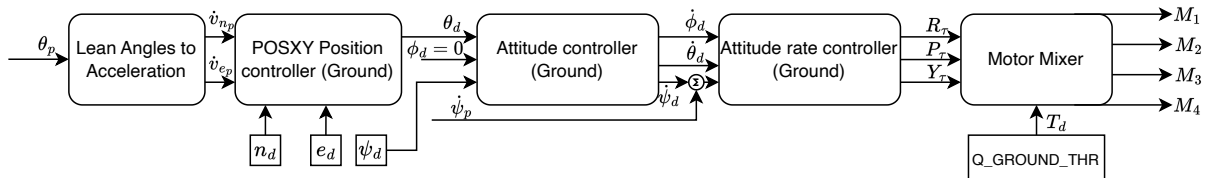


Figure C.5: RDBWA mode.

Finally, an RGUIDED mode was also planned, where the robot would drive automatically to a waypoint specified by the GCS, however, doing so would require further modification of the MAVLINK implementation, and of the GCS software, as the current implementation of guided requests is only meant to be handled in forward flight mode (in ArduPlane), and so, a prompt in the GCS software would be required to determine what mode the vehicle should handle the guided request in.